A Dissertation submitted in fulfilment of the requirements for the Degree of Doctor of Philosophy

Non-Intrusive Methods for Crowd Estimation

Farzad Tofigh

2019

University Of Technology Sydney,
Faculty Of Engineering and Information Technology, School Of Electrical and Data Engineering

Supervisor

Dr. Mehran Abolhasan

Co-Supervisors

Prof. Guoqiang Mao

Dr. Justin Lipman

Dr. Negin Shariati

Statement of Originality

I, Farzad Tofigh, declare that this thesis, is submitted in fulfilment of the requirements for the award of PhD in Engineering, in the School of Electrical and Data Engineeing at the University of Technology Sydney. This thesis is wholly my own work unless otherwise reference or acknowledged. In addition, I certify that all information sources and literature used are indicated in the thesis.

This document has not been submitted for qualifications at any other academic institution.

This research is supported by theAustralian Government Research Training Program.

Signature:

Production Note:
Signature removed prior to publication.

Farzad Tofigh

Date: Febraury, 2019

Table of Contents

List of Figures

List of Tables

List Of Abbreviations

ACS	Absorption Cross-Section
AP	Access Point
BLE	Bluetooth Low Energy
CDR	Call Data Record
CSI	Channel State Information
DNG	Double-Negative Material
EM	Electromagnetic
EMC	Electromagnetic Compatibility
ENZ	ε- Near Zero
ERR	Electric Ring Resonator
FDTD	Finite Difference Time Domain
FHS	Frequency Hopping Synchronization
FS	Frequency Synchronization
GHz	Giga Hertz
GPS	Global Positioning System
IAC	Inquiry Access Code
IR	Infra-Red
KNN	K-Nearest Neighbour
LHM	Left-Handed Material
MAC	Medium access control
MHz	Mega Hertz
MLE	Maximum Likelihood Estimation
MPA	Metamaterial Perfect Absorber
MNZ	μ Near Zero

List Of Abbreviations

NIM	Negative-refractive Index Material
PCB	Printed Circuit Board
PDF	Probability Distribution Function
RB	Random Back-off
RF	Radio Frequency
RFID	Radio-Frequency Identification
RHM	Right-Handed Material
RSS	Received Signal Strength
RSSI	Received Signal Strength Indicator
SAR	Specific Absorption Ratio
SINR	Signal-to-Interface-plus-Noise Ratio
SRR	Split-Ring Resonator
UHF	Ultra High Frequency
VHF	Very High Frequency
WSN	Wireless Sensor Network

List Of Parameters

τ	Parameter of exponential distribution
r	Euclidian distance
α	Path-loss exponent
$\Pr(Sync)$	Probability of having synchronized nodes
$\Pr(X)$	Probability of parameter X
P_t	Transmitting power
$P_r(X_{ij})$	Receiving power at node j from node i within the distance of x_{ij}
P_{th}	Threshold power
$PL(x_i, x_j)$	path-loss from node i to j
$PL_0(d_0)$	Path-loss at reference distance
d_0	Reference distance (Usually 1 Km)
Z_σ	Zero mean Gaussian random variable with standard deviation σ
ρ	Penetration rate; defined as the ratio of detected Bluetooth devices over the total number of people within radius R
C_{ij}	Recorded set of samples of received signal strength
S_{ij}^N	Recorded signal strength on AP number N
x_{ij}^N	Receiving signal strength plus noise from cell i and j in AP number N
X_t^k	position of node k at time t
z_t^k	measurements for device k at time t
$N(0, Q)$	Guassian Noise with mean of zero and covariance matrices of $Q = diag(\sigma_x^2, \sigma_y^2)$
P_{abs}	Absorbed power
m	body mass
σ_a	Absorbed cross section

List Of Parameters

S_c	Power density
δ	Penetration depth
ω	Angular frequency
σ	Conductivity
μ	Magnetic permeability
λ	Wave length
ε	Electric permittivity
E	Electric field
H	Magnetic field
k	Phase vector
Z_ω	Effective impedance
A_ω	Absorption ratio
Γ_ω	Reflection coefficient
T_ω	Transmission coefficient
ϕ	Polarization angle
θ	Incident angle

ABSTRACT

Urban living and its vibration environment pose ever-increasing challenges in our everyday lives. Urban planning and managing events requires correct and accurate information about the city and its environment. Residents as an inseparable component of the urban environment are affected most by any changes to it. Furthermore, the daily interactions of residents put increasing pressure on road infrastructure, power supply, and environmental management, including water, noise, air quality, healthcare and safety. Therefore, understanding their behaviour and the ability to monitor changes is one of the main interests for city management groups.

Current crowd density estimation technologies that leverage IR depth perception and video and image processing have privacy and deployment issues. Non-intrusive solutions have been introduced to reduce computational expenses and concerns regarding the privacy of residents. Probing for available Bluetooth and probing for available WiFi devices are among the popular non-intrusive methods for crowd detection, crowd distribution analysis and behaviour monitoring. However, both methods are highly dependent on the availability of such devices. Moreover, the uniqueness of MAC addresses threatens the privacy of individuals.

Estimating the crowd density based on available electromagnetic (EM) energy-level measurements is a fully non-intrusive method that monitors variation in EM radiation within an environment using a combination of advanced metamaterials and analytics to create a crowd density estimation detector. When measuring the EM energy in an environment, any object introduced into the measured environment directly affects the amount of EM energy observed within the environment. The human body is on average 60% water, which has an effect on the amount of EM radiation within the environment. Measuring the effects of humans on the current environment and comparing with expected models of behaviour allow

for an approximation of the number of individuals to be determined.

To accurately monitor changes in the EM energy observed, we make use of metamaterials. Metamaterials respond to various frequencies in terms of transmission, reflection and absorption. This feature provides the opportunity to use them as sensors in different applications. In this study, a polarization insensitive metamaterial absorber with size of $18 \times 18 \times 1.75mm^3$ is used to accurately measure variations in the signal levels at 2.4 GHz and 5.1 GHz. The absorbed energy is translated to measurable parameters of voltage and current through a network of resistors. The level of absorbed energy varies with the introduction of any absorbing object which can be detected by monitoring available voltage and current values. Simulation and measurement results of the proposed structure demonstrate its sensitivity toward the available EM energy with nearly 100% absorption efficiency and very stable performance (greater than 75% absorption ratio) for incident angles from $theta = 0$ to $theta = 70$.

Furthermore, individuals carrying mobile devices into a measured area will affect the energy level for the respective frequencies that the devices operate at. A single detector can be placed within a defined area to provide crowd estimation within a specific radius (e.g., a room, an elevator, or a platform). Alternatively, multiple detectors can be tiled throughout a defined area to provide a crowd distribution.

ACKNOWLEDGEMENTS

This thesis would not have been fulfilled without the supervision and guidance of many individuals who contributed and extended their valuable assistance in the preparation and completion of this study.

At first, I offer my sincerest gratitude to my principal supervisor, Dr. Mehran Abolhasan, who has supported me throughout my thesis with his patience and knowledge. I attribute the level of my Ph.D. degree to his encouragement and effort, and without his support, this thesis would not have been completed.

I am indebted and grateful to Dr. Justin Lipman for his unconditional support and valuable guidance during this thesis. It is an honour for me to work with him during my studies. He has not been only a great advisor, but also an encouraging and motivating friend.

I am truly thankful to my co-supervisor Prof. Guoqiang Mao for all his invaluable guidance and directions during my studies. He was always available and willing to assist. I would like to thanks him for his immense contribution to this thesis and advices.

My sincere thanks also goes to Dr. Negin Shariati and Dr. Wei Ni for all their support and guidance during this thesis.

I wish to express my sincere appreciation to my lab-mate, Mr. Majid Amiri, for all the stimulating discussions, tireless working days and nights before deadlines (reminiscing our trip to Melbourn) and for all the fun we have had every morning at gym.

It is with immense appreciation that I acknowledge Sydney Trains for providing the opportunity of engagement in a real-world scenario research problem. They kindly provided access to train platforms and related data.

I am also grateful to Mr. Gennady Lavrov for all his help in implementing "MobiSensing" platform. I also would like to thank Mr. Qinghua Tan for his presence and help during Bluetooth data collection.

A very special gratitude goes out to Mr. David Welch for his assistance during the measurements on his very busy day.

Last but not the least, I would like to thank my family and all my friends (too many to list here but you know who you are!) for providing support and friendship that I needed all these years.

To my parents, Fariba and Hossein,

and my brother, Behrad

Chapter 1

Introduction

1.1 Thesis motivation

Urban living poses ever-increasing challenges in our daily lives. Therefore, cities must be smarter in managing their resources, infrastructure and environment to promote economic, social and environmental well-being, and urgent solutions are required for viable living conditions and sustainable city development.

Residents as an integral component of a city play a critical role in it. The impacts of residents' daily interactions and activities are undeniable on the city environment and infrastructure. These interactions and activities are exponentially increasing due to population growth. The recent report of the Australian Bureau of Statistics predicts 100% growth in Australia's population by 2075 [1]. This prediction means that New South Wales will experience 35% growth rate in its population by 2040, whereas Sydney will have a population of 7.9 million people (84% growth) in 2053. The other three largest cities will be Melbourne, projected to have a population increase of 93% by 2053, and Brisbane and Perth, which are predicted to experience increases of 42% and 63%, respectively, by 2028. Furthermore, another report predicts a 1% yearly increment in total number of daily trips, meaning 27

million trips on an average workday by 2036, in Sydney alone [2]. Thus, understanding residents and their behaviour, needs, and distribution will help city management teams plan for the future properly.

A wide range of crowd estimation and monitoring solutions have been proposed and investigated. Image-processing-based approaches [3] are among the most popular solutions in crowd detection and monitoring. However, all the provided solutions require recorded images of residents in the environment, which can violate their privacy. Furthermore, monitoring areas are limited by computational expenses and the number of cameras that can be deployed. To address the expenses and deployment issues, techniques of wireless scanning for devices have been proposed. Bluetooth and WiFi probing [4,5] can be easily employed to provide the required information regarding crowd changes in the scanning area. However, the accuracy of estimation and monitoring depends on the number of available devices and frequency of scans.

Non-intrusive crowd estimation approaches [6, 7] that are based on available wireless technologies offer solutions for estimation while preserving privacy. These solutions, such as channel state information (CSI) monitoring [8], observe defined features of the available signals and map them to changes in the environment. Although machine-learning algorithms [9] that are used to address the complexity of the feature variations and its mapping provide good accuracy for estimations, the computational expenses of training an algorithm are undeniable. Therefore, a new method with less complexity would be a worthwhile contribution towards non-intrusive crowd estimation.

1.2 Thesis scope and objectives

Probing for possible Bluetooth and WiFi devices is used in crowd detection, crowd distribution analysis, and behaviour monitoring. However, both solutions highly depend on the

availability of the media.

Participatory Bluetooth scanning is one of the methods introduced as a solution to detect crowds [10, 11]. In this approach, a node itself serves as a scanner and provides information to detect the number of devices around and, consequently, the number of people. However, the scanning radius varies in different environments and densely crowded areas. A chapter of this thesis investigates an analytical approach to increase the accuracy of the estimations.

WiFi scanning is the other approach for the passive detection of crowds and their distributions [5, 12, 13]. Recently, a new security measure known as dynamic WiFi MAC address for mobile phones was introduced; this feature can result in multiple detections of an individual. Moreover, the frequency of scans is critical in determining the distribution of a crowd. Applying prior knowledge to the analysis helps to overcome the sparse data collection. A real-world experiment on a train station platform is performed to map the crowd distribution throughout the platform.

Although both Bluetooth and WiFi scanning are categorized as non-intrusive crowd estimation approaches, yet there is a possibility of recording the gathered data to track individuals. In addition, fully non-intrusive solutions such as channel state information have also been introduced to detect and monitor crowds. In such methods, complicated algorithms are used to observe the defined features of the available signals and map them to changes in the environment. Thus, a fully non-intrusive method with less complexity would be a worthwhile contribution to crowd detection and monitoring.

The objectives of this dissertation are as follows:

- To provide an analytical model to increase the accuracy of Bluetooth scanning for crowd estimation.

- To provide an analytical model to derive the distribution of crowd using WiFi scans with sparse data collection.

- To introduce a fully non-intrusive method of crowd estimation.

1.3 Thesis contributions

In this dissertation, non-intrusive methods for estimating crowd density are investigated. In this regard, crowd detection and density estimation methods based on Bluetooth and WiFi scans with a backup of mathematical analysis are provided. Following these methods, a novel method for crowd detection using measurements of electromagnetic energy levels is proposed. Finally, a method for accurate measurements using metamaterial absorbers is presented.

1.3.1 Bluetooth probes

Chapter 3 of this dissertation investigates a probabilistic approach to increase the accuracy of estimation using participatory Bluetooth scanning. The discovery probability and probability of detection are calculated and based on experimental data, and unknown parameters are estimated using the maximum likelihood estimation method. Another set of experiments are performed to test the proposed approach in estimating number of people around a node. A testbed is also designed and implemented using an Android app that collects data and uploads them to the cloud. The collected data are analysed, and the results are represented on a webpage to provide an understanding of the city-wide crowd distribution.

1.3.2 WiFi probes

In chapter 4, WiFi probing is studied in a real-world scenario, with the aim of providing crowd counting and its distribution. The data that are collected on a train station platform are used to drive the fingerprint map. Considering the resolution of collected data, prior knowledge is applied to produce a probability map, with the aim of increasing the accuracy

of location estimates. The probability map is used to estimate the locations of the detected nodes and calculate a density heat map. The acquired heat map is compared with the results of analysing CCTV images and exhibits a good correlation.

1.3.3 A fully non-intrusive approach

Chapter 5 provides a new solution for non-intrusive crowd detection and estimation. In this method, available electromagnetic energy levels are measured and used to estimate the number of people in a room. When measuring EM energy in an environment, any object introduced into the measured environment directly affects the amount of EM energy observed within the environment. The human body is on average 60% water, which has an effect on the amount of EM energy within the environment. Measuring the impact of humans on the current environment and comparing with expected models of behaviour allow for an approximation of the number of individuals to be determined.

1.3.4 Metamaterial absorbers

Metamaterial absorbers are designed to catch RF signals and dissipate them. However, the induced surface current can be measured to determine the amount of available and absorbed RF energy. To this end, a polarization-independent low-frequency metamaterial absorber using space-filling curves is presented in chapter 6. The approach of using space-filling curves is employed to reach lower frequencies with smaller dimensions of unit cells. The proposed structure provides 99% absorption at 900 MHz with a unit cell size of 0.075λ [1].

In chapter 7, a dual-layer metamaterial absorber targeting available WiFi bands (2.4 GHz and 5 GHz) is introduced. WiFi bands are chosen due to their availability indoors. It is noteworthy to mention that 2.4 GHz is very close to the body resonance at 2 GHz, which increases the accuracy of measurements due to high body absorption. The proposed structure

[1] λ indicates the wavelength.

is based on Rogers 3003, with a dielectric loss of 0.001, allowing us to redirect the induced surface current to a resistor and measure the voltage. Furthermore, to avoid measurement interference, resistors are moved to the bottom layer of the structure using single vias. The design is polarization-independent, and it exhibits a greater than 75% absorption ratio for incident angles from $\theta = 0$ to $\theta = 70$.

1.3.5 Relevant publications

Patents:

- Australian patent pending, "Methods and Apparatus of Crowd Estimation Based on Electromagnetic Energy Measurements," Application number: 2018201509.
- US provisional patent, "Methods and Apparatus of Crowd Estimation Based on Electromagnetic Energy Measurements," Application number: 62636839.

Conference papers:

- F. Tofigh, M. Amiri, N. Shariati, J. Lipman, M. Abolhasan, "A Polarization-Independent Low-Frequency Metamaterial Absorber Using Space-filling Curve," Submitted to EuMC, 2019.
- F. Tofigh, G. Mao, J. Lipman, M. Abolhasan, "Crowd Density Mapping Based on WiFi Measurements on Train Platforms," ICSPCS' 2018.

Journal papers:

- F. Tofigh, M. Abolhasan, G. Mao, W. Ni, "Bluetooth Discoverability Probability Model For Smartphone Based Crowd Density Estimation," Submitted to IEEE Access, 2018.
- F. Tofigh, M. Amiri, N. Shariati, J. Lipman, M. Abolhasan, "Polarization Insensitive Metamaterial Perfect Absorber for Crowd Estimation Based on Energy Level Measurements of Ambient Electromagnetic Waves," Submitted to Scientific Reports, 2018.

- F. Tofigh, M. Amiri, N. Shariati, J. Lipman, M. Abolhasan, "Crowd Estimation Using Electromagnetic Wave Power-Level Measurements," Submitted to IEEE Transactions on Vehicular Technology, 2019.

- M. Amiri, F. Tofigh, N. Shariati, J. Lipman, M. Abolhasan, "Miniature Tri-band Sierpinski-Minkowski Fractal Metamaterial Perfect Absorber," accepted to appear in IET Microwaves, Antennas & Propagation, 2019.

Chapter 2

Crowd Estimation in Literature

Residents as an integrated part of cities play critical roles in future planning for every city and related events. In the last few decades, rapid increases in population have increased the requirement for accurate estimation of crowds. Crowd analysis has drawn significant attention from researchers in recent years due to a variety of reasons. Exponential growth in the world population and the resulting urbanization have led to an increasing number of activities, such as sporting events, political rallies, and public demonstrations, thereby resulting in more frequent crowd gatherings in recent years. In such scenarios, it is essential to analyse crowd behaviour for better management, safety and security. To this end, various techniques have been introduced. This chapter provides an overview of the presented crowd estimation and its mapping techniques.

2.1 Crowd estimation techniques

Crowd counting as the basis of crowd estimation aims to provide the number of people in an area while offering the capability of mapping the counted numbers and extraction of corresponding density map. This capability would provide valuable information in making

decisions and infrastructure development for the future. A wide range of techniques, with different goals, have been introduced recently to provide the required crowd density maps. These techniques range from the grid density method by H. Jacobs [14] to more advanced and accurate methods that require deployment of sensors in the area of interest that are able to collect the required information [6, 15–18].

Image-processing techniques using digital cameras have proven to be effective techniques for crowd estimation [15]. Other methods that can be categorized as signal-based methods leverage the ubiquitous adoption of various wireless sensors, especially Bluetooth and/or WiFi radios [4, 16, 19, 20]. The remainder of this section discusses each technique in more detail.

2.1.1 Vision-based crowd estimation

One of the most common techniques for crowd estimation is using digital cameras while employing image-processing techniques to detect human beings and provide the number of people per pixel presented in the image (as illustrated in Fig. 2.1). Similar to most computer vision problems in any non-uniform environment, crowd analysis also comes with numerous challenges, such as occlusions, high clutter, non-uniform distribution of people, non-uniform illumination, and intra- and inter-scene variations in appearance, scale and perspective. The complexity of the crowd analysis problem has led to an increased focus of researchers on image analysis techniques. These methods can be classified into three main categories:

1. Detection-based analysis

2. Regression-based analysis

3. Density estimation-based analysis.

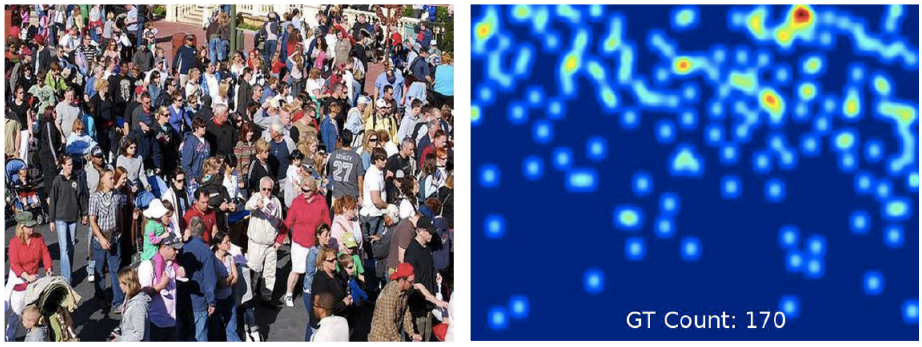

(a) (b)

Figure 2.1: Illustration of vision-based crowd estimation and density mapping.

2.1.1.1 Detection-based analysis

Detection frameworks were one of the early approaches in vision-based crowd analysis. In this approach, a detector, ranging from face detection techniques to human body detection [21], is employed to detect people and count the number of people in the area [22, 23]. It is noteworthy to mention that most of these approaches train a classifier using different machine-learning techniques, such as support vector machines [24], random forest [25], and neural networks, to detect pedestrians [26–29].

2.1.1.2 Regression-based analysis

In regression-based approaches, a mapping technique that matches the count with extracted features from local image patches is used [30–32]. Using this approach, the process of training and learning detectors can be avoided, which helps to reduce the complexity of the crowd estimation process.

2.1.1.3 Density estimation-based analysis

To include spacial information in the analysis, [33] proposed the technique of learning a linear mapping between local patch features and corresponding object density maps. Using this technique, spatial information is incorporated into the learning process and eliminates

the process of the detection and localization of individual objects. Thus, the integral of the density map over any region provides the count within that region.

In summary, although vision-based approaches have been proven effective and accurate, they also have been proven to be computationally expensive, especially over a large area. Moreover, image-processing techniques are highly dependent on the image quality, which can be easily affected with weather conditions or light. There are propositions to address some these issues, such as using UAV (Unmanned Aerial Vehicle) and UGV (Unmanned Ground Vehicle) images [34]; however, it is still challenging to obtain automated global awareness based on images, especially for large crowds.

2.1.2 Signal-based crowd estimation

Considering the ubiquity of wireless technologies, signal-based techniques are introduced as an alternative solution to detect people and provide the crowd density. In comparison with vision-based approaches, signal- based techniques are more cost-effective and easy to deploy in large areas. These techniques can be categorized into two approaches: "device-based" or "device-free". In device-based approaches, the detection is tied to a specific device that people are carrying—for example, RFID tags. In device-free approaches, the detection is not related to the devices carried by people. In some of the literature, mobile phone-based approaches are considered device-free approaches due to the ubiquity of mobile phones.

2.1.2.1 Device-based techniques

In device-based strategies, users have to opt in by carrying a specific device, such as RFID tags, to take part in estimation. These techniques usually require dedicated scanners to detect the specified devices. Passive approaches are an alternative to opt-in approaches in which density estimation occurs without user awareness or participation.

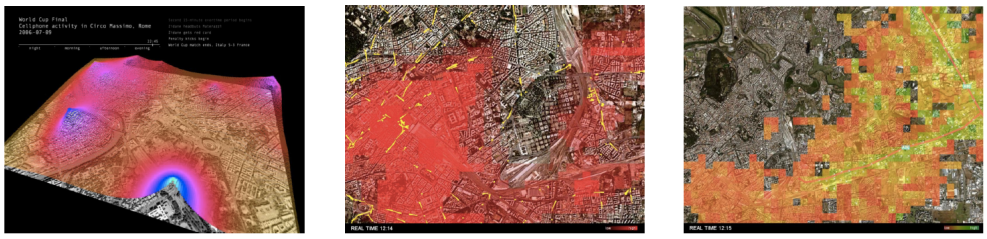

(a) (b) (c)

Figure 2.2: (a) Rome during events. (b) Rome public transportation. (c) Traffic flow [35].

2.1.2.1.1 Cell tower information In 2011, Calabrese et al. used cell tower information by extracting all the signalling messages to derive the number of associated devices [35]. These information integrated with the location of buses and taxis used to map crowd dynamics (Vehicular traffic and movements of pedestrians and foreigners) in Rome, Italy. Fig. 2.2 represents some of the results of this research. It is noteworthy that this method depends on the active mobile equipment, not the actual number of devices around each tower.

In another technique, the call data record (CDR) was used to estimate the number of devices around each tower around Morristown, New Jersey to analyse the flow of people [36]. Authors analysed voice and SMS traffic data through 35 cell towers for 60 days to obtain Morristown laborshed[1] and partyshed[2] maps. CDR contains the client number, timestamp and associate base-station ID. However, this information is available only if the user tries to make a call or send an SMS. Moreover, the location accuracy is related to the BS's sector coverage, usually more than 300 meters. To address localisation challenges, Wirz et al. suggested the use of mobile device GPSs during the Lord Mayors Show in London using a specific mobile app [20]. This method was also used by Koshak *et al.* to derive the behaviour of people during Hajj [37].

[1]Represents the geographical distribution of city workers' living areas.
[2]An example footnote.

2.1.2.1.2 Social media posts Every activity and interaction on the Internet leaves a footprint that can be used to extract useful data. In 2015, Botta et al. used two months of recorded CDR data (calls, SMSs, and Internet activity) along with associated locations of Twitter posts to quantify the crowd size in Milan [38]. In another study, Sinnott et al. used social media data (Twitter posts) to estimate crowd size in four different sport events across the world [39]. They have investigated 61 matches in England, 51 matches in Spain, 61 in Italy and 45 AFL matches in Australia to provide and estimation of the number of attendees. The authors, claim that they could reach the error as low as 0.04342. However, this error is 0.33663 for AFL in Australia and 0.27977 in Seire A of Italy.

2.1.2.1.3 RFID tags Managing large events such as Hajj comes with its own challenges, and understanding the crowd behaviour would help to control and manage it better. Yamin et al. proposed the use of RFID tags as wrist bands to understand the crowd behaviour during Hajj and Kumbh [17, 40].

2.1.2.1.4 BLE tags Bluetooth low-energy tags have been introduced as a low-cost alternative to RFIDs to understand crowd dynamics during Hajj [41]. During this study, 600 tags and ten smartphones were used for 5 days to collect data for crowd analysis.

2.1.2.1.5 MAC address scanning In communication networks, MAC addresses are defined as a unique identifier of a network interface. The ubiquity of mobile phones and their related sensors and networking interfaces such as Bluetooth and WiFi enable them to be used in people counting and crowd estimation. The unique MAC addresses of Bluetooth and WiFi interfaces can be detected with scanners and used to estimate the number of people around each scanner [5]. Although there are differences between Bluetooth and WiFi protocols [4], both technologies are vastly used as simple and low-cost solutions for crowd density and behaviour estimation.

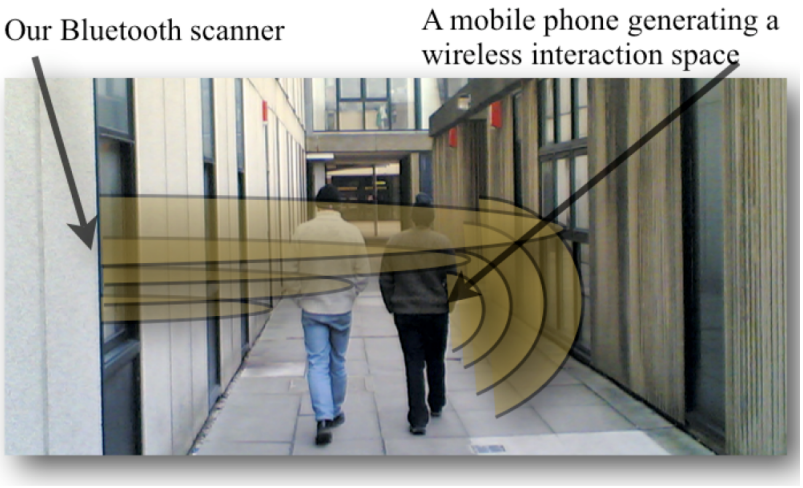

Figure 2.3: Bluetooth scanning window in [42].

In early research, in 2006, O'Neill et al. used Bluetooth scanning with two methods of gatecounts that provide the count on the gate and static snapshots to understand the patterns of movements and presence of crowds [42].

In recent years, Bluetooth technology has been suggested as a low-cost alternative solution for crowd detection and spatial behaviour extraction [43] [44] [45] [46, 47]. The tracking feature of Bluetooth has encouraged its use in a large number of applications, such as understanding people's behaviour in a shopping mall [48] and travel time estimation on highway segments [49]. Leveraging this feature of Bluetooth, Versichele et al. installed 22 Bluetooth scanners to cover various areas of the Chent Festivities event in 2012 [50]. Analysing the data gathered over 10 days, the authors extracted various trajectories that visitors follow during the festival. Using this method, the estimated number of unique visitors was claimed to be approximately 735,000 (minimum: 630,000, maximum: 880,000), with $\sim$ 1.4 million visits in total, which shows an acceptable accuracy compared to the estimate of 1.5 million visitors from the city. This approach was also implemented indoors during the trade fair in Belgium in 2012 with the purpose of understanding visitors' behaviour during the event [51].

In 2014, in a German airport, Bluetooth and WiFi scanners were installed to capture

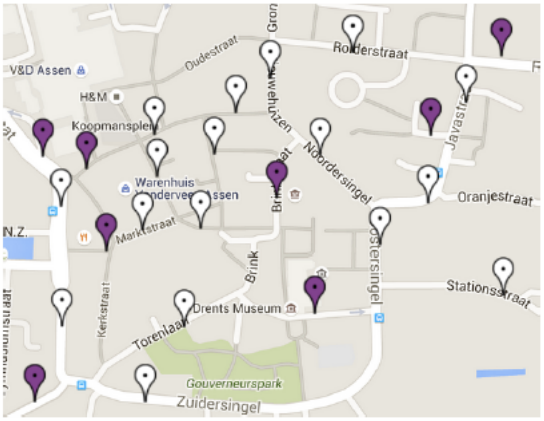

Figure 2.4: Deployment of WiFi scanners in the city centre of Assen, as shown in [13].

MAC addresses of available mobile phones to estimate pedestrian flow [12]. A similar approach has also been implemented in an office area to understand the different behaviours of people, especially as a group [52]. In [13], the authors deployed 27 WiFi scanners in the city centre of Assen during a festival, as shown in Fig. 2.4, to extract the number of attendees and related patterns during the festival. This technique was also used in Madrid to estimate the number of bus travellers by installing WiFi monitoring units and analysing the collected data [53].

As described above, in the majority of previous approaches, fixed scanners are used to scan the surroundings, and the collected data are used to perform estimations. Covering a large area with fixed scanners can be costly and not feasible. To address this issue, Stopczynski A. *et al.* introduced the method of participatory Bluetooth scans during a large music festival [10]. In this approach, a subset of participants installed an application that records Bluetooth scans. The location and detected Bluetooth devices are sent to a server to estimate the number of festival participants and their distribution. Fig. 2.5(a) shows the extracted density distribution during the festival. In another study, Weppner et al. used a similar approach to estimate the crowd density and understand its flow during a three-day city-wide festival in Zurich [11]. The extracted density map is shown in Fig.

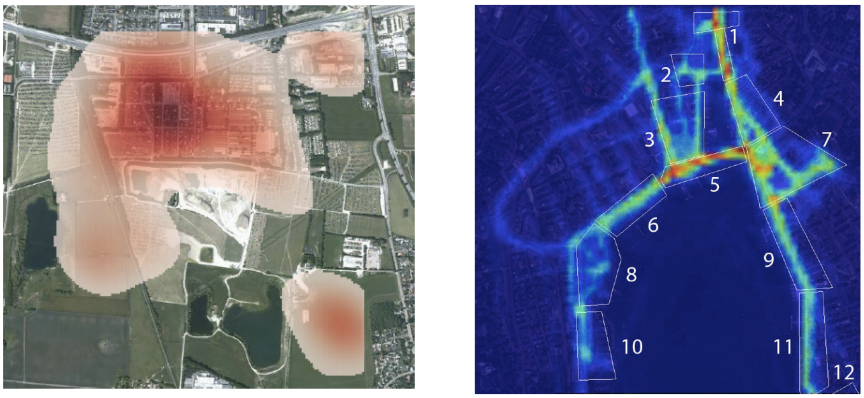

(a) (b)

Figure 2.5: (a) Kernel density at a music festival, as described in [10]. (b) Extracted density map of [11].

2.5(b). The outcomes of the data analysis were backed up using ground-truth data, and the accuracy of the results in correlation with the number of scanners and various scanning windows was analyzed. The error for the proposed approach investigated in two different scanning windows, ranging 65.44% in 10 minutes window to 26.11% in 30 minutes windows. Hence, the best accuracy that they achieved was 73.89%. It is noteworthy that both studies assumed 10 metres for effective Bluetooth detection; however, according to its specifications and experiments, the effective detection radius could be greater (up to $100m$).

2.1.2.1.6 Audio Tone based In an interesting approach, Kannan *et al.* Introduced audio tone as a source of information to extract the number of crowd [54]. In this method, they used speaker phone to transmit one or more simple tone and record audio tones with 44 KHz sample rate in the frequency range of 0 to 22 KHz. Fig. 2.6 illustrates the introduced method by the authors. In this method, each phone sends a tone with an initial bit pattern. This tone is received by other phones and after performing bit-wise OR operation is saved as a new packet. This cycle continues until the counting is done and provides 90% accuracy in counting.

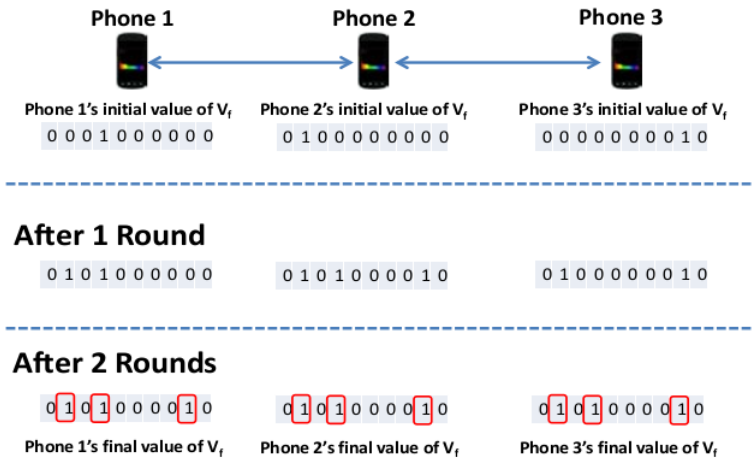

Figure 2.6: Illustration of Audio Tone based counting described in [54].

2.1.2.2 Device-free techniques

All of the aforementioned techniques require a detectable device to estimate the crowd density and its behaviour. However, it is not feasible to expect people to carry a device all the time. Moreover, privacy concerns and new security measures, such as the invisibility of Bluetooth devices and periodic changes in advertised MAC addresses, can increase the error of estimations [55]. Researchers have suggested device-free methods to overcome these issues. These methods can be categorized into two main groups:

- RSS Monitoring and Measurements.
- Channel State Information.

2.1.2.2.1 RSS Monitoring and Measurements One of the popular methods for device-free estimation is to monitor changes in RSS measurements. In [6], the authors recorded the received signal strength (RSS) values on a grid of a wireless sensor network (WSN), as shown in Fig. 2.7(a) to classify the crowd density as low, moderate, or high. Experimental results for two different conditions, static and moving, shows an accuracy up to 95%. However, the classifier categories moderate as both highly and moderately crowded. Moreover, the

proposed method fails detecting high intensity crowd in static mode. Wang *et al.* proposed a solution to measure queues based on the RSSI monitoring technique [56].

In another approach, Depatla *et al.* used one receiving antenna to record the changes in the RSS values [57]. Their approach, as shown in 2.7(b), mainly relies on the behaviour of signal facing blockage and also scattering effects. Experiments show that authors can estimate number of people with more than 92% accuracy. Using a similar approach, Depatla *et al.* repeated the experiment while placing antennas behind walls and analysing the recorded information [7]. The obtained results demonstrate over 81% accuracy in detecting the number of people through the wall.

2.1.2.2.2 Channel State Information (CSI) Channel state information specifies the channel properties in a communication link. This information explains how a signal propagates from the transmitter to the receiver and outlines the combined environmental effects of scattering, fading, and power decay with distance. Since the CSI can contain more information compared with RSS values, researchers have used it to estimate the crowd number [8]. In [58], authors monitor WiFi links in home to identify in-place and walking movement activities. This is done by comparing signal profiles and they have reached 96% average true positive rate with less than 1% average false positive rate. Fig. 2.8 describes the main approach used to estimate the crowd density and people's activities based on CSI analysis.

Based on CSI analysis, Yang *et al.* presented a method to count the number of people passing by [59]. They suggested using the pattern of phase differences to recognize moving directions. In a recent study, by leveraging the WiFi-enabled devices in combination with CSI analysis, Zou *et al.* suggested a method of occupancy detection and estimating the number of people indoors with the accuracy of 99.1% and 92.8%, respectively [60].

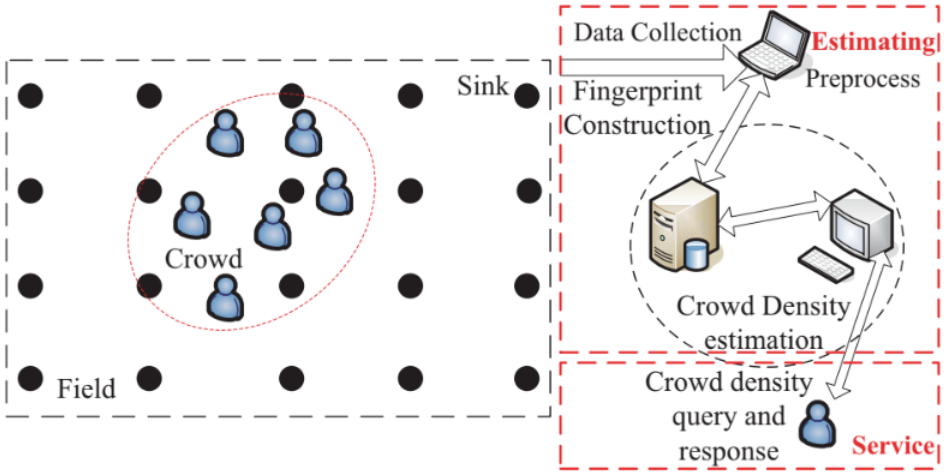

(a)

(b)

Figure 2.7: Crowd estimation using RSS measurements in [6].

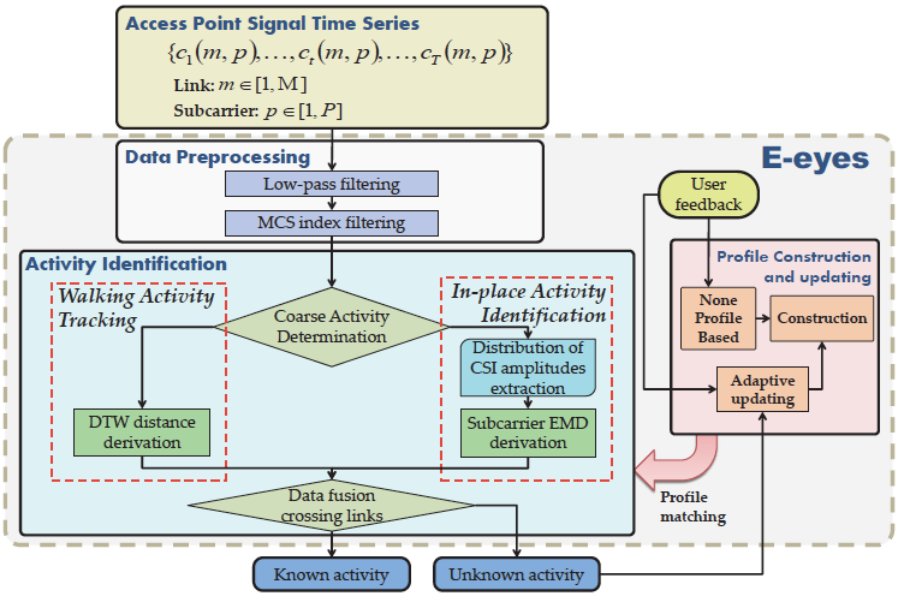

Figure 2.8: Crowd estimation and activity recognition based on CSI analysis in [8, 58].

2.2 Conclusion

An overview of different methods for crowd estimation is provided in this chapter. There are number of vision-based techniques cited frequently in literature as one of popular approaches in crowd estimation. Although vision-based techniques are presented an acceptable accuracy, but their accuracy is highly depended on the image quality. In addition, there is always concerns of privacy due to possible face detection and tracking. As an alternative solution, signal-based methods are represented. Methods such as RFID tags or WiFi or Bluetooth MAC address detection, comes with a concern of privacy and tracking. Tackling this issue, more complicated solutions such as channel state information analysis are introduced. However, these methods are complex in terms of anlysing recorded channel state information. Remaining of this thesis, investigates possible solutions for non-intrusive methods of crowd estimation with less complexity.

Chapter 3

Bluetooth Discoverability Probability Model For Smartphone-based Crowd Density Estimation

Crowd density estimation is an integral part of crowd analysis and has found extensive application in crowd control and city planning. Over the last decade, a range of measurement techniques from visual sensing to image processing have been used to provide measurement. However, the increasing ubiquity of mobile devices carried by people has enabled a number of new approaches to perform crowd density estimation. This chapter presents a participatory approach to estimate crowd density through Bluetooth scanning of mobile devices. The participatory approach is low cost, can cover a large area and can provide an understanding of the crowd and its behavior. The proposed approach provides an accurate method for crowd estimation in one scanning period using a probabilistic model. The model considers the Bluetooth discovery probability, distances among nodes, and environmental effects. Theoretical analysis are supported with field measurements and experiments which shows a good agreement with the theoretical analysis.

3.1 Introduction

Crowd density estimation has been of significant interest to crowd analysis over the last several decades. The application of crowd analysis can be applied within varying domains: the success of an event as measured by the number of participants attending an event; emergency response and related event planning for large scale public events such as New Years Eve celebrations; transport planning and targeted advertising for marketing analysis. Understanding the size of crowd, its movement and behaviour models provides planners with critical data to aid planning and response.

Recently, a wide range of techniques were introduced for crowd detection and estimation. These techniques range from a grid density method by H. Jacobs [14] to more advanced and accurate methods that require deployment of sensors in the area of interest that are able to collect the required information [6, 15–18]. Vision-based methods, using digital cameras, have proven to be an effective method in crowd estimation [15]. Signal based methods that leverage the ubiquitous adoption of mobile phones with Bluetooth and/or WiFi radios have provided alternative methods to detect and estimate crowds by scanning specifically for the data transmissions generated by these wireless technologies [11, 61].

Unfortunately, most of these methods have proven to be either costly or impractical to deploy within urbane environments or over large areas. Vision based methods are computationally prohibitive and do not scale well. Signal based methods require costly deployment of sensing infrastructure [6, 11, 15, 15–18, 61].

Mobile terminals such as mobile phones are currently equipped with large numbers of embedded sensors that can measure different parameters of their surrounding area. Specifically, mobile devices can use Bluetooth to scan their immediate environment for any other discoverable Bluetooth devices. Employing this capability, Stopczynski A. *et al.* used participatory Bluetooth scanning to infer participants mobility and interactions in large events [10].

Weppner J. *et al.* also used mobile phone based Bluetooth scanning during a Zurich festival to derive citywide crowd understanding [11]. It's noteworthy that both publications assumed 10 meters for effective Bluetooth detection. However, according to the Bluetooth specification and experiments effective detection radius can reach up to a hundred meters.

This chapter presents a novel smartphone based participatory approach with an estimation of the crowd accurately inferred from the probabilistic analysis. The contributions of this chapter are summarized as follows:

- A theoretical analysis of scanning Bluetooth detection probability in terms of distance and time is calculated by considering the independency of clocks on each device and modeling the transmission signal channel. A stochastic approach, attributed to the randomness of the events is taken into account in crowd density calculations.

- Field measurements are implemented to estimate parameters accurately and validate the proposed method. The results show an accurate agreement between the theoretical analysis and experimental results.

The remainder of this chapter is organized as follows. Section 3.2 presents related literature. Section 3.3 formulates the problem and presents an analysis of the detection probability and crowd estimation techniques. Finally, experimental results are presented and the outcomes are discussed.

3.2 Related work

A wide range of approaches have been proposed after Jacobs' grid density method of crowd estimation [14]. With the introduction of new communication and imaging technologies over the last decade, researchers have been able leverage either vision based (digital cameras) or signal based (WiFi and Bluetooth) to improve crowd estimation accuracy. The methods

described in literature can be further categorized into two approaches: "device-based" or "device-free". In the device-based approach, it is assumed that people carry a device that can be detected - for example via wireless signals from a mobile phone or RFID tag. Alternatively, the device-free approach makes no such assumption and does not depend upon devices carried by people.

A popular approach to crowd estimation is to use digital cameras and image processing to detect people and provide an estimation of the crowd. The methods used vary from pixel-level analysis to object-level analysis or a combination thereof [15, 62]. Image based approaches are device-free which is preferred during measurement. However, cameras are only able to cover a limited area and deploying cameras to cover an extended area can prove costly. Further, processing images or video streams from a large number of cameras is computationally expensive. Accuracy is also greatly affected by environmental conditions such as light and shadowing.

The ubiquity of WiFi devices has led to the development of WiFi based crowd estimation. As people are moving in an area, WiFi transmissions leave measurable traces. Measuring variations in WiFi received signal strength indicator (RSSI) between a pair of stationary transmitter and receiver antennas has been used to estimate the number of people located within range of a receiving antenna [57]. More recently, Channel State Information (CSI) has also been explored to improve the accuracy of the estimation by investigating the variations of wireless channel state in different situations [16]. In [61], Domenico *et al* proposed a differential CSI method to provide a rough estimation of the number of people in a room. In [6], Yuan *et al* used a network of deployed sensors within a grid to collect RSSI measurements. A K-mean algorithm was then used to classify the crowd density into different levels. However, the downside of signal based methods is that they are subject to line of sight and signal scattering effects which can affect results. Yamin *et al* used RFID tags along with a wristband to count and monitor crowded events like Hajj in Mecca [17]. In [41], BLE tags

detectable by smartphones are used for crowd detection and allow for an individual's walking route to be reconstructed. However, to determine density, this approach requires people in the area to be tagged. In [42, 63], Bluetooth scanners are used to scan for Bluetooth tags allowing for the estimation of crowd density and also the mobility patterns of people wearing Bluetooth tags. This approach is useful in confined spaces however it does not scale to larger areas or citywide.

To address gaps in image based and signal based approaches, the participatory methods described in [10, 11] proposed to use mobile phones or smartphones as scanning devices that scan for any available devices and use the acquired information to provide a rough estimation of the crowd density. Leveraging these approaches combined with a sufficient number of scanning nodes, any area may be covered at a low cost. However, this approach also requires the participation of people to carry the mobile devices to collect details from the Bluetooth tags.

3.3 Problem formation

This section presents a proposed model, problem formulation and detailed analysis of the detection probability within range of a master node that is scanning for other Bluetooth devices.

Bluetooth devices use an internal clock for timing and frequency hopping to avoid interference. To detect another device, a client should be in inquiry-scan state while listening to the frequency that the scanning device advertises during a specific time slot. As each device uses an internal clock for time and frequency selection, there is a possibility of not detecting other devices due to a mismatch of frequency hops during the scanning period. Furthermore, as with all signals, Bluetooth signals suffer from attenuation over distance. Thus, any drop in the scanning signal strength will reduce both the detection range and

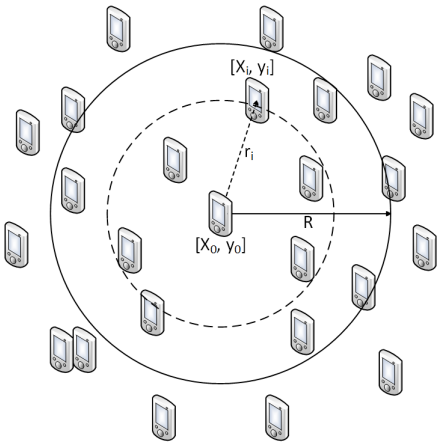

Figure 3.1: System model for analysis.

detection probability within the scanning area. It should be noted that in this chpater, the "master node" is a device that performs a scan for other devices denoted as "slave nodes".

Table 3.1 describes notations and abbreviations in this chapter. To formulate the problem, a 2-D system with N people located at random positions $[x_i, y_i]^T$ in a circle of radius R is considered. It is assumed that the master node is located at the center of this circle at $[x_0, y_0]^T$ as described in Fig. 3.1. The distance between the master node and any slave node device i then becomes $r_i = \sqrt{(x_0 - x_i)^2 + (y_0 - y_i)^2}$. The radius R defines the detection range for a device.

All devices in the system are randomly distributed and work independently. So, the system is modelled by Poisson process with density of λ defined as:

$$\Pr(n) = \frac{(\lambda|B|)^n}{n!} e^{-\lambda|B|} \tag{3.1}$$

This process provides the probability of having n nodes in the area of B.

Failure to detect one or more slave nodes (miss-detection) in the system occurs for the following reasons:

- There is no overlap between the time and frequency domain of a master node and slave nodes.

- The inquiry process expires without obtaining a successful measurement.

- The slave node cannot receive the signal due to signal attenuation (out of range) or the signal is blocked.

Thus, the probability of discovering a slave node within a given distance, r_i, depends on two independent probabilistic events characterized by the following two probabilities:

1. Probability of having both master node and slave nodes operating on the same frequency hop simultaneously, $\Pr(Sync)$.

2. Probability of successfully receiving scanning and response signals at slave node or master node, respectively; $\Pr(P_r(r_i) \geq P_{th} \mid r_i)$.

Hence, the probability of detecting a slave node within a given distance from the master node would be:

$$\Pr(Detection|r_i) = \Pr(Sync) \times \Pr(P_r(r_i) \geq P_{th} \mid r_i) \tag{3.2}$$

Hence the probability of having a slave node within a range of R from a master node detected, can be given by:

$$\begin{aligned} \Pr(Detection) &= \int_0^R \Pr(Detection, r_i = r)dr \\ &= \int_0^R \Pr(Detection \mid r_i = r) f(r_i = r)dr \end{aligned} \tag{3.3}$$

where $f(r)$ is the probability density function of having a device at a distance of r.

Table 3.1: Notation Explanation

Notation	Meaning
Inquiry/ Master/ Scanning node	The node in the inquiry state; which is sending IAC packets
Inquiry-scan/ Client/ Slave node	The node in inquiry-scan state; listening to IAC packets
IAC	Inquiry Access Code
FHS	Frequency Hopping Synchronization
FS	Frequency Synchronization
RB	Random Back-off
τ	parameter of exponential distribution
r	Euclidian distance
α	Path-loss exponent
$\Pr(Sync)$	Probability of having synchronized nodes (concurrent identic frequency-hope)
$\Pr(X)$	Probability of parameter X
P_t	Transmitting power
$P_r(x_{ij})$	Receiving power at node j from node i
P_{th}	Threshold power
$PL(x_i, x_j)$	Path-loss from node i to j
$PL_0(d_0)$	Path-loss at reference distance
d_0	Reference distance (Usually 1 Km)
Z_σ	Zero mean Gaussian random variable with standard deviation σ
ρ	Penetration rate; defined as the ratio of detected Bluetooth devices over the total number of people within radius R
$\Gamma(k)$	Gamma function of k

3.3.0.1 Discovery probability

In [64–66] the authors provide analysis of Bluetooth's discovery and connection process. A Bluetooth connection can be divided into three phases:

1. Inquiry process that discovers neighboring nodes by collecting neighbors' information;

2. Paging procedure that establishes connection between a master node and slave nodes;

3. Piconet formation that starts the network between two sets of master and slave nodes.

A master node in inquiry state (scanning for client nodes) transmits very short ($68\mu s$) packets, referred to as ID packet, with an Inquiry Access Code (IAC). For this purpose, 32 out of 79 available radio carriers will be divided into two 16-frequency trains: A and B. The master node transmits the ID packet at two different frequencies and searches for the response in two continuous time slots. More precisely, Bluetooth devices are equipped with a 28 bit free-running clock that ticks every $321.5\mu s$. The master node sends out ID packets in the selected two frequencies for the first two $312.5\mu s(625\mu s)$ time slots. In the next $625\mu s$ time slot the master node changes its status to inquiry-scan and searches for the response on the previously selected frequencies. In order to overcome the synchronization issues, a $10\mu s$ margin is considered in scanning for the responses. Furthermore, the total time to send and scan for 16 frequencies of each train is 10ms and each train will be repeated 256 times. So, every $2.56s$ a swap occurs between trains. Moreover, every $1.28s$ a frequency will be swapped between trains.

The slave node in inquiry-scan state, listens to one of 32 channels for $11.25ms$. A longer scan window ensures scanning of an entire train of 16 frequency channels. The scanning frequency of each device is chosen based on its clock value and changes every $1.28s$. As a slave node device receives an inquiry packet, it changes the mode to sleep for a uniformly distributed random number of time slots between $[0, 1023]$, also known as random back-off

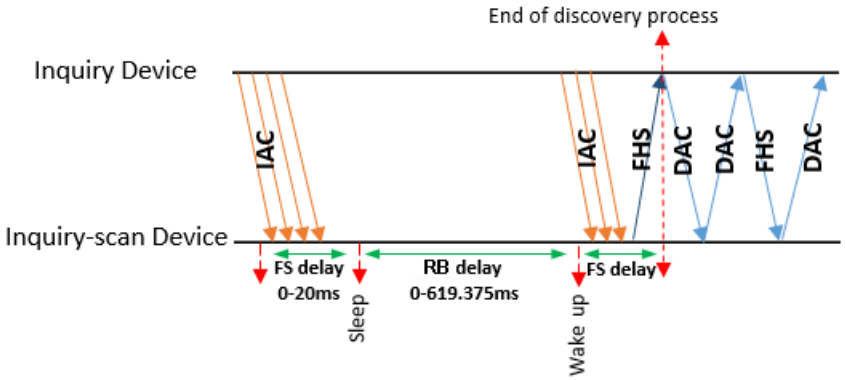

Figure 3.2: Discovery process.

time (RB). This alteration minimizes the collision among devices that are listening to the same frequency channel. The device returns to the scan mode by listening to the previous frequency channel as soon as the back-off time elapses. On hearing the second ID packet from the inquiry device (master node), the slave node waits for $625\mu s$ and then sends an FHS (Frequency Hopping Synchronization) packet, containing ID and clock value of the device. Once the master node receives the FHS packet it then adds the slave node device as one of its neighbors. This process is shown in Fig. 3.2

Considering the discovery procedure described above, the master node should receive the FHS packets from any slave device within range to be able to detect it. The FHS packet will be sent by master node if it receives an IAC packet twice during a period of $FS_1 + RB + FS_2$. The time of receiving FHS packets is an identically and independently distributed ($i.i.d$) random variable that can be modeled to yield an exponential distribution with parameter τ. This process can be denoted as a Poisson process by X. So, the probability of node detection (having synchronized master node and slave node) would be [64]:

$$\begin{aligned}\Pr(Sync) &= \Pr(RB + FS_1 + FS_2 \leq X) \\ &= \int_0^{T_{scan}} \Pr(T \leq x) f_X(x) dx \end{aligned} \tag{3.4}$$

Since the sleep time is uniformly distributed and $\Pr(T_{max} < x) = 1$, then

$$\begin{aligned}\Pr(Sync) = & \int_0^{T_{max}} \frac{x\tau e^{-\tau x}}{T_{max}} dx + \int_{T_{max}}^{T_{scan}} \tau e^{-\tau x} dx \\ &= \frac{1}{\tau T_{max}} - e^{-\tau T_{scan}} \\ &- \frac{(1 + \tau T_{max} + \tau T_{scan}) e^{-\tau T_{max}}}{\tau T_{max}} \end{aligned} \tag{3.5}$$

Where $f_X(x)$ is the exponential distribution with parameter τ, T_{scan} is one period of scanning, $T = RB + FS_1 + FS_2$, and $T_{max} = 659.375ms$.

3.3.0.2 Detection probability

As mentioned, in order to detect a slave node, the master node should be able to deliver IAC packets to the slave nodes and also receive FHS packets from the slave nodes. This process (exchanging IAC and FHS packets) beyond having synchronized nodes, relies on receiving a sufficiently strong signal to be able to read packets. Signal strength between master node and slave nodes varies due to environmental effects such as path-loss, line of sight and obstacles in the environment. These effects can be modelled using log-normal model [67].

To account for the probability of having SINR (Signal-to-Interference-plus-Noise Ratio) greater than threshold in a given distance, we use Log-normal connection model in our analysis. Denoted by P_t the transmitting power, by $PL(x_{inq}, x_{inqscan})$ the path-loss between

the master node and slave node and considering shadow fading, the receiving power would be:

$$\begin{aligned} P_r(x_{ij}) &= P_t - PL(x_i, x_j) \\ &= P_t - PL_0(d_0) – 10\alpha \log_{10}(\frac{x_{ij}}{d_0}) + Z_\sigma \end{aligned} \tag{3.6}$$

where Z_σ is a zero mean Gaussian random variable with standard deviation σ. A pair of Bluetooth devices are connected - can be discovered, if and only if $P_{SINR} > P_{th}$, where P_{th} is the threshold power. Thus, the probability of detecting a Bluetooth slave node within range of the master node performing a scan and located at x_{ij} can be calculated as [67]:

$$\Pr\{P_r(x_{ij}) \geq P_{th}\} = \int_a^\infty \frac{1}{\sqrt{2\pi}\sigma} e^{-\frac{z^2}{2\sigma^2}} dz \tag{3.7}$$

while

$$a = 10\alpha log_{10}(\frac{x_{ij}}{r_0}) \tag{3.8}$$

and

$$r_0 = d_0 \times 10^{\frac{P_t - PL_0(d_0) - P_{th}}{10\alpha}} \tag{3.9}$$

3.4 Crowd density estimation

The most straightforward method to estimate the crowd around each master node is to run a scan for any nearby Bluetooth devices and assuming that each discovered device indicates a person within a given radius. However, even with this assumption we showed

that Bluetooth device detection is a function of random variables due to synchronization and signal propagation with distance and there is a possibility of miss-detection. Furthermore, considering a real world situation, this method may not be accurate due to undiscoverable devices. To take undiscoverable devices into account, we define penetration rate (ρ) as the ratio of discoverable Bluetooth devices to the total number of people within radius R. This ratio would be obtained through field experiments.

$$\rho \triangleq \frac{Number\ of\ people\ with\ discoverable\ Bluetooth\ devices}{Total\ number\ of\ people} \tag{3.10}$$

Theorem 1. *Let K be the number of discoverable Bluetooth devices within an area. Then, K has an inhomogeneous Poisson distribution with density $Z \triangleq \lambda_B \pi r^2 \times Pr(Detection)$;* where $\lambda_B \pi r^2$ denotes the expected value for available Bluetooth devices and $Pr(Detection)$ is defined by *(3.3)*.

Proof. Let M denote the number of people in an area. Then, M has a homogenous Poisson distribution with density λ, representing the number of people per unit area. Therefore, assuming M_B as total number of persons with Bluetooth devices in a disk with a radius of R will be a Poisson distribution with the density of $\lambda_B \triangleq \rho\lambda$:

$$\Pr(M_B = n) = \frac{(\lambda_B \pi R^2)^n}{n!} e^{-\lambda_B \pi R^2} \tag{3.11}$$

Considering the fact that probability of detecting devices are identically and independently distributed, probability of detecting k devices of $M_B = n$ available Bluetooth devices would be

$$\Pr(K = k \mid M_B = n) = \begin{pmatrix} n \\ k \end{pmatrix} [\Pr(Detection)]^k [1 - \Pr(Detection)]^{n-k} \tag{3.12}$$

Thus, the probability of discovering k devices in a Poisson distributed environment is given by

$$\begin{aligned}
\Pr(K=k) &= \sum_{n=k}^{\infty} \Pr(K=k \mid M_B=n) \Pr(M_B=n) \\
&= \frac{[\Pr(Detection)]^k}{k!} e^{-\lambda_B \pi R^2} \\
&\times \sum_{n=k}^{\infty} \frac{[1-\Pr(Detection)]^{n-k}}{(n-k)!} (\lambda_B \pi R^2)^n \\
&= \frac{[\lambda_B \pi R^2 \times \Pr(Detection)]^k}{k!} e^{-\lambda_B \pi R^2} \\
&\times \sum_{n=k}^{\infty} \frac{[\lambda_B \pi R^2 \times (1-\Pr(Detection))]^{n-k}}{(n-k)!}
\end{aligned} \tag{3.13}$$

using Taylor series;

$$\begin{aligned}
\Pr(K=k) &= \frac{[\lambda_B \pi R^2 \times \Pr(Detection)]^k}{k!} e^{-\lambda_B \pi R^2} \\
&\times \left[e^{\lambda_B \pi R^2} / e^{\lambda_B \pi R^2 \times \Pr(Detection)} \right] \\
&= \frac{[\lambda_B \pi r^2 \times \Pr(Detection)]^k}{k! \exp(\lambda_B \pi r^2 \times \Pr(Detection))}
\end{aligned} \tag{3.14}$$

which yields a Poisson distribution as a function of λ and $\Pr(Detection)$. □

By determining the discovery probability and using Maximum Likelihood Estimator (MLE), if k Bluetooth devices can be measured, the crowd density can be estimated as the value of λ that maximizes $\Pr(K=k)$.

3.5 Experimental results

The Bluetooth specification specifies a detection range of up to one hundred meters. However, considering the nature of wireless signals, antennas and various environmental effects, probability of detecting a Bluetooth device varies given distance and environmental parameters. Effects of path-loss and blockage have been analyzed through log-normal model. To verify the analysis, a series of experiments have been designed and implemented. During the experiments, we tried to account for all possible environmental effects such as attenuation, blockage, and effect of crowd by performing tests in different conditions and environments. Fig. 3.3 shows some of the selected environments for the experiments. As illustrated, the chosen environments have various structures and pose different type of environmental and non-environmental effects. Experiments were performed within the campus of University of Technology Sydney and Sydney CBD. To ensure more realistic and accurate measurements, mobile phones are used for both master node and slave node devices during testing. The experiments in this study can be categorized into three main sets. First set of experiments investigate the detection probability of Bluetooth devices. Second set of experiments were designed to drive penetration rate as defined in (3.10). The third set of experiments validates the theoretical analysis based on the experimental results, indoors and outdoors.

3.5.1 Detection probability

The first set of experiments performed target the detection probability of Bluetooth devices. The scanning master node can detect slave nodes if both are operating on the same frequency slot and $P_r(x_{ij}) \geq P_{th}$. Where $P_r(x_{ij})$ indicates receiving signal power within a distance x between nodes i and j where P_{th} is the threshold power. Nexus mobile phones (with Bluetooth version 4.2) are used as measurement devices on both sides (master and slave node) and one scanning period (12 seconds) is considered as the time interval for each

Figure 3.3: Experimental environments

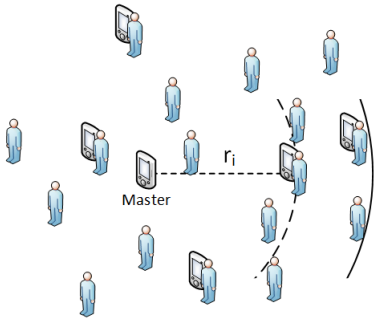

Figure 3.4: Method of experiment to drive detection probability

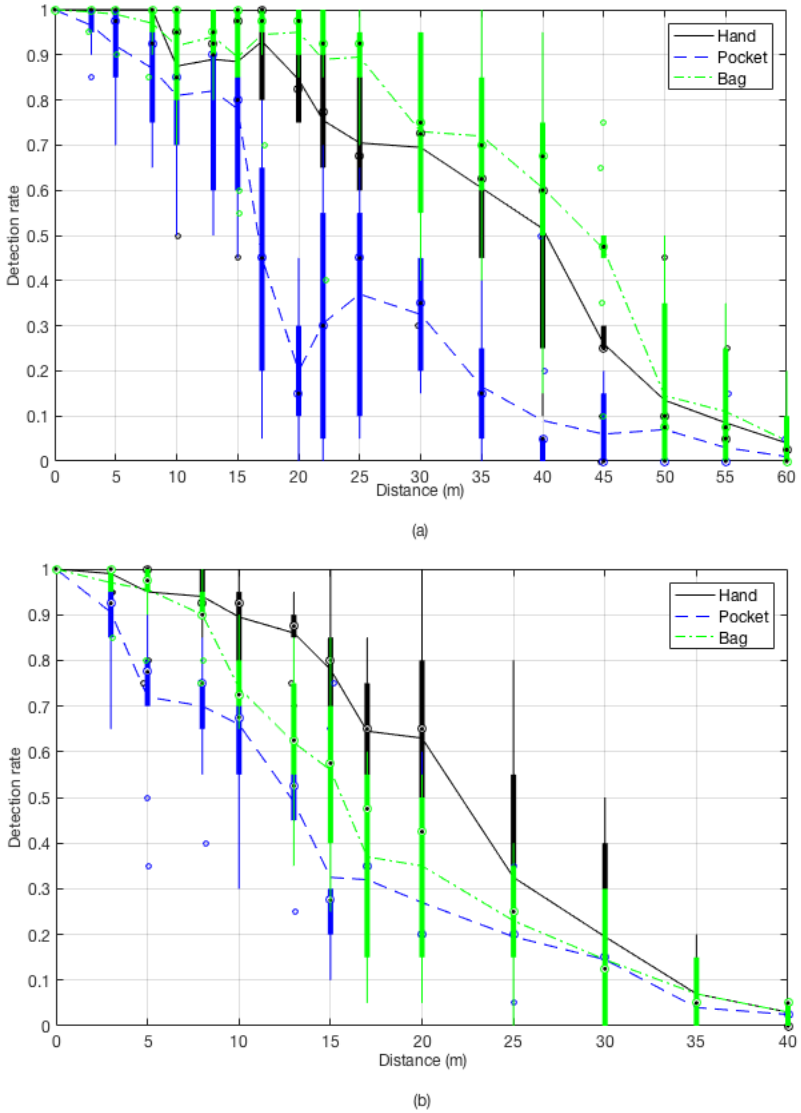

Figure 3.5: Measurement results for various environments and three different methods of carrying a device. (a) Indoors (b) Outdoors

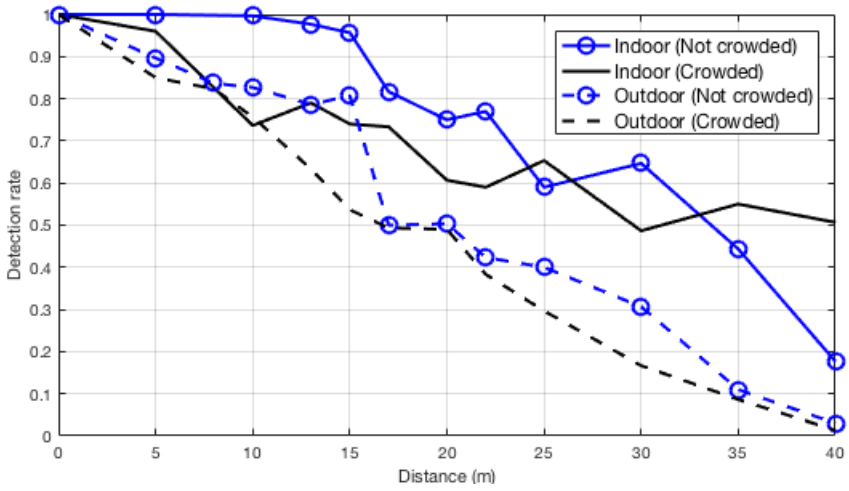

Figure 3.6: Effect of crowd on Bluetooth detection rate.

measurement. All the tests are done in a random environment during sunny and rainy working days. During the early stages of experiments, it was apparent that the effects of the human body and the orientation of how the phones were held or carried could not be neglected. So, the experiments were modified to consider all the possible environmental and non-environmental effects. As shown in Fig. 3.3 the experiments accounted for a variety of different environments with glass-metal design, open concrete structures, and random structures inside buildings with and without human interference. Likewise for outdoor, open green spaces, areas with possible natural blockages such as trees, and areas surrounded by buildings with and without human interference were also investigated.

Fig. 3.4 describes the method of experimentation for detection probability analysis. As shown, the test environment considered as real scenario with random number of people and Bluetooth devices around the master node. For each test, the master node performing a scan was placed at the center of a circle with radius r ($0m \leq r \leq 100m$). A person who is carrying the slave node was moved at the circumference of the circle. Having the slave node moving and standing in different positions helps to have human body effects in the gathered data. Ten data samples were collected for each experiment at each position for both line of sight

and non-line of sight. Furthermore, the experiments considered a phone held in a hand, in a pocket and in a bag. In total, three hundred data samples were collected for each R in both crowded and non crowded environments to consider the effects of human interference. It is noteworthy to mention that the experiments are repeated for ten times in similar conditions and environments to have a reliable data set. Fig. 3.5 represents the average values of the collected data to illustrate the effects of the how a phone is held or carried. Investigating the effects of the crowd on the detection rate, Fig. 3.6 shows the average value of the three hundred samples at every distance for both crowded and non-crowded environments both indoors and outdoors. During this work, we have defined crowded as more than two persons in a square meter. As represented in Fig. 3.5 the lowest detection rate occurs while carrying a phone in the pocket and the highest rate is achieved when a phone is held in a hand. Considering the randomness of the conditions and environments, the average value of all tests for indoors and outdoors is used in detection analysis to take all the possible variations into account. According to the experimental results represented above, the Bluetooth range is greater than the 10 meters described in literature. The range varies indoors and outdoors and can provide a range of 55 meters to 35 meters - while achieving a detection rate of more than 10 percent.

As stated, measured data is used to estimate the values of the parameters in the detection probability using MLE. By substituting (3.4) and (3.7) into (3.2), the probability of detection with a given distance can be calculated as shown in (3.15).

$$\Pr(Detection \mid r) = \int_{0}^{T_{max}} \frac{x\tau e^{-\tau x} dx}{T_{max}} + \int_{T_{max}}^{\infty} \tau e^{-\tau x} dx \times \int_{10\alpha log_{10}(\frac{x_{ij}}{r_0})}^{\infty} \frac{1}{\sqrt{2\pi}\sigma} e^{-\frac{z^2}{2\sigma^2}} dz \tag{3.15}$$

Our study considers static environment during one scan. Thus, the scanning node has enough time to scan its surrounding as nodes are not changing fast during the scanning period. As a result, the synchronisation probability can be ignored. Thus, (3.15) can be reduced to:

$$\Pr(Detection \mid r) = \int_{a}^{\infty} \frac{1}{\sqrt{2\pi}\sigma} e^{-\frac{z^2}{2\sigma^2}} dz \tag{3.16}$$

Where $a = 10\alpha log_{10}(\frac{x_{ij}}{r_0})$. Hence, the unknown parameters are α, r_0, and σ that need to be estimated based on the measurements. However, using the complicated structure of (3.16) in the remaining calculations would result in an overly complex formula. So, as an alternative, a linear model is also considered to fit the measured probability of detection.

$$\Pr(Detection \mid r) = Ar + B \tag{3.17}$$

Where r is the distance between two nodes.

Using MLE, parameters of the detection probability function can be estimated as

$$L(R|\theta) = \prod_{1}^{100} \left[\Pr(Detection \mid r)\right]^k \left[1 - \Pr(Detection \mid r)\right]^{N-k} \tag{3.18}$$

Figure 3.7 shows the obtained PDF (Probability Distribution Function) using log-normal model, (3.16), and linear model, (3.17), fitted to the measurements for indoor and outdoor environments. Each measurement point is the average of a hundred tests in various environments including the means by which a phone is carried.

Having the probability of detection within a given r and using (3.3) the probability of detection can be obtained for indoors and outdoors. Considering a log-normal model:

$$\Pr(Detection) = \int_0^\infty \Pr(Detection \mid r) \times 2\lambda_B \pi r e^{-\lambda_B \pi r^2} dr$$
$$= \frac{\lambda_B \sqrt{2\pi}}{\sigma} \int_0^\infty \int_{10\alpha \log_{10}(\frac{r}{r_0})}^\infty e^{-\left(\frac{z^2}{2\sigma^2} + \lambda_B \pi r^2\right)} r dz dr \tag{3.19}$$

Thus, for indoors the probability:

$$\Pr(Detection) = -0.4\sqrt{2\pi} \int_0^{R_{In}} \lambda_B \pi r e^{-\lambda_B \pi r^2} \left(erf\left(1.18 \log(\frac{r}{28})\right) - 1 \right) dr \tag{3.20}$$

Where R_{In} represents the radius for $\Pr(Detection) > 0.1$ for indoors. And, outdoors:

$$\Pr(Detection) = -0.4\sqrt{2\pi} \int_0^{R_{Out}} \lambda_B \pi r e^{-\lambda_B \pi r^2} \left(erf\left(1.05 \log(\frac{r}{18})\right) - 1 \right) dr \tag{3.21}$$

R_{Out} is the radius for $\Pr(Detection) > 0.1$ for outdoors. Also, taking the linear model into account:

$$\Pr(Detection) = \int_0^\infty Pr(Detection \mid r) \times 2\lambda_B \pi r e^{-\lambda_B \pi r^2} dr$$
$$= \int_0^\infty (Ar + B) \times 2\lambda_B \pi r e^{-\lambda_B \pi r^2} dr \tag{3.22}$$

For indoors:

$$\Pr(Detection) = \int_0^{R_1} 2\lambda_B \pi r e^{-\lambda_B \pi r^2} dr + \int_{R_1}^{R_{In}} (1.048 - 0.016) \times 2\lambda_B \pi r e^{-\lambda_B \pi r^2} dr \quad (3.23)$$

Where $R_1 = 3m$ indicates $\Pr(Detection) = 1$. And, outdoors:

$$\Pr(Detection) = \int_0^{R_{Out}} (1 - 0.022r) \times 2\lambda_B \pi r e^{-\lambda_B \pi r^2} dr \quad (3.24)$$

3.5.2 Penetration rate and crowd estimation

To estimate the crowd, we have defined a penetration rate, (3.10) that will provide the average ratio of discoverable devices over the number of people within the radius R. Radius R is determined according to the measurement conditions (section 3.5.1) - 35m for outdoors and 55m for indoors. Two hundred tests have been done in randomly chosen indoor and outdoor environments to determine the penetration rate. During each test, the Bluetooth measurements have been repeated five times to assure the quality of gathered data. To drive the penetration rate, the number of devices was recorded and averaged over five repeated tests. Simultaneously, the number of people within the detection radius were counted and recorded. Then, the penetration rate for each test was calculated and a final penetration rate was determined as the average value for all the results.

Based upon the analysis mentioned in Section 3.4, we estimate the crowd around each master node. Substituting detection probability functions of (3.20), (3.21), (3.23) and (3.24) into (3.13) and solving for λ to maximize $\Pr(K = k)$ will give us an estimation of the

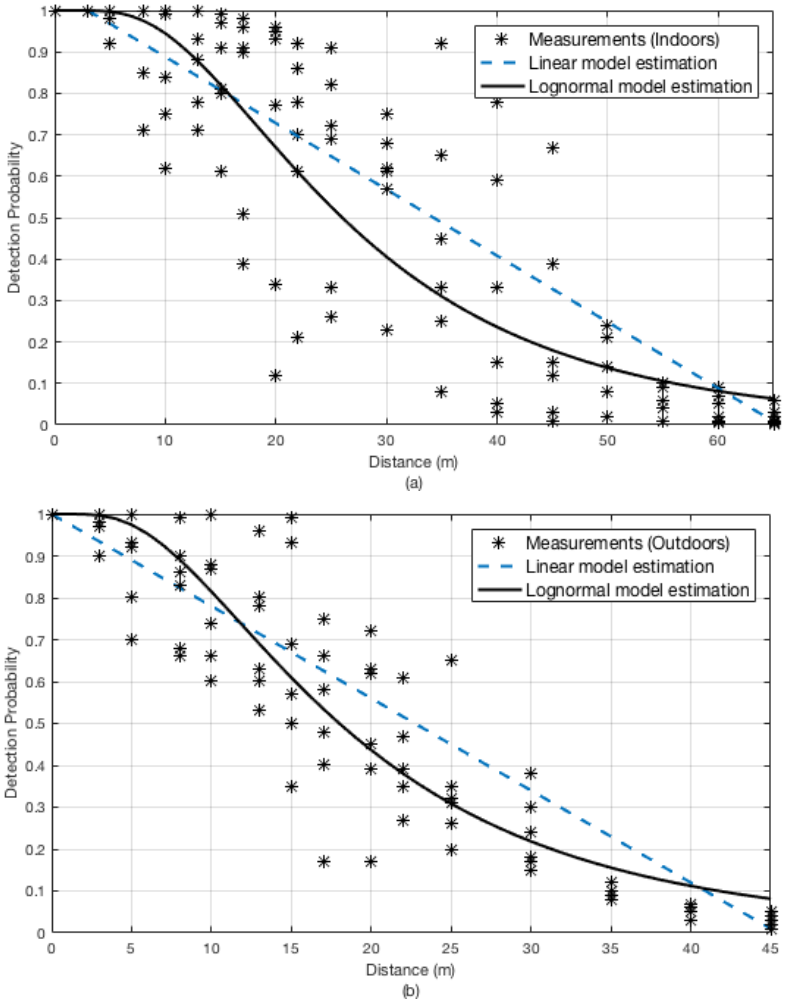

Figure 3.7: Measurement results for detection probability, and estimated log-normal and linear models. (a) Indoors (b) Outdoors

crowd around each node. As mentioned, maximum value of λ for any given number of devices, provides the mean value of the density according to the detected number of devices. The analytical results also can provide the variation in the calculated density to cover the variation of the measurements.

To illustrate the accuracy of the analytical results, Table 3.2 provides a comparison of the estimated mean values for both models in 3.5.1 and the average value of twenty random experiments for a given number of devices both indoors and outdoors. It also represents the error value as the ratio of absolute difference of estimated and experimented values to experimental values. As demonstrated in Table 3.2 and due to the availability of the data, three different numbers of devices were considered. Estimated values have been divided into two sections to compare the results for both linear and log-normal models. For indoors environments with one available Bluetooth device, the estimated value is 6 people (with the density of 0.041) using the linear model and 9 people (with the density of 0.059) using the log-normal model while the actual value for one available device is 7 people (with the density of 0.047) on average. For outdoors environments with one available Bluetooth device, the estimated number of people is 22 people (with the density of 0.0047) using linear model and 41 people (with the density of 0.0138) using the log-normal model while the actual value for one available device is 43 people (density of 0.01) on average. Comparing the results and errors, it can be concluded that for indoor environments the linear model is acceptable. However, for outdoor environments the linear model results are not acceptable and log-normal model should be considered as the main model.

3.6 Testbed design (Mobisensing)

Static scanning nodes in traditional systems provide limited coverage area, which makes citywide coverage infeasible. Mobile crowd sensing yields more coverage than traditional

Table 3.2: Estimated value for crowd and error rates.

	Num. of nodes	Estimated value		Experimental value	Error	
		Linear model	Log-normal model		Linear model	Log-normal model
Indoor	1	(0.041) 6	(0.059) 9	(0.047) 7	12.8%	25.5%
Indoor	2	(0.081) 12	(0.095) 14	(0.073) 11	10.9%	30.1%
Indoor	3	(0.122) 18	(0.13) 19	(0.107) 16	14%	12.3%
Outdoor	1	(0.0074) 22	(0.0138) 41	(0.01) 43	53%	38%
Outdoor	2	(0.0143) 42	(0.0222) 66	(0.02) 62	28.5%	11%
Outdoor	3	(0.0213) 63	(0.0297) 88	(0.022) 64	3.2%	35%

systems due to the mobility of the users. Given a sufficient number of participants in a region and considering the spatio-temporal correlation of the data that the users submit, a full coverage of the region will be established. On the other hand, the mobility introduces some challenges in data interpretation such as the sensing quality. Having an accurate understanding of the environment requires accurate measurements, which can be affected because of the mobility of the users.

3.6.1 Test-bed preparation

Understanding the crowd's behaviour in a wide area requires a large set of data, which is associated with the time and location. To this end, a test-bed has been designed. The test-bed consists of two parts:

- An Android phone application, *MobiSensing*, that collects the required information.

- Data visualisation that maps the processed data into Google Maps as an overlay.

3.6.2 Framework of *MobiSensing*

MobiSensing is an Android-based app that runs as a background application. This application records locations through the Google location provider and scans for WiFi access-points and Bluetooth devices every 30 seconds. To preserve the anonymity, the application assigns an ID to each device and uploads data using its assigned ID. Furthermore, the application is equipped with a pedometer to increase the location and mapping accuracy. Information is uploaded to a central server from all available devices. This information is processed on the server, and the outputs are represented as a layer on top of Google Maps.

3.6.3 Key challenges

Using the participatory *MobiSensing* app, one can sense only part of the spatially and temporally associated data, which indicates several research challenges.

- Gathered data quality: Given a set of data, how can we assure that the received data are reliable? One of the greatest challenges is the location accuracy, which sometimes is as low as 500 meters.

- Data integration: The spatially and temporally correlated gathered data from various devices should be assigned to the actual location and time. Furthermore, several devices can upload large quantities of shared data. All of this information should be distinguishable to derive meaningful data for analysis.

- Data mapping: Given a set of spatially and temporally associated data, a flexible data mapping system is required to intelligently manage data in the process.

3.6.4 Data quality

The analysis and accurate outputs are highly dependent on the gathered data quality. Considering the circumstances of the sensing conditions, e.g., the way of carrying the phone, walking speed, and network issues, there is a possibility of having missing or corrupted data. Thus, there should be techniques to guarantee the quality and accuracy of data. Moreover, a large quantity of data is transferred through mobile phones. This number of data should be handled properly.

To overcome the aforementioned issues, some techniques are implemented as follows:

1. High degree of data access optimisation
2. System for easy data validation and evaluation to ensure validity
3. Modular implementation of the system that allows scaling in various environments to accommodate the rising computational and storage requirements.

These techniques are further discussed in the remainder of this section.

3.6.5 Data integration

Received data contain location, timestamp, and a unique serial number of all the detected devices. The system will map the location into the triangular grids. Then, the system calculates the Euclidian distance of the centre of the mapped triangles; if it is smaller that the threshold (55 m), then the system will start to read the time and detected device table. All overlapped data are identified, and the final results are projected to the map.

3.6.6 Data mapping

A flexible data mapping system is required to properly handle the data association and processing. Based on the requirements of the project, the data mapping system should

be capable of providing meaningful visualisation of data for quick validation and in-depth analysis.

As one passes urban areas, especially those with high skyscrapers, the accuracy of GPS and mobile network localisation dramatically decreases. According to our tests, the location accuracy is 5 to 500 m. Thus, the spatial association of data becomes a challenging issue. The data mapping system should be able to handle the less accurate data as a core functionality.

Due to the number of data, the provided technique should be sufficiently fast to ensure that on-demand access is possible. Furthermore, the method should ensure that data processing and data retrial can be simultaneously performed.

- The requirement of function primary indicates that for calculations, visualised data must be accurately tied to estimations without middle-ware.

3.6.6.1 Data Mapping: Self tessellating spatial mapping solution

The system was first developed with a simple sampling database, which tracked all submitted data to plot them on the map. A basic implementation was quickly found to be unusable because most submission points overlapped and had a high degree of localisation inaccuracy. Thus, the system must be capable of interpreting and processing data accordingly while providing meaningful results. Additionally, it has been determined that fixed area mapping is difficult; sampling the entire city at meaningful resolution is possible with traditional mapping methods, but it would require significant processing power, and there are many unused sampling areas, as cities do not neatly fit in rectangular areas.

The developed solution organically addresses all of those issues from the base model implementation. The system uses a dynamically generated mesh to wrap the requested areas with base data elements of a fixed size regardless of geographical position. The resultant mesh is highly compact and only wraps areas with actual data, which also enables a system deployment in any other city or even country with no changes to the mapping. This structure

also enables cooperative system mapping, where multiple servers are responsible for their own area but can synchronise the data together for the master server to provide access to the full map, since the mathematical model to generate a mesh is fully predictable.

This solution also enables very quick selective queries for specific areas; the result has a variable resolution that depends on a query, and boundaries can be drawn over the model to separate the areas for precise sampling purposes. Due to the associative structure of the model relative to each sample, queries can be performed for each selected time frame in the area without requiring model snapshots.

Most importantly, the model enables a dynamically defined resolution and can accommodate varied samplings and associate them based on the data layer and to different model depths if required while allowing a quick computation with only a linear relation to the data access speed, as well as an exponential data density relation.

Such structure is much easier to visualise in terms of data relation, but its grid-less structure creates issues with visualisations, which were solved during development and were used as a graphical overlay for Google Maps in a web browser to show a data mapping to commonly used map service in order to allow easy data browsing and validation.

The data sample associative process is complex in nature. When a sample is received, the system associates it through the model to its required depth and expands the model if necessary to accommodate it while ensuring that the model selection is valid. The sample accuracy is also considered by a model, as it will define an area that this sample can potentially affect. When a final level of model is reached, the currently active samples in a selected area are compared, where the system decides whether the sample data must be set over other associated samples, to finalise a selected area. The mechanism of data selection varies depending on the associated data, but it primarily revolves around consideration of the sample value and precision. Higher-precision samples are commonly considered over lower-precision ones to associate in a model. When finished, a summary will be generated. However, all

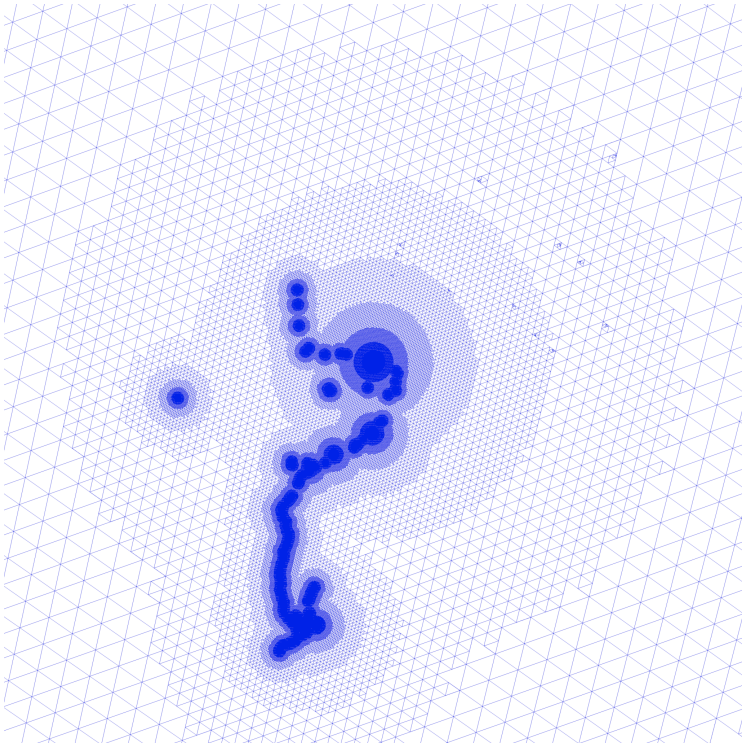

Figure 3.8: Sample Mesh of the Model

samples are recorded to the model as associative links to the area with a certain strength to allow a consideration of other samples of the area, using a data processing algorithm to obtain a finalised result or a time frame selection, where the samples can be retrieved with their associated model and quickly compiled to the valid model for that particular time frame. One does not have to store the sample for each case, though that is certainly possible if the request times are critical.

The model uses an optimised set of mathematics to ensure a good performance when attempting to map the data. Many critical components must be computed each time a sample must be associated or found.

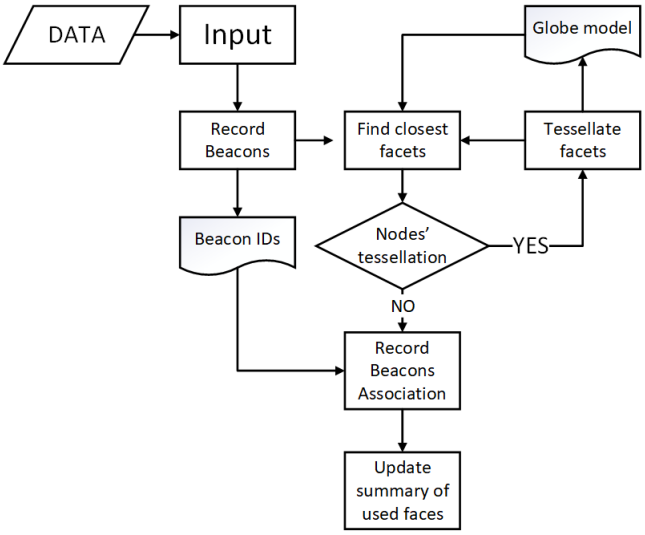

Figure 3.9: implemented approach for data storage and mapping.

3.6.7 Model storage

3.6.7.1 Theory and structure

The data storage structure (layer zero for irregular icosahedron) enables an $O(n)$ computing time to access a specific node or area of nodes on the data model, where 'n' is the depth with a sample density that increases by (20×4^n) for each layer [68–70]. However, by reusing data from the previous layer, a memory impact is lessened and only results in (20×3^n), which can be later optimised to (20×2^n) if some data are omitted and generated on request. The mentioned values are only true for fully tessellated layers. In practice, the system only requires a fraction of the structure to cover a target area. Fig. 3.9 provides the flow chart diagram of the implemented approach.

The fundamental property of the introduced model is its optimisation for radial selections, where the data access and storage are optimised around circular areas, which suits perfectly for application. Although any shape is technically supported, the original request must be done with a circular area request.

A distinct hierarchical model is utilised for storage purposes, where each element may

contain another layer, and the system may tessellate future layers on any node in a model if it was not tessellated. Using the relational storage, each node must contain: 3 distinct three-dimensional vectors to form a triangle for the node and a node normal, which represents a triangle centre. Each node receives a unique ID, which is used for data association, but only the final layer of the model contains data association, and all other layers have summarised associations, which update if the new associated data would alter them.

3.6.7.2 Practise

Unfortunately, the functional system does not follow the estimated values as strictly as predicted. This is not a fault of the structure, but rather, the structure generally contains a large volume of data, which results in storage solution, where the data are spread, and the seek time is difficult to account for.

3.6.8 Model access

The model is accessed through a mathematical comparison, as the nodes cannot be linearly addressed and arranged with spatial coordinates. Few techniques were used to ensure a valid and functional data selection during normal usage, even with few specific corner cases that may occur during system usage. It is noteworthy to mention that the accuracy of the measurements can differ in especially in city centres with skyscraper. So, triangle meshes are used to reduce the error of mapping especially with poor location measurements. Furhtermore, it should be understood that the circular selection does not perfectly fit the triangular grid, and special considerations must be considered. Hence, a supplied target radius has a slight correction to ensure that the wanted elements are selected.

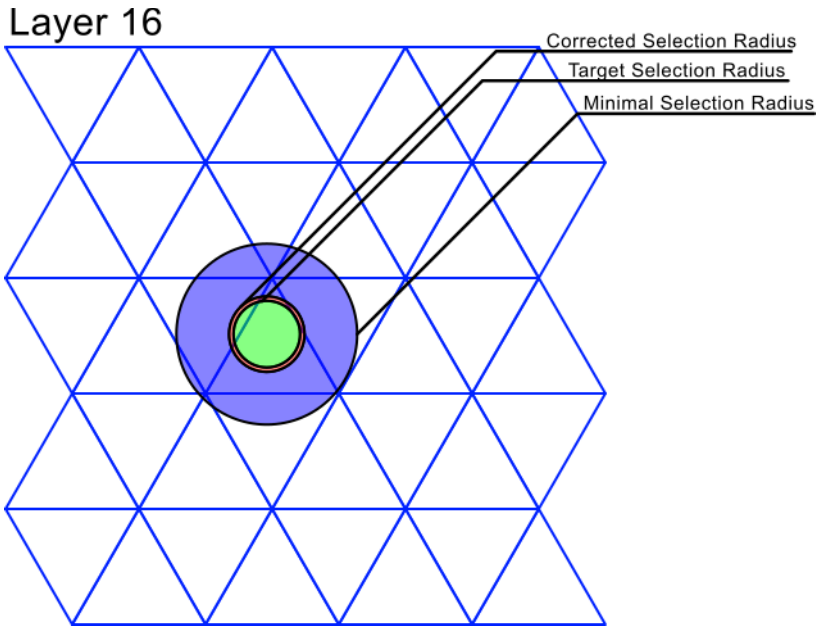

Figure 3.10: Intermediate Layer Selection

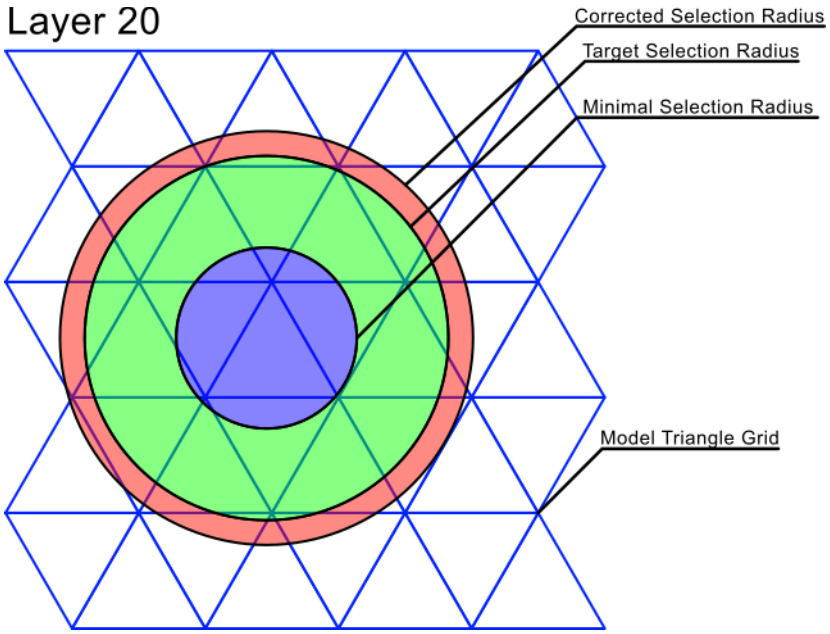

Figure 3.11: Final Layer Selection

3.6.9 Data validation

To validate the received data in the server, the server acknowledges the receipt of the data to the provider ID. This batch contains the necessary information about the received data, with which the phone can verify the proper data transference.

3.6.10 Prototype Implementation

Through problem analysis and experimentation, several prototypes were developed to ensure the best fitting result, but a few changes were applied to the common methodology to ensure that the development time was reduced while maintaining a high resultant software quality.

3.6.10.1 Architecture

The prototype was unconventionally implemented, where the architecture was first designed in a program after which the algorithms for interoperation were made. This process was done to ensure that the supporting structure and the data to be stored could first be defined; then, the retrieval and access methods were designed. This approach minimised the number of prototype iterations, where a nearly complete structure was derived in the shortest possible time. Most changes were added iteratively to accommodate various intermediate data, which must be tracked and computed.

3.6.10.2 Experimental setup

The prototype was developed as asynchronous PHP and JS application, where two distinct modules operate in tandem to allow a model access.

The designed test-bed is in use to collect the required data. We have 12 mobile phones running, collecting and uploading data all over Sydney. The collected data is uploaded to the server which runs the algorithm to extract locations and crowd density. The results of

the analysed data are shown on the "MobiSensing" web page.

3.7 Conclusion

In this chapter, we presented the analysis of crowd estimation using Bluetooth in mobile phones. The analysis investigates the probability function of the Bluetooth device detection according to the distance and time for better estimation. Field measurements were used to estimate the parameters of the probability function and validate the analysis. In this approach, unlike most methods, the scanning node is mobile and scans the environment while moving. There is also the possibility of having several nodes in the area while providing some overlapped information. To model the system in this situation, we modelled the mobile node in a one-dimensional environment and extended it to two-dimensional systems.

The main goal of this study is to provide a solution to use mobile crowd sensing and integrate the data with the infrastructure. To reach this goal, a test-bed was designed and implemented to collect the required information using an Android application and upload the data to the central processing unit. The data are processed in the central server, and the results are projected as a layer on top of Google Maps.

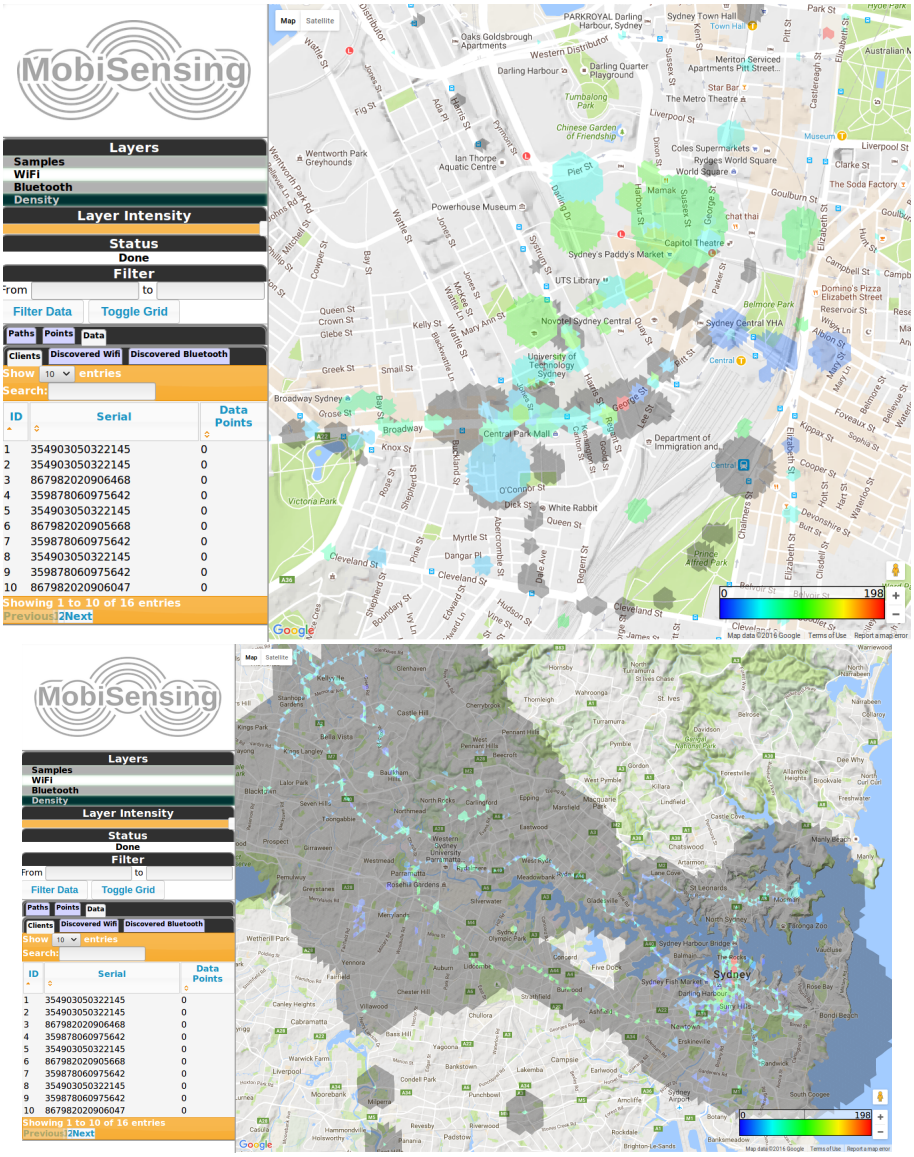

Figure 3.12: Implemented system

Chapter 4

Crowd Density Mapping Based on WiFi Measurements on Train Platforms

Crowd distribution is a challenging issue in the management and design levels. This chpater provides a passive method to derive the crowd density distribution using WiFi measurements on a real scenario. Six WiFi Access Points (AP) are deployed in the platform 2/3 of Redfern station, Sydney to monitor the platform for a week. Based on the probability maps that are built using RSSI measurements and prior knowledge, the crowd distribution is calculated on the platform and its results are compared with distributions acquired from CCTV images. Final density heat maps are in good agreement with the acquired results from CCTV cameras.

4.1 Introduction

Understanding crowd behavior and its distribution is always a critical matter in terms of planning, management and safety. To this end, one needs to detect people and map them into the area to be able to determine the density and its distribution. There are several methods to detect people such as CCTV camera images [71, 72], RFID tags [40], WiFi [13, 73–75] or Bluetooth [4, 50] probing and etc. Analyzing the images of CCTV cameras can provide an accurate estimation of the number of people in the area. However, the coverage of the video cameras is limited and it's not possible to install them anywhere. Moreover, processing the images of the video cameras are computationally expensive. Using techniques such as reading RFID tags, requires huge participatory of people to carry the tags around in addition to the FRID readers installation. Meanwhile, pervasive existence of smart phones makes WiFi scanning more suitable method in detecting people.

Using WiFi scanning raise two main challenges. First challenge is to provide an accurate estimation of the number of people within the scanning range, considering the probability of having unavailable or undiscovered WiFi nodes. To address this issue, we use the same method of penetration rate described in chapter 3 for Bluetooth scanning. Second challenge in using WiFi scans, is to locate the detected nodes and map it into the area to derive the density distribution map. Researchers have been focused in localizing the node using WiFi signals for the last decade. Most of the localization methods are based on the RSSI measurements and channel modeling to estimate the location [58, 76–78]. WiFi fingerprints, which is another approach in localization, is also reading RSSI values in different points and comparing the fingerprints with measured values [75, 79, 80]. These measurements are usually done on the carrying device, such as mobile phones, to estimate the location of the user. This approach is not applicable in crowd density estimation project, since the scanners (WiFi Access Points) should collect data and locate the nodes. So, a similar approach is

introduced to locate the nodes in the area using WiFi fingerprints.

Furthermore, using any of the introduced methods requires large number of data samples to be able to locate the node properly. Thus, localization process becomes more challenging with the limited number of measurement samples. People getting off the train are usually walking fast to reach the gates as soon as possible. So, the detection and RSSI values can be changed very fast during this time. All these will result in having a sparse data samples.

This chapter presents a method to estimate crowd density and its spatial distribution based on RSSI measurements on WiFi access points on a train platform in Redfern station, Sydney. To the best of our knowledge, this is the first time of using the measurements on the APs to locate the nodes in the area. Considering the limited number of measurement samples, a probabilistic method is introduced to create probability map instead of exact fingerprint map to help locating the nodes and deriving the density distributions. The main contributions of this chapter can be summarized as:

1. Localizing the nodes based on the received signal strength measurements on each AP using probability map which is constructed based on fingerprint map

2. Crowd Density Estimation using multiple WiFi APs' scans

3. Determining spatial distribution of the crowd using above steps

Understanding spatial distribution of the crowd relies on describing RSSI accurately and conquering with the non-gaussian noise from interference, reflection, and fading. The remander of this chapter is organized as follows. Section 4.2 defines the problem and challenges that should be conquered. Proposed solution is described in Section 4.3. Section 4.4 describes the experiments and discuss outcomes of the research and final conclusion is presented in section 4.5.

It should be noted that CCTV images along with WiFi scanning data is provided by Sydney Trains on this project.

4.2 Problem statement

Ubiquity of WiFi technology and representation of specific characteristics in different situations made it a practical solution in crowd estimation and device localization. Leveraging characteristics such as location-specific RSSI values enables one to determine the spatial distribution of available devices. Although WiFi probes are very useful in detecting available nodes, locating the nodes while they are not engaged is quite challenging. To define the problem, the scenario on the platform has been described and then the challenges are specified.

4.2.1 Experiments and data collection

The experiments and data collection, have been done on a train platform (Platform 2/3) in Redfern station, Sydney. Fig. 4.1 represents the test environment with a small cabin, available seats, and six APs installed on the platform for scanning purposes. Part of the platform that is covered with metallic shades are also indicated in Fig. 4.1. During the experiment, the whole platform is divided into $1m \times 1m$ grids; which the centers are indicated by dots. All APs scan the area continually and record timestamps and RSSI values for any detected device. To satisfy privacy preservation, any individual node indicated with a unique hash ID.

To determine crowd density, the easiest way is to count the number of available individual devices appear in each AP as scans its coverage environment. However, there is a high chance of missing a node due to packet collision, signal attenuation or blockage. Furthermore, a recent feature on phones which enable them to create dynamically changing MAC addresses can result in multiple detections of the same node over a specified period of time.

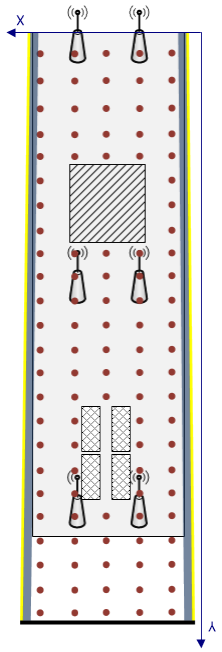

Figure 4.1: Test environment and problem statement.

4.2.2 Spatial-Temporal variation of signal

Recorded RSSI values are the main characteristics to localize a node. However, the received value of signal strength can vary in time due to various reasons such as blockage, OS of the devices, and battery level of the device. Furthermore, WiFi security and power saving approaches results in a very spars data; specially, on the peak hours while people are in rush and moving fast. According to the WiFi protocol, while an AP listens to the probe requests coming from the devices if the device receives reply from an AP, it will initiate association process. Otherwise, it will go to sleep mode for a random period. This process causes issues in localizing the nodes due to the detection intervals.

4.3 Proposed approach

Realizing an estimation of crowd distribution can be divided into two steps. First step is to have an understanding of the number of nodes in the platform. Then, location of each node

should be determined to map it on the platform.

4.3.1 Localization

As mentioned, each AP listens to the probe requests of devices and by hearing the request, records RSSI values of the receiving packets. To find the location of a node based on the WiFi signal measurements several methods have been introduced. Use of fingerprint map based on prior measurements is one of the promising techniques [81–84] [85]. In this technique, WiFi signal will be measured in the space time domain and then, new measurements will be compared to the recorded values to estimate the location of the node. In this section, the WiFi signal fingerprint map construction approach and its issues on dealing with limited sample numbers of data will be discussed. Therefore, a new approach will be introduced to minimize the uncertainty of fingerprint map based localization in dealing with a sparse dataset.

4.3.1.1 Fingerprint and Probability map construction

The experiments on this project was based on passive scanning process [4] which results in a sparse set of data specially during rush hours; while people are trying to reach out or get into the train as soon as possible. Considering the average speed of people during these hours and WiFi random back-off protocol the number of samples that can be recorded are limited. The limited number of data leads to a very challenging issue in terms of localization and node mapping.

Given a set of APs, $AP = \{AP_1, AP_2, AP_3, ..., AP_N\}$ where N is the number of APs in the test field $\mathcal{F} \subseteq \mathbb{R}^2$. The field, $\mathcal{F}$, is divided into $1m \times 1m$ grids and large number of received signal strength samples is recorded in each AP from a device on the cell, C_{ij}. Where i and j are indicators of row i and column j in the grid. So, the signal signature of any WiFi device on each cell can be described as $Signature(C_{ij}) = \left\{S_{ij}^1, S_{ij}^2, ..., S_{ij}^N\right\}$. S_{ij}^N represents recorded

signal strength on AP_N from a device at cell ij. Assuming the receiving signal from cell i and j in AP N as

$$x_{ij}^N = S_{ij}^N + n \tag{4.1}$$

Where S_{ij}^N is the actual value of the receiving signal and n is a spatially uncorrelated zero mean Gaussian noise. The probability of the location can be formulated as a Gaussian probability:

$$\Pr(L_{ij} \mid x_{ij}^N) = \frac{1}{\sigma\sqrt{2\pi}} \exp(\frac{1}{\sigma^2} \parallel x_{ij}^N - S_{ij}^N \parallel^2) \tag{4.2}$$

During this project, we assume that the node k is on a 2D environment and its position at time t can be described as $X_t^k = \begin{bmatrix} x^k & y^k \end{bmatrix}^T$ which is mapped to the center of cell that it's associated. Assuming that the average value for signal strength can be measured from any AP within each cell. Then, we have a tensor describing WiFi RSSI measurements within each cell. To determine the position of each node, we define the probability function of the position as $f(X_t^k = x_t^k)$. Thus, considering the measurements of each AP and assuming that measurements are $i.i.d$, the probability of having the node in cell C_{ij} will be

$$f\left(X_t^k = C_{ij} \mid measurements\right) = \prod_{l=1}^{N} f\left(S_{ij}^l \mid x_{ij}\right) \tag{4.3}$$

Having measurements for device k at time t as z_t^k, we aim to estimate node's position, $\hat{x_t^k}$, for the state x_t^k. Thus, the system can be modeled as follows; using particle filters:

$$x_t^k = g\left(x_{t-1}^k, w_t^k\right) \tag{4.4}$$

$$z_t^k = h\left(x_t^k, v_t^k\right) \tag{4.5}$$

Where $g(\cdot)$ is the transition function from state x_{t-1}^k to x_t^k and $h(\cdot)$ is the measurement function. $w_t^k \sim N(0, Q)$ and $v_t^k \sim N(0, R)$ are noise with covariance matrices $Q = diag\left(\sigma_x^2, \sigma_y^2\right)$ and $R = diag\left(\sigma_1^2, ..., \sigma_N^2\right)$, respectively.

Deriving the fingerprint map based on the experiments helps to determine locations more accurately. However, localization with this method requires enough number of measurements due to temporal variation of the RSSI measurements. To overcome this issue, probability map is introduced. Using this method, a probability will be assigned for every measurement and the expected value for each cell will be calculated using assigned probabilities.

It is noteworthy to mention that in this map, the grids that are blocked with different obstacles will receive the value of zero as the probability of existence.

4.3.2 Leveraging prior knowledge

As mentioned above having limited number of samples of received signal strength poses tremendous challenges in finding the location of each node. Leveraging prior knowledge can help to compensate the lack of samples. To acquire this knowledge, the platform is monitored for a day. It is noted that people trying to avoid the middle of platform due to the obstacles such as pillars and seats. They also tend to stay on the side that train stops. However, some try the other side of platform for faster walk. Considering all these observations, the distribution on the X-axes of the platform (as illustrated in Fig. 4.1), according to the trains' timetables, can be modeled using Gaussian mixture model with variable variance values as shown in Fig. 4.2.

$$f(x) = (1 - \alpha)g_1(x) + \alpha g_2(x) \tag{4.6}$$

Where $g_i(x) = \phi_{\theta_j}(x)$, $\theta_j = (\mu_j, \sigma_j^2)$.

On the other hand, people form a nearly uniform distribution as reaching the concourse

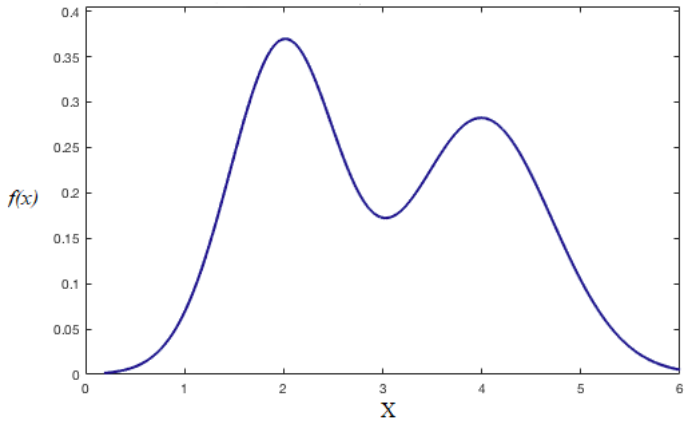

Figure 4.2: Distribution on the X axes of the platform.

as shown in Fig. 4.3. This phenomena can be modeled by defining variance of the Gaussian mixture model as a function of Y-axes (distance from concourse). So, a multi-dimentional model obtained which provides the distribution of the platform.

$$f(x) = \sum_{i=1}^{K} \alpha_i g(x \mid \mu_i, \Sigma_i) \tag{4.7}$$

$$g(x \mid \mu_i, \Sigma_i) = \frac{1}{\sqrt{(2\pi)^k \mid \Sigma \mid}} \times \exp\left(-\frac{1}{2}(x - \mu_i)^T \Sigma_i^{-1} (x - \mu_i)\right) \tag{4.8}$$

where α is the weight and g is the Gaussian distribution with mean of μ and standard deviation of Σ. This probability function is used to adjust the final probability map of crowd distribution aiming for better accuracy.

4.3.3 Crowd estimation and crowd distribution

The most straightforward method to estimate the crowd around each AP is to run a scan for any nearby device and assuming that each discovered device is indicating a person within a given radius. However, even with this assumption, device detection is a function of random

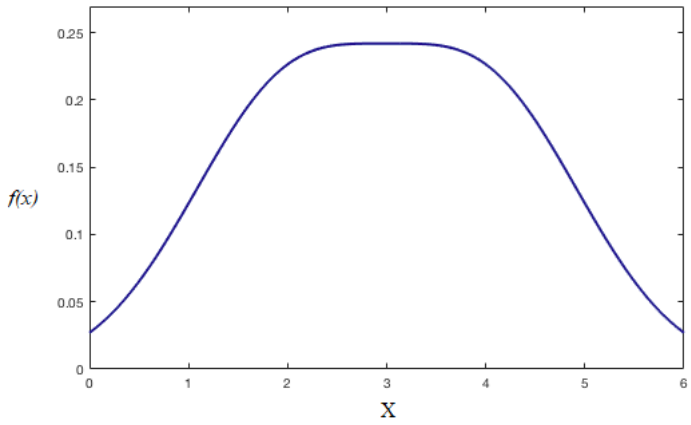

Figure 4.3: Distribution on the concourse entrance.

variables due to synchronization and signal propagation with distance and there is a possibility of miss-detection. Furthermore, considering real world situation, this method may not be accurate due to undiscoverable devices. To take undiscoverable devices into account, we define penetration rate (ρ) as the ratio of discoverable devices to the total number of people within radius R. This ratio would be obtained through field experiments.

$$\rho \triangleq \frac{Number\ of\ people\ with\ discoverable\ Bluetooth\ devices}{Total\ number\ of\ people} \tag{4.9}$$

Considering the probability of having a node in cell i and j, the expected value of the number of people in each cell is determined as

$$\mathbb{E}(\text{Number of people}) = \sum_{i}^{M} 1 \Pr(L_{ij}) \tag{4.10}$$

4.4 Experiments

The experiments are done on platform 2/3 of Redfern station, Sydney. Fig. 4.4 provides layout of the platforms in the station. Sydney Trains provided facilities and managed data

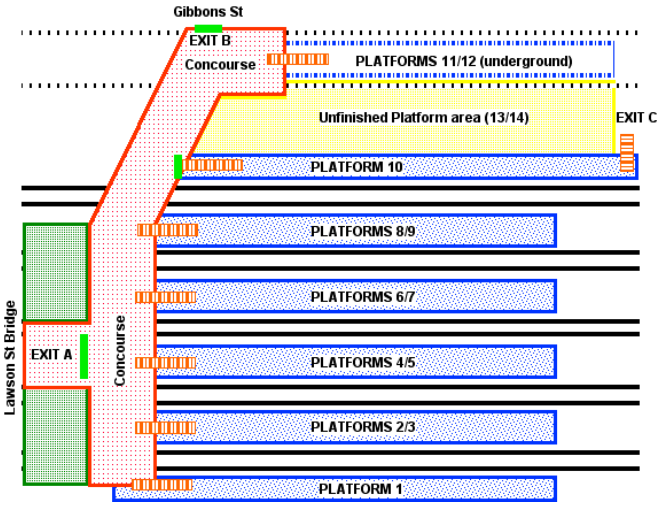

Figure 4.4: Map of Redfern train station [https://www.triposo.com/poi/N_603520919].

collection on the platform during the experiments. The experiments were divided into two sections. In the first section, we have recorded data to extract fingerprints and probability map of the platform. As it is clear, there is a small gap between platforms, around 13 meters . Therefore, adjacent platforms (1 and 4/5) also considered during the experiments and initial data collection. Then, CCTV images and WiFi data is collected for a week to provide and estimate the crowd density map. Final results are compared with the results of CCTV images to validate the approach.

4.4.1 Fingerprint map extraction

To drive the fingerprint map for the platform and considering our limited access to the data collection systems, we have to design series of experiments to derive the RSSI values at the center of the grids as described in Fig. 4.1. To collect RSSI values, three participants with six different mobile phones followed predefined rules. Each person had a Nexus 6p and one other phone (Samsung, Apple, Sony). The platform divided into three sections for the measurements and defined different paths for each person as shown in Fig. 4.5. Each person followed the defined path while standing steady at the centre of each cell for a minute.

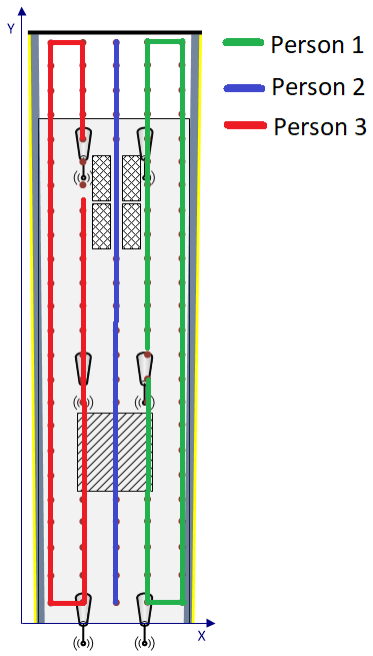

Figure 4.5: Grids and paths during the experiments for fingerprint map.

This process enabled us to record enough data samples to extract the fingerprint map of the platform.

When we collected the data provided by Sydney Trains (according to the defined rules and recorded timestamps) we extracted the averaged RSSI values for each point aiming to build the fingerprint map. Fig. 4.7 shows the averaged values of measured RSSI for each person from all the six APs. As mentioned, each person follows a specific defined rules during this stage. So, the measurement can be verified based on the patterns of change and its values according to its distance from each AP. Then, considering AP positions and defined paths for each participant, the fingerprint map formed using the average values of measurements to build the fingerprint map for each AP through the platform.

Having new measurements, the probability map for each node is calculated regarding each AP as illustrated in Fig. 4.6. The probability map is created based on the probability of being in different cells according to the fingerprint map. Considering the fact that measurements from each AP is independent from each other, all the probability maps are combined and

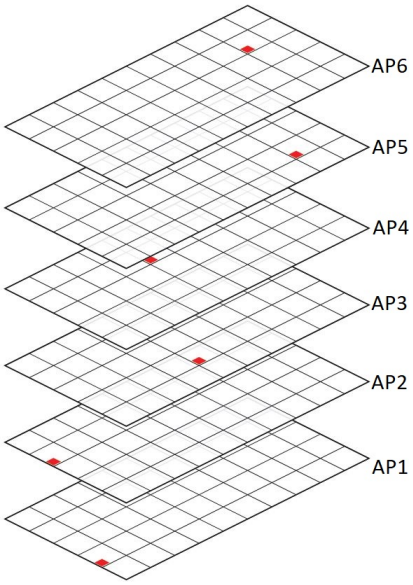

Figure 4.6: Positions of APs and the probablity stack to build probability map.

the expected number of people for each grid as described in (4.10). Finally, the density map is calculated according to the estimated numbers for each cell.

4.4.2 Density map extraction

CCTV images and WiFi probing data were collected for a week from the platform. The CCTV images are used as ground truth to extract the penetration rate (ρ) by counting the number of people within one minute window and matching it with the number of detected MAC addresses. Comparing both data, the penetration rate is calculated as one device per four person on the average ($\rho = 4$).

To extract the density map, the probability map for every detected node is calculated regarding each AP and the final probability map is created for each node. Then, all the probability values formed the final density map for one minute set of measured data. Finally, using KNN (K-Nearest Neighbors) method the final heat map is generated for every minute. Fig. 4.8 shows samples results for the crowd distribution and density map on the platform at

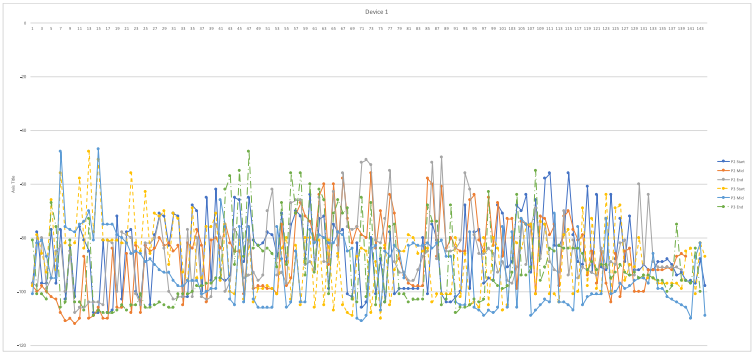

(a)

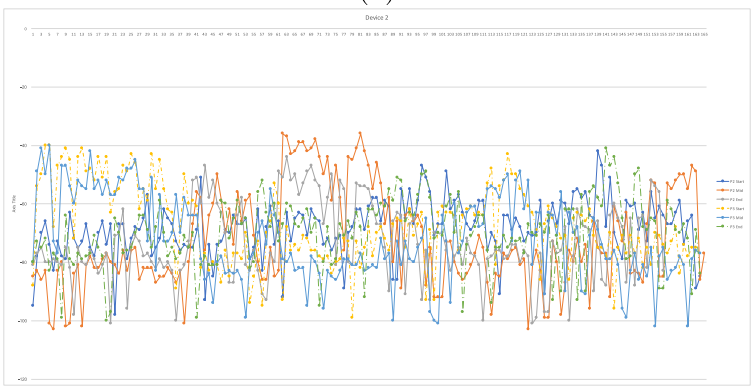

(b)

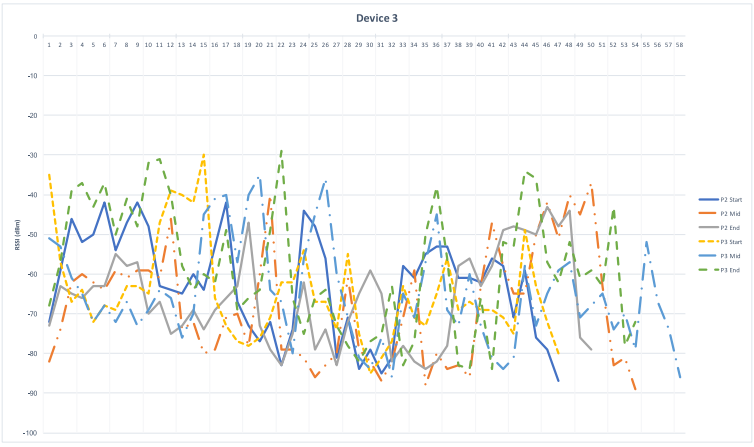

(c)

Figure 4.7: Averaged RSSI measurements for three different person in all the six APs. (a) First person. (b) Second person. (c) Third person.

four different time stamps on 27 June 2017. According to the definition provided by Sydney trains, more than five persons in a square meter considered dangerously crowded. So, the density heat map reflects these values by assigning blue to zero (no one in a cell) and red to having six people in a cell.

Fig. 4.8(a), (b) and (c) shows three continuous intervals at 16:01, 16:02 and 16:03, respectively. The changes of the crowd distribution in the platform before, during and after train arrival can be seen. In Fig. 4.8(c) and (d) nearly uniform distribution of the crowd density also can be noted near the concourse. Another interesting point that can be seen in Fig. 4.8 is the fixed high density cells on the sides of the platform which are indicators of train doors.

The analysis results are compared with the results of analysis of CCTV images. Using deep learning method, the machine is trained to identify people and extract the density based on the number of people within a square meter. Fig. 4.9 shows the crowd density analysis using CCTV images at 16:02, 16:03 and 16:31. Comparing Fig. 4.9(a) and (b) with Fig. 4.8(b) and (c) that show the results for 16:02 and 16:03, respectively, proves that both are following similar patterns in terms of density distribution. Fig. 4.9(c) represents the distribution for 16:31 to compare with Fig. 4.8(d), as well. Although the results are acceptable, considering the resolution of data in both approaches but there is a chance for discrepancy due to the missing data. WiFi detection is highly depended on the number of available devices and the quality of images and camera placement plays an important role in counting people and estimating their locations.

4.5 Conclusion

In this chapter, an experimental evaluation of WiFi crowd estimation and a new approach in estimating its distribution over the platform 2/3 in Redfern train station, Sydney is pre-

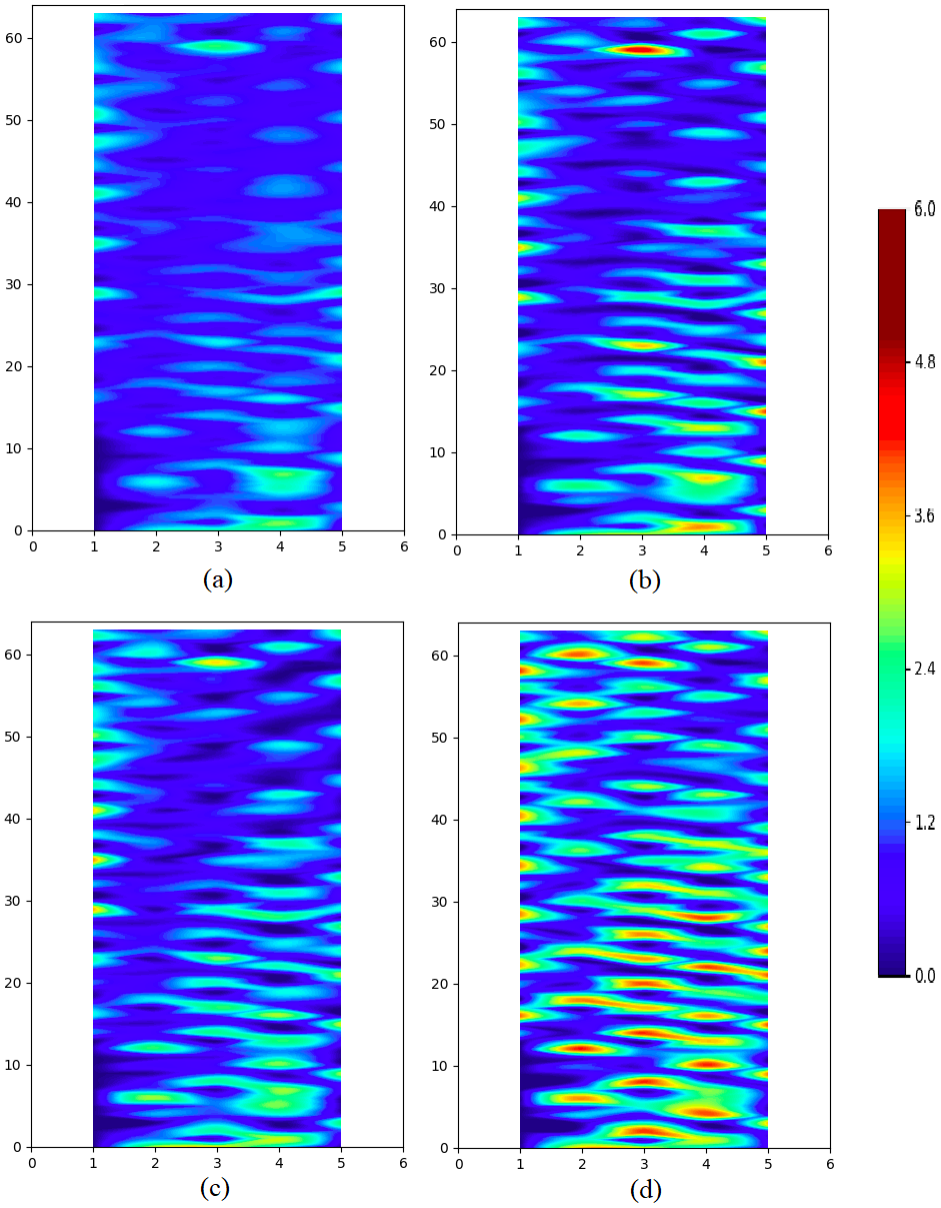

Figure 4.8: Crowd distribution on the platform 2/3 of Redfern station. (a) 27 June 2017 at 16:02 (b) 27 June 2017 at 16:03 (c) 27 June 2017 at 16:31 (d) 27 June 2017 at 17:00

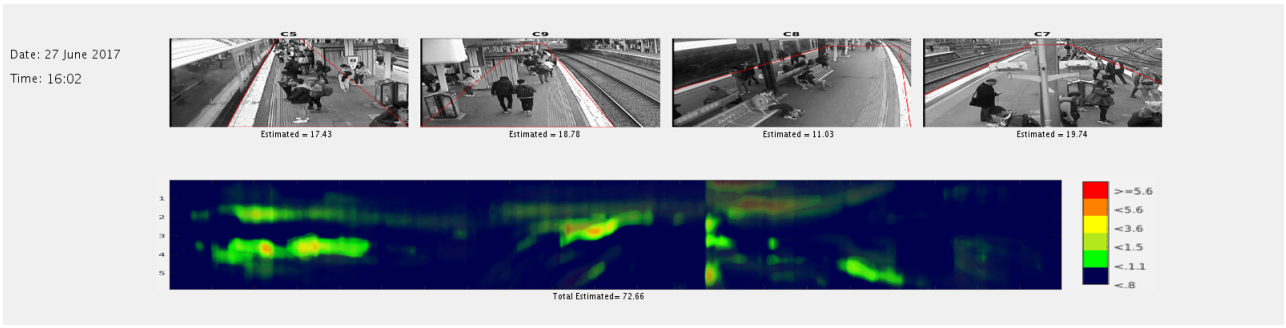

(a)

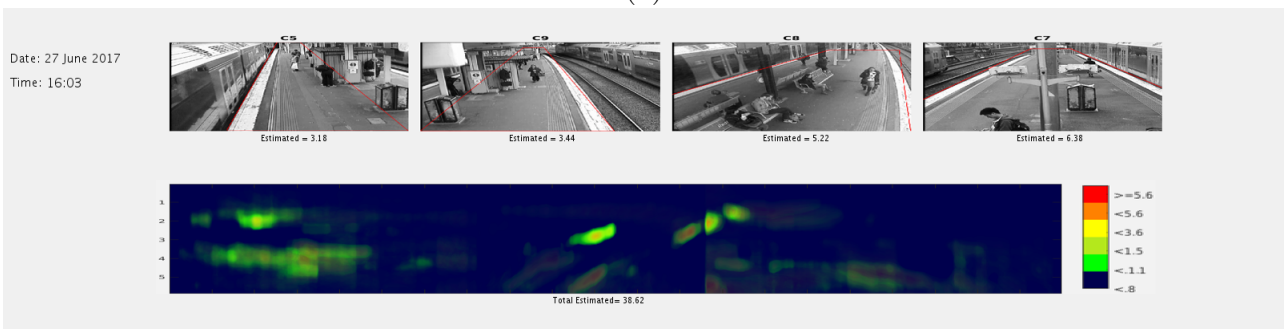

(b)

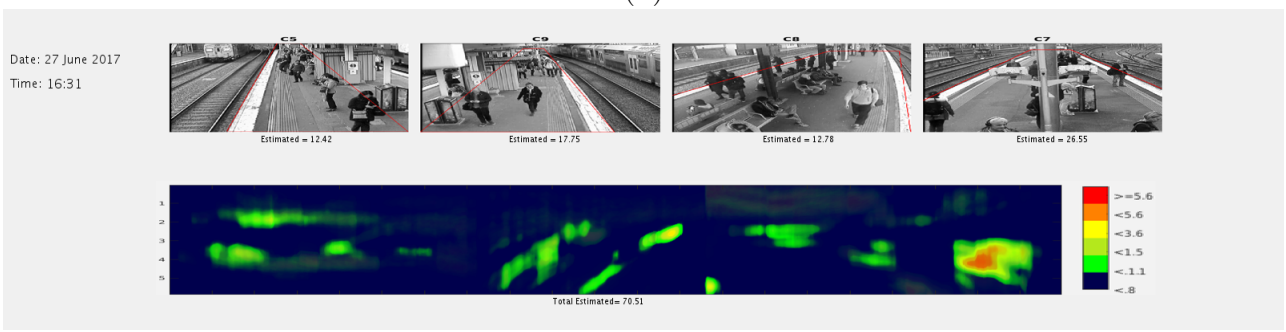

(c)

Figure 4.9: Crowd distribution based on CCTV images. (a) 27 June 2017 at 16:02 (b) 27 June 2017 at 16:03 (c) 27 June 2017 at 16:31

sented. A probability map based on RSSI measurements and prior knowledge is constructed which is used to determine the location of new nodes and measurements. Final results are compared to the density maps extracted from CCTV images during same period and proves a good accuracy. However, it is noteworthy to mention that both methods have there own shortages. Image based techniques rely on having high quality images and camera deployment in proper angle of view. For example, during the experiments, we experienced a direct sun light turning aquired images unreadable. WiFi measurement accuracy is also limited due to miss detection and security measures such as dynamic MAC addresses. Thus, a combination of both techniques can cover all possible shortcomings and help to provide more accurate density maps.

Chapter 5

Crowd Estimation Using Electromagnetic Wave Power-Level Measurements

Current crowd density estimation technologies that leverage IR depth perception, video and image processing or WiFi/BLE-based sniffing and probing have privacy and deployment issues. This chapter presents a novel method for crowd density estimation that monitors variation in Electromagnetic (EM) radiation within an environment using a combination of advanced metamaterials and analytics to create a crowd density estimation detector.

5.1 Introduction

The rapid growth in urban populations demands new methods for managing crowds. However, crowd density estimation has proven to be very challenging due to various issues, such as privacy and infrastructure availability. Various techniques have been introduced and investigated recently, which can be categorized as "device-based" and "device-free" techniques.

The image-based and signal-based strategies explored in the previous chapters have the inherit problem of privacy. In image processing and IR-based approaches, captured images can be associated with individuals to identify and track them. Likewise, wireless probing techniques suffer from potential privacy issues with the current WiFi and BLE implementations that allow for a unique fingerprint of a device —and hence the owner of the device— to be created.

Recent advancements in the underlying technologies required to detect and measure the existence of dominant EM waves provide a means of developing a unique form of crowd density estimation in any environment that can address the privacy and deployment issues described above. When measuring the EM energy in an environment, any object introduced into the measured environment directly affects the amount of EM energy observed within the environment. The human body is on average 60% water, which has an effect on the amount of EM radiation within the environment. Measuring the effects of humans on the current environment and comparing them with the expected models of behaviour enables an estimate of the number of individuals to be determined. Importantly, the proposed method is privacy-friendly, as no unique identifier is obtained. Furthermore, this strategy does not require line-of-sight detection and can be placed in subtle locations.

5.2 Theoretical background

With the advent of new wireless technologies, our world is filled with EM waves, and any object has an effect on the level of measurable EM energy at each frequency. The human body is a complex organism with plenty of oxygen, carbon, and hydrogen [86]. These elements, in combination with many other elements, such as calcium, sodium, magnesium, and phosphorus, build a system with many different types of characteristics and properties. Thus, this lossy dielectric, the human body, absorbs part of energy while transmitting it.

This section describes the units of absorption and models to be used in the study.

5.2.1 Units of absorption: SAR and ACS

To measure the absorption, the measurement units should be defined first. One of the main quantities to consider is the specific absorption rate (SAR). The SAR, defined in Eq. (5.1), quantifies the amount of electromagnetic power that is absorbed per unit mass.

$$SAR = \frac{P_{abs}}{m} \tag{5.1}$$

P_{abs} and m represent the absorbed power and body mass, respectively.

There is an alternative quantity that represents the amount of absorbed power by the whole body and is known as the absorption cross-section (ACS) [87]. Eq. (5.2) defines the ACS (σ_a) according to the absorbed power, P_{abs}, and power density, S_c.

$$\sigma_a = \frac{P_{abs}\,(W)}{S_c\left(\frac{W}{m^2}\right)} \tag{5.2}$$

Combining Eq. (5.1) and (5.2), the ACS can be calculated using the SAR as follows:

$$\sigma_a = \frac{SAR \times m}{S_c} \tag{5.3}$$

5.2.2 Absorption by tissues: dielectric relaxation and the response of dielectrics to time-varying fields

The absorption of electromagnetic energy in the human body is a complicated problem due to the multiple layers of tissues. Thus, the human body can be modelled as a lossy dielectric with a complex permittivity. Applying an electric field to a dielectric, the material takes a limited amount of time to polarize [88]. Consequently, this lag will cause phase differences

between the field and polarization, which result in loss and attenuation of a wave traveling through it.

This property of the dielectric can be described as the penetration depth. The penetration depth, δ, is the depth that the amplitude of the wave is decreased to $\frac{1}{e}$ of its initial amplitude. In a good conductor, the penetration depth is defined as follows [89]:

$$\delta = \sqrt{\frac{2}{\omega\sigma\mu}} \tag{5.4}$$

where $\omega = 2\pi f$, σ is the conductivity and μ stands for the permeability. The dependence of the penetration depth on the frequency determines one of the important parameters in our study. For example, the penetration depths for dry skin, infiltrated fat, and muscle as a function of frequency were calculated in [90]. For dry skin, fat and muscle, the penetration depth was calculated to be 2.5 m, 1.3 m and 0.8 m at 1 MHz and 1.4 mm, 3.9 mm and 1.3 mm at 20 GHz.

5.2.3 Absorption by the whole body

The specific absorption ratio is calculated using full-wave simulations with complex voxel models. Many such models of the human body have been developed for medical, biomedical and radiation investigation purposes [91–96]. In this research, we have used the family voxel model for simulation and SAR calculations.

Although various factors should be taken into account in estimating human body effects on the level of available EM energy, considering the proposed application, we have simplified it by only considering the absorption as a function of height and mass. These two parameters can be indicators of the few other related parameters, such as body surface area, an estimation of body fat and body water. Thus, using these two parameters can provide a

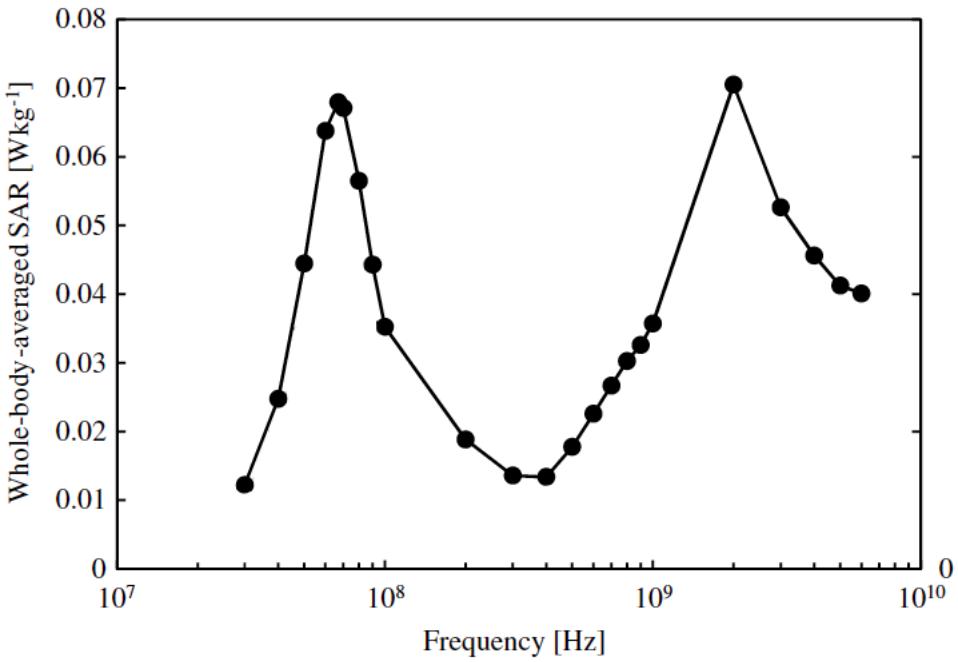

Figure 5.1: Whole-body-averaged SAR of a Japanese male model [97].

proper estimation of the average absorbed power.

5.3 System evaluation

To evaluate the theory, a series of simulations and experiments have been designed and performed. As mentioned above, frequency is one of the main parameters in body absorption measurements. Hirata *et al.* studied SAR relation with body temperature elevation from 30 MHz to 6 GHz using seven different human body models [97]. Fig. 5.1 represents the calculated values for whole- body-averaged SAR in a Japanese male model, showing two peaks at 60 MHz and 2 GHz. Thus, measurements around these frequencies will provide better accuracy in the our estimation. However, there are other factors that need to be considered during the tests. These factors will be illustrated in the next section.

A simulation is performed using FDTD numerical solutions in Comsol to investigate the proposed estimation approach in a 3D environment. A room with metal walls and dimensions

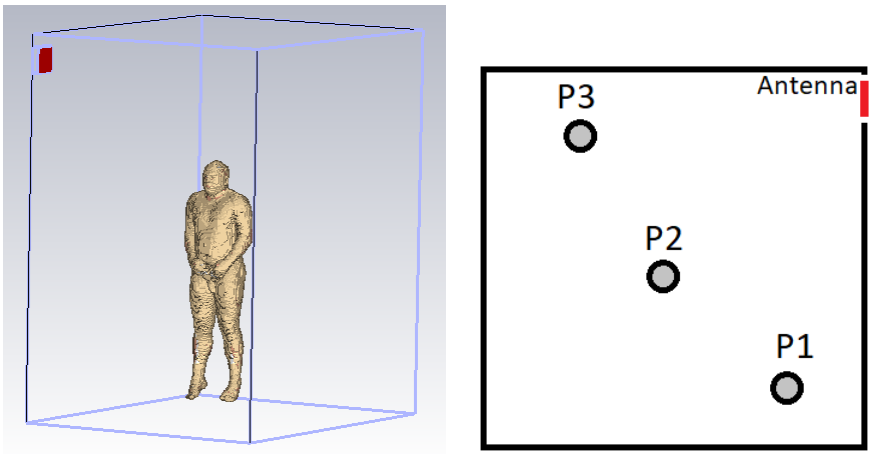

(a) (b)

Figure 5.2: (a) Simulation environment with the male model. (b) Positions of the model during the simulation.

of $4 \times 4 \times 4\ m^3$ is chosen as the simulation environment, which helps to control the available power inside a Faraday cage and results in accurate measurements. Moreover, a voxel family model is used during simulations to simulate body effects on the signal. Fig. 5.2 shows the simulation environment with the male model and its positions during the simulations.

Frequencies with maximum absorption values are chosen in the presence of the human body model to simulate the effects of the human body. To obtain an understanding of the EM wave energy distribution, the E-field distribution at 60 MHz and 2 GHz in the proposed room is simulated, and the results are shown in Fig. 5.3. At 2 GHz, the wavelength is $14.99cm$, which is small compared to the room dimensions. This resulted in a significant amount of peaks and holes and consequently a complicated field distribution. However, at 60 MHz, the wavelength is $\sim 5m$, providing a more uniform and stable distribution of the field inside the room. Moreover, at 2 GHz, the wavelength is comparable with body dimensions, and thus, any small body movement results in field distribution disruption and makes the measurements more challenging.

Noting the field distributions, the receiver antenna placement is also an important factor in available power measurements, specifically in a metallic room. The electromagnetic waves

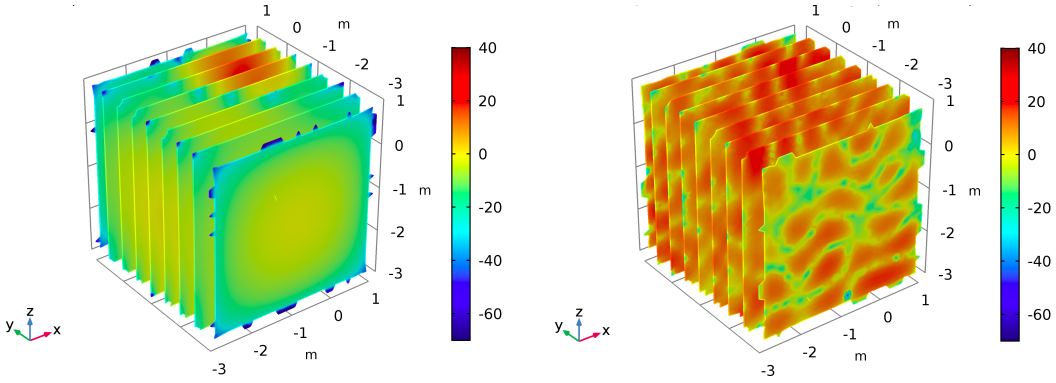

Figure 5.3: E-field distribution in the room at (a) 60 MHz, and (b) 2 GHz.

produce peaks and holes due to the reflection in the environment, which can occur due to the introduction of various types of objects (including human body). Thus, in order to measure the absorption and changes in the level of RF energy, there is a need to have multiple antennas to measure the average energy level.

5.3.1 Simulation results

A series of simulations have been conducted based on numerical solutions using Comsol as follows:

- People's positions and their effects on the field distribution: one person in the room in various positions at 60 MHz and 2 GHz.
- Effects of the number of people on the E-field distribution and value.
- Effect of different human bodies: males, females, and children.

5.3.1.1 Effect of various positions on the field distribution

In the first step, a male body is inside the room in the positions illustrated in Fig. 5.2, simulated at 60 MHz and 2 GHz. The simulated E-field distribution for both resonance

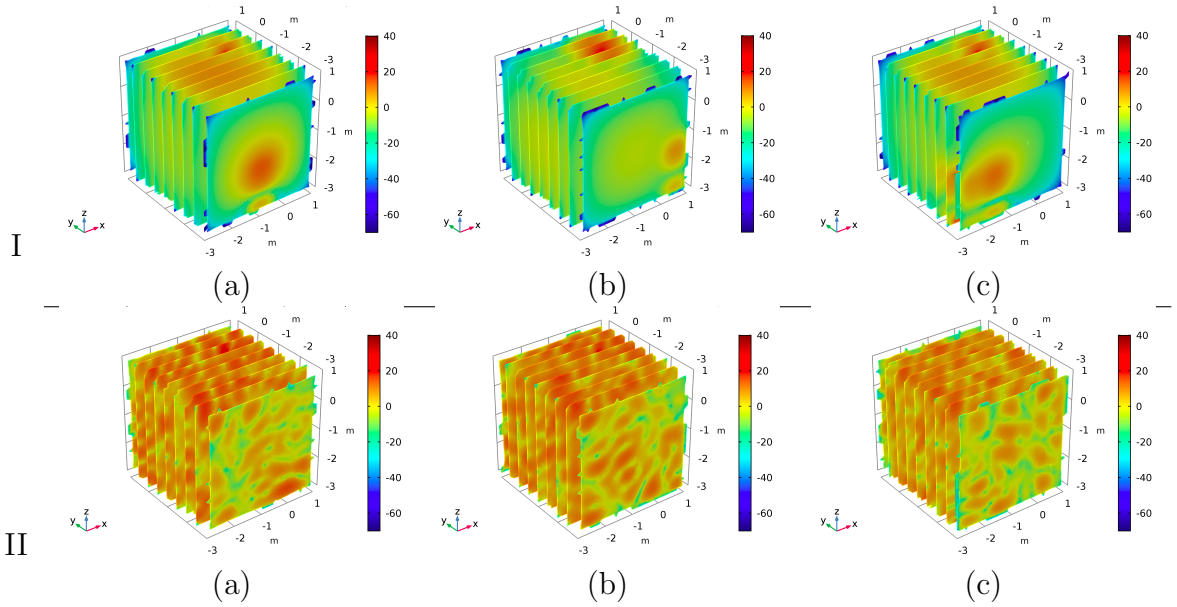

Figure 5.4: E-field distribution at two resonance frequencies, 60 MHz (section I) and 2 GHz (section II), with one person at three different positions. (a) Position 1. (b) Position 2. (c) Position 3.

frequencies is shown in Fig. 5.4. At both frequencies, a male model is placed in positions I, II and III in the series of (a), (b), and (c) in Fig. 5.4, respectively. The differences between distributions can be clearly seen in different positions at both frequencies. At 2 GHz, the E-field distribution changes significantly with position changes due to the small wavelength. However, at 60 MHz (row I), the E-field and, consequently, Radio Frequency (RF) energy are distributed nearly uniformly and are more robust to position changes, making the measurements more reliable. It is noteworthy that in order to have a proper measurements and estimation, the average changes in the available RF energy level are required. Thus, one receiver antenna cannot be used in the measurements since it only measures the receiving signal levels. Therefore, choosing 60 MHz as the main test frequency, multiple antennas should be deployed in various planes to provide proper measurements during simulations and experiments.

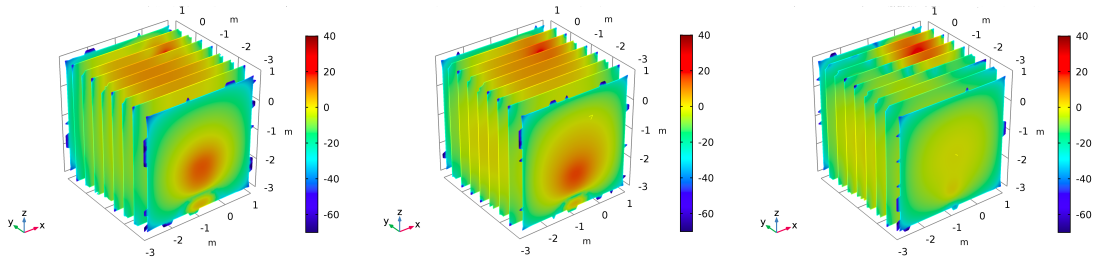

(a) (b) (c)

Figure 5.5: Body type effects. (a) Male. (b) Female. (c) Child.

5.3.1.2 Effect of body type and size on the field distribution and its values

As mentioned above, the human body is a very complex medium, especially considering different genders and ages. Thus, body type and size are important factors in estimating crowd density using RF energy measurements. To model these effects properly, we have considered three main body types, male, female and child, in the simulations. Fig. 5.5 represents the results of simulations for the three body types. The resulting field distribution demonstrates the need for having multiple antennas during the measurements. Using the probe, the energy levels in the planes are measured for each simulation.

5.3.1.3 E-Field distribution and its average value in the presence of different numbers of people

The ultimate goal of the proposed approach is to estimate the number of people and possible detection of the body type. To this end, a series of simulations with different numbers of people and various body types are considered, and the average RF energy levels are measured. Table 5.1 shows the average values for various scenarios. The averaged available RF energy in the room, AKA the reference energy, is normalized to zero dBm. For an average male body, the average energy drops to -0.65 dBm. For an average female body, the RF energy level is similar to the that of the male body, -0.65 dBm.

Number of people		Average RF energy (dBm)
0	0	0
1	Male	-0.65
1	Female	-0.65
1	Child	-0.4
2	1 Male + 1 Female	-1.1
2	1 Male + 1 Child	-0.8

Table 5.1: Simulation results for different numbers of bodies with various body types.

5.3.2 Experimental evaluation

The proposed approach is backed up by designing a series of experiments inside an elevator cabin. The elevator cabin is chosen due to its metallic case, which works as a Faraday cage and provides a controlled environment. As mentioned above, a frequency of 60 MHz is selected for the test. The wavelength in this frequency is comparable to the dimensions of the elevator cabin and human body, and thus, the recorded energy levels are more stable during position changes. In the experimental setup, a transmitting antenna along with a software defined radio unit (HackRF One) is used to provide a steady level of RF energy. Other HackRF One units and a Rohde & Schwarz FSH8 (R&S) handheld spectrum analyser is used to measure the signal levels inside the room.

Fig. 5.6 shows the experimental setup. During each experiment, ten measurements were collected with defined positions for antennas and subjects (i.e., the people being measured). Then, the position of subjects were changed, and the measurements were repeated.

Four people with different body types—three males, a female —took part in the measurement tests.

Table 5.2 presents the average level of measured RF energy per person. Inside an empty room, an average value of -19 dBm was measured initially. The measurement results for different scenarios follow the trend of the simulations reported in Table 5.1, proving that the proposed approach could be used to estimate crowd density.

Figure 5.6: Experiment setup.

Number of people		Average RF energy (dBm)
0	0	-19
1	Male	-20.2
1	Female	-20.3
2	Male	-21.2
2	Female	-21.2
2	1 Male + 1 Female	-22.4
3	2 Male + 1 Female	-24
3	3 Male + 1 Female	-25.3

Table 5.2: Average level of measured RF energy per person.

5.4 Conclusion

In this chapter, a new method for crowd estimation using EM measurement levels has been presented. The proposed approach is investigated through simulation and experiments. The experimental results confirm an approximately $0.8dB$ drop in the average signal level.

As mentioned above, the average level of RF energy should be measured to provide accurate measurements and estimation of the crowd. In this chapter, multiple antennas are used during the measurements. However, using multiple antennas and averaging the measured values can be costly and not accurate. Therefore, having a device that can provide the average energy level with a lower cost would be worthwhile. To this end, we leverage metamaterial properties and design a metamaterial perfect absorber to measure the average value of the available RF energy.

Chapter 6

Low-Frequency Metamaterial Absorber Using Space-filling Curves

In the previous chapter, a method of crowd estimation based on changes in electromagnetic energy levels was introduced. The accuracy of the estimation is directly related to the accuracy of the energy-level measurements. Furthermore, using antennas for the measurements can only measure the signal levels at one point. Thus, understanding the changes in the energy levels requires a large number of measurements and averaging the measured energy levels.

Metamaterials, due to their unique characteristics, are used in various applications, such as invisibility cloaks [98–101], super lenses [102, 103], and sensing devices [104–106]. Among various types of metamaterials, absorbers are good candidates to be used as energy measurement sensors. The key point of using metamaterial absorbers for measuring the EM energy level is that they can be fabricated to provide a large surface, and an accurate measurement of the average available power can be obtained. Metamaterial absorbers can absorb 100% of the electromagnetic energy which enables detection of slight changes in the level of electromagnetic energy.

This chapter provides an overview of the physics behind metamaterials and metamaterial absorbers. It also provides a short description of various techniques introduced in the previous designs. Furthermore, a design of a compact absorber using space-filling curves is introduced as a solution of providing low frequency absorbers.

6.1 Introduction to metamaterials

In 1999, Rodger M. Walser from the University of Texas Austin introduced the term "metamaterial" to describe "Macroscopic composites having a synthetic, three-dimensional, periodic cellular architecture designed to produce an optimized combination, not available in nature, of two or more responses to specific excitation" [107, 108]. However, recent research has proven that metamaterial structures are not restricted to periodic cellular architectures, and non-periodic structures also can offer metamaterial properties. Fig. 6.1 illustrates some of the initially introduced metamaterial designs [109, 110].

Metamaterials with a sub-wavelength unit cell size can be described using the effective medium theory [111]. Thus, a material can be characterized by its electric permittivity (ε) and magnetic permeability (μ). Considering the thinnest material in nature, free space with permittivity of ε_0 and permeability of μ_0, the characteristics of a material can be described using its relative permittivity and permeability, defined as $\varepsilon_r = \frac{\varepsilon}{\varepsilon_0}$and $\mu_r = \frac{\mu}{\mu_0}$, respectively.

For a long time, metamaterials, Left-Handed Materials (LHM), Negative-refractive Index Materials (NIM), Double-Negative Materials (DNG), and backward-wave materials have been used interchangeably. However, they represent different meanings in practice. At present, metamaterials can be interpreted as a large umbrella that covers all the materials that cannot be found naturally, and each point in the $\varepsilon - \mu$ domain represents specific properties. For example, the point $\varepsilon = -\varepsilon_0$ and $\mu = -\mu_0$ indicates anti-air in the LHM region that can produce a perfect lens. Materials with $\mu = 0$ and $\varepsilon = 0$ are also called μ-Near Zero

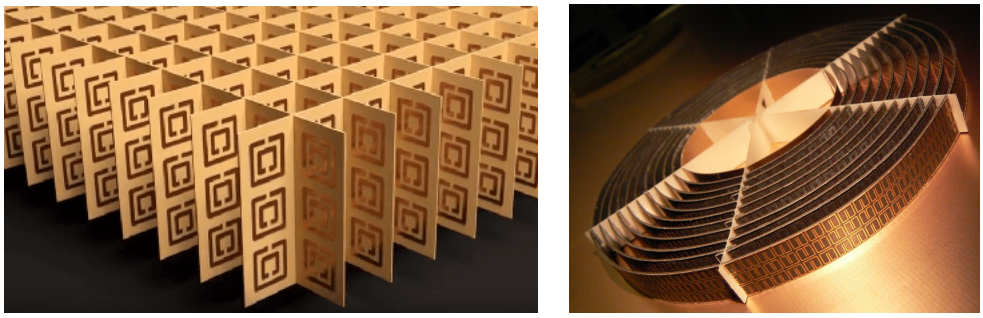

(a) (b)

Figure 6.1: Periodic and non-periodic metamaterials. (a) Periodic structures [109]. (b) Non-periodic structures [110].

(MNZ) and ε-Near Zero (ENZ) materials, respectively. The line $\varepsilon = \mu$ in both the Right-Handed Materials (RHM) and Left-Handed Materials (LHM) regions defines the impedance-matching materials, resulting in no reflection, known as absorbers. Metamaterial absorbers have been proposed in a wide range of applications such as the absorption of undesired frequency [112], solar cells [113], thermal emitters [114] and optical switches [115, 116].

Natural materials usually have permeability μ_0 and permittivity greater than ε_0. Metamaterials take a step further by enabling designers to realize all possible material properties. Fig. 6.2 represents the possible properties for isotropic and lossless materials in the domain of permittivity and permeability. The first quadrant, in which the permittivity and permeability are greater than zero, corresponds to Right-Handed Materials. Right-handed materials support forward-propagation waves and can be described with Maxwell's equations, electric field (E), magnetic field (H) and wave vector (k). The second ($\varepsilon < 0 \; and \; \mu > 0$) and fourth ($\varepsilon > 0 \; and \; \mu < 0$) quadrants represent electric and magnetic plasma environments, respectively, and both support evanescent waves. Left-handed materials (LHM), introduced by Veselago [117], are shown in the third quadrant, where $\varepsilon < 0$ and $\mu < 0$.

Most natural materials have a magnetic permeability of $\mu = \mu_0$ and electric permittivity of $\varepsilon \geq \varepsilon_0$. This feature is shown as a line in the first quadrant of Fig. 6.2. Furthermore, natural electric and magnetic plasma can be rarely found, characterized in the second and

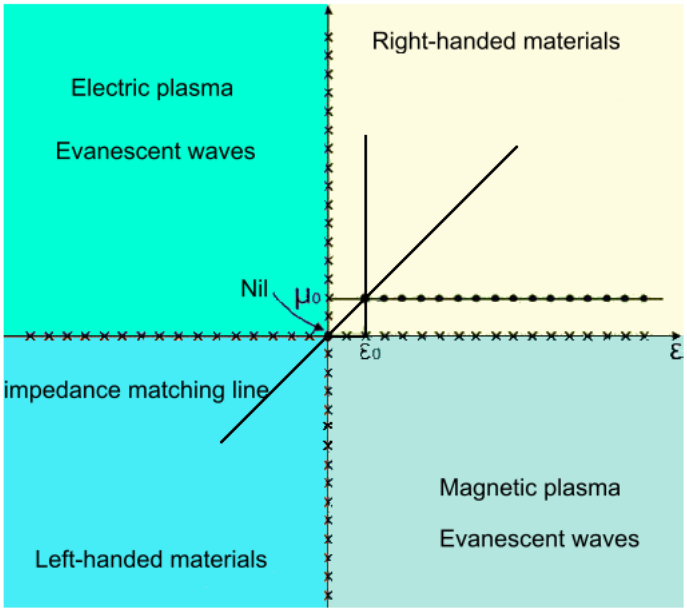

Figure 6.2: All possible properties of materials [108].

fourth quadrant of the Fig. 6.2. Meeting any other characteristics for permittivity and permeability requires an accurate realization using metamaterials, even for RHM.

6.2 Left-Handed materials

Effective medium theory suggest that the description of electromagnetic properties of any given material can be done by its electric permittivity (ε) and magnetic permeability (μ). These properties are used to describe and predict electromagnetic phenomena within a material or at the surface between two materials such as refractive index. Snell's law states the relations between the angles for incident and refracted or transmitted waves, which is mainly known as the refractive index and defined as $n = -\sqrt{\varepsilon\mu}$. Veselago, in 1967, analytically determined the reverse refraction of light at the interface of a material with negative refractive index and conventional refractive index, as shown in Fig. 6.3(a). This extraordinary material was realized in theory by Veselago but ignored for decades. In 2000, David R. Smith introduced a class of materials by depositing a structure onto a circuit-board substrate

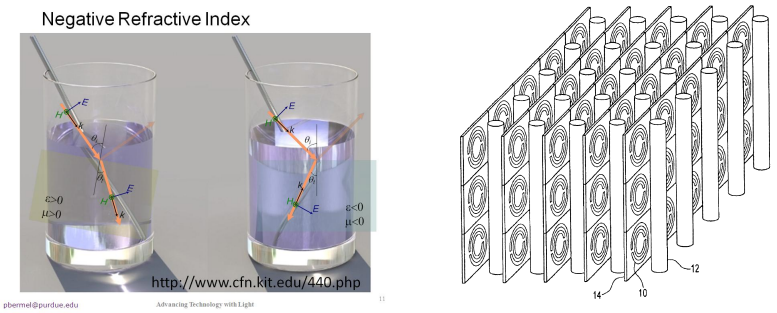

(a) (b)

Figure 6.3: (a) Refraction in LHM. (b) The negative-refractive-index material introduced by Smith *et al.* [118].

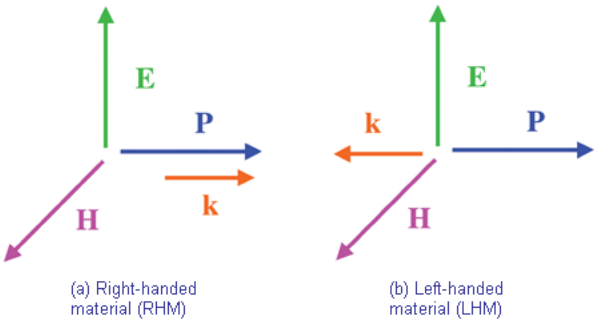

Figure 6.4: Right-handed and left-handed coordinates and EM fields.

consisting of a series of thin copper split-rings and ordinary wire segments strung parallel to the rings [118]. Fig. 6.3(b) represents the structure introduced by Smith *et al.*

The interesting phenomena of negative refractive index introduced a new direction for research and applications in the field of microwave theory. Considering the negative permittivity and permeability in the material, Maxwell rules should be adjusted since the combination of electric field (E), magnetic field (H), and phase vector (k) does not follow the right-handed coordination system anymore. Thus, having a wave in a material with negative refractive index, it propagates in the reverse direction. This feature that is illustrated in Fig. 6.4 enables sub-wavelength imaging by making resolution below the diffraction limit possible.

The reverse-propagation feature of metamaterials also offers a flat surface, in contrast

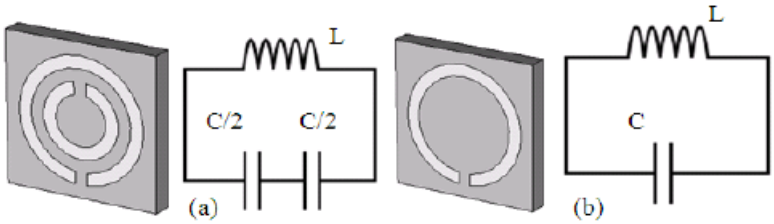

Figure 6.5: Conventional SRR. [119]

with conventional materials, which are usually curved. This flat structure can be achieved by implementing an LC resonator as a cell. In the resonance frequency, the system represents an abrupt change in the imaginary value of the impedance, which is interpreted as the metamaterial properties. Split-ring resonators (SRRs) are one of the early designs that provide the LC resonators [119]. Fig. 6.5 shows two conventional SRRs and their equivalent circuits. The top metallic layer of the structure is responsible for the electric response of the system, whereas the anti-parallel current between top and bottom layers plays the role in its magnetic responses. Thus, understanding the structures such as conventional SRR and effective parameters of the design lead the designer to manipulate the unit cell to resonance at the desired frequency.

As mentioned above, metamaterials offer lots of applications due to their specific characteristics. The following section of this chapter provides an overview of the physics behind the design of metamaterial absorbers and discusses various techniques that have been introduced in designing these absorbers. Metamaterial absorbers were initially introduced to offer an alternative solution for ferrite absorbers, which are heavy and have a considerable effect on the other part of system. Recently, new applications for metamaterial absorbers have been introduced by researchers. Remarking the efficiency of metamaterial absorbers in scavenging waves, sensing is one of the applications that have drawn much attention recently.

6.3 Principles of metamaterial perfect absorbers

The realization of high-efficiency unity absorption using metamaterials was first illustrated by Landy *et al.* [120] by adjusting the real and imaginary parts of the permittivity $\varepsilon(\omega)$ and permeability $\mu(\omega)$ to perfectly match the impedance of free space. Thus, the incident electromagnetic wave can be absorbed perfectly and dissipated. Such features of a Metamaterial Perfect Absorber (MPA) motivated the researchers to use it in various applications in different areas, such as thermal emitters [114] and optical switches [115, 116].

The effective impedance of the MPA is a function of its electric permittivity, $\varepsilon(\omega)$, and the magnetic permeability, $\mu(\omega)$, where both are also functions of frequency, f, and the material properties. Anti-parallel surface currents between the metal layers that define the permeability are responsible for the magnetic part of resonance. The surface current on top layer of structure expresses the permittivity, which stands for the electrical part of resonance. Thus, according to the impedance-matching theory, the effective impedance of an MPA can be adjusted to match the impedance of free space . The effective impedance of an MPA can be calculated as follows [121]:

$$Z(\omega) = \sqrt{\frac{\mu(\omega)}{\varepsilon(\omega)}} = \sqrt{\frac{(1 + S_{11}(\omega))^2 - (S_{21}^2(\omega))}{(1 - S_{11}(\omega))^2 - (S_{21}^2(\omega))}}, \omega = 2\pi f \tag{6.1}$$

Then, to match it with free space, we should have $Z(\omega) = 1$.

6.3.1 Absorption ratio

Typically, the transmission and reflection ratio of any surface can be determined by applying the Fresnel equations or using measurement instruments. However, there is not any straightforward solution for measuring the absorptivity of a surface. Thus, a specific approach is introduced to calculate the absorption ratio based on transmission and reflection measurements. Eq. (6.2) represents the absorption ratio of an absorber, which has been derived

from Fresnel equations [122],

$$| A(\omega) | = 1 - | S_{11} |^2 - | S_{21} |^2 \tag{6.2}$$

where $| A(\omega) |$ stands for the absorption ratio and S_{11} and S_{21} are scattering parameters of reflection and transmission, respectively.

Absorbers are designed to catch all the possible electromagnetic waves. For this purpose, a continues ground plane is usually used to block any transmission. Therefore, the transmission is nearly zero ($| S_{21} | \rightarrow 0$), and consequently, the absorption ratio can be simplified as [122]

$$| A(\omega) | = 1 - | S_{11} |^2 \tag{6.3}$$

6.4 A brief history about absorbers

In 2008, Landy *et al.* introduced a two-layer PCB as the first metamaterial-based unity absorption structure [120]. As shown in Fig. 6.6, the structure consists of two metallic layers on both sides of the substrate. The top layer of the structure is an Electric Ring Resonator (ERR) with a cut wire on its bottom layer providing electric and magnetic responses. The magnetic response in the system is the result of coupling between the mid wire of the ERR and cut wire on the bottom layer. Landy's work introduced a new area of research with a wide range of applications targeting absorption of undesired frequencies [112] and sensing applications [123].

There has been much effort to customize MPAs for different applications. Different metamaterial applications have distinctive requirement based on their limitation. The size of the structure, frequency bandwidth, and ability to catch a signal with different polarizations and incident angles are some of the most important characteristics during the design procedure.

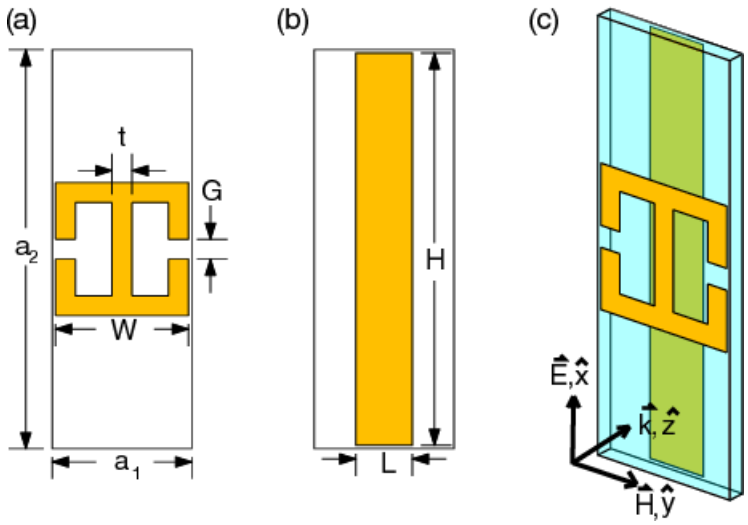

Figure 6.6: MPA structure proposed by Landy [120]

Furthermore, in some applications, such as energy harvesting, there are especial requirements such as wider bandwidth to maximize the absorption. Thus, changes in conventional structures are needed. Below, some of the presented solutions to eliminate specific requisites are reviewed.

6.4.1 Size of structure

One the main challenges in the design of MPAs, especially in lower frequency bands, is the size of the structure. The structure size of a metamaterial unit cell is directly relevant to the desired wavelength. To scale down the size of metamaterials, various methods have been proposed. These methods can be classified into three main categories. The first category is manipulating the shape of the structure and aims for longer effective electrical length within a compact structure. The second method is to use lumped elements in the designs to change the capacitance and inductance values of the system. The third technique is to use air gaps to increase the effective capacitance of the system.

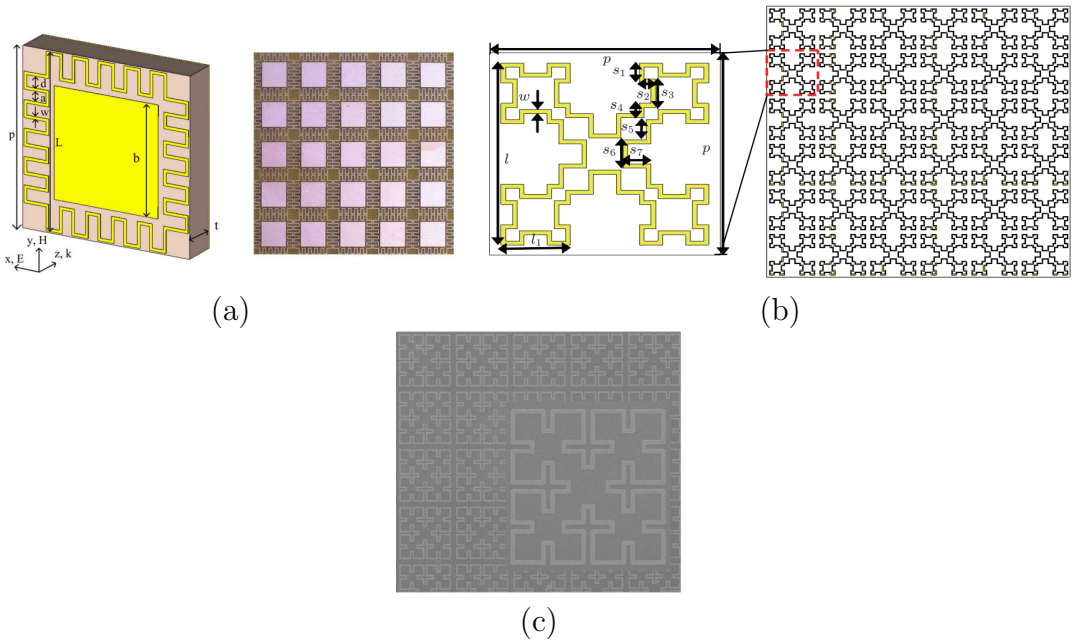

Figure 6.7: Unit cell size miniaturization via manipulating the effective electrical length of the structure [124–126].

6.4.1.1 Manipulating effective electrical length

Increasing the effective electrical length of the structure leads to the stimulation of lower frequencies in the system. In this regard, Yoo *et al.* presented a snake-shaped MPA, shown in Fig. 6.7(a), to decrease the size of the unit cell compared to the wavelength (75 cm) [124]. Recently, fractal-based structures have been used to decrease the size of the absorber's unit cell. For instance, Fan Y. *et al.* proposed a structure based on a Minkowski curve (Fig. 6.7(b)) to design an absorber that is small compared to the wavelength [125]. In another approach, Yanbing Ma at al. used Sierpinski fractals in a THz regime targeting to miniaturize the dual-band metamaterial absorber [126]. His proposed structure is shown in Fig. 6.7(c).

6.4.1.2 Systems with loaded lumped elements

Using lumped elements is another technique that has been used to to reduce the size of the metamaterial absorber unit cell. As discussed above, metamaterials are characterized based

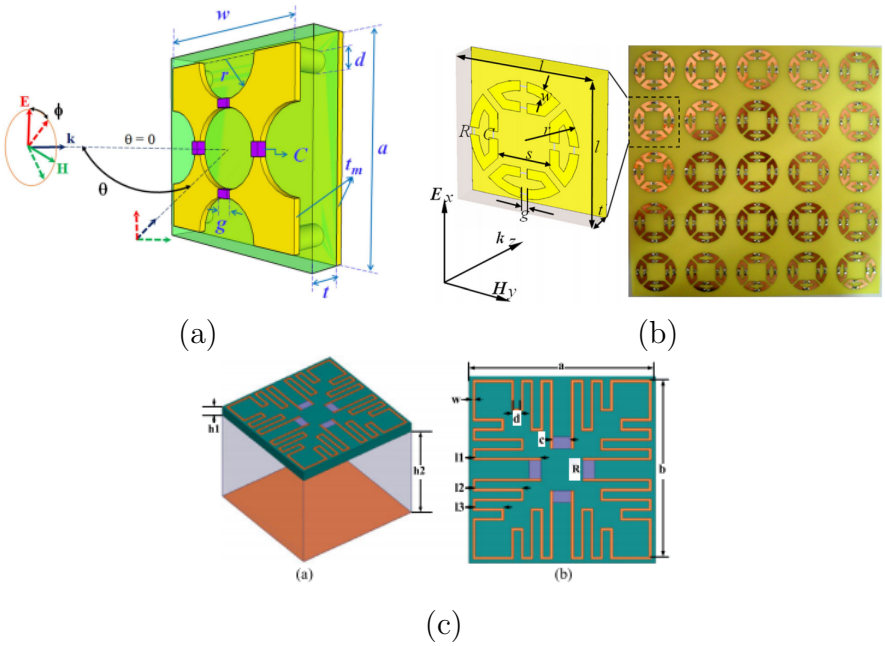

Figure 6.8: MPA miniaturization using lumped elements. (a) Lumped capacitors used in [127]. (b) Lumped resistors used in [128]. (c) Lumped elements use along with air gaps in [129].

on the capacitance and inductance values that the structure represents. Adding lumped elements and embedding them in the structure help to manipulate the values of the equivalent capacitance and inductance and thus shift the resonance frequencies. In this regard, Khunyen *et al.* in [127] used capacitors along with vertical inter-connectors to reduce the size of an MPA unit cell in a VHF band, as shown in Fig. 6.8(a). [128] added resistors into the structure, as shown in Fig. 6.8(b), and proved the use of lumped resistors in MPA to improve the absorption ratio and to increase the bandwidth.

6.4.1.3 Capacitance manipulation using air gaps

In another approach, researchers tried to manipulate the characteristics of the system by adding an air gap between the metallic layer and ground plane to increase the equivalent capacitivity of the MPA [130]. Using this technique, a smaller MPA unit cell reacts to the lower frequency bands, due to the added capacitor. In addition to miniaturization, air

gaps in a structure enhance the absorption ratio in higher-frequency bands according to the Fabry–Perot cavity concept [131]. However, to design the MPAs with desired frequency bands, researchers generally employ a combination of these techniques. For instance, in [132], the authors used a flexuous metal path with lumped resistors to miniaturize conventional absorber for RFID systems in a UHF band (910 MHz). In another study, the authors added a combination of lumped resistors and capacitors to achieve lower-frequency absorption bands [129]. Their design is shown in Fig. 6.8(c).

6.4.2 Multi-band metamaterial absorbers

Depending on desired applications, there is a demand for a system that can operate in multi-frequency bands. Having a multi-band system and controlling frequency bands is one of the challenging issues in the design of an MPA. SRRs (AKA ERR) with specific shapes and dimensions stimulate resonances in a specific frequencies in the system. This feature can also be used as a technique to achieve a wide band structure by putting the resonances close to each other. Therefore, by combining a number of these SRRs, a multi-band or wide-band system can be achieved. However, it is noteworthy that adding any number of metallic structures in the system affects the whole structure. The added part can introduce new capacitances between itself and other metallic parts of the structure (also known as the parasitic element for the other resonators), and thus, the final structure requires full analysis to understand the absorption bands.

In 2016, Gunduz *et al.* used three resonators to achieve three absorption bands, as represented in Fig. 6.9(a). In this design, every ring stimulates one frequency band, and due to the coplanar approach of structure, a thin structure is achieved. Thus, the absorber can be easily fabricated [133]. In another example, the authors proposed using a pair of rings to provide a quad-wide-band MPA, locating them alternatively in a homogeneous structure [134]. The proposed structure is shown in Fig. 6.9(b).

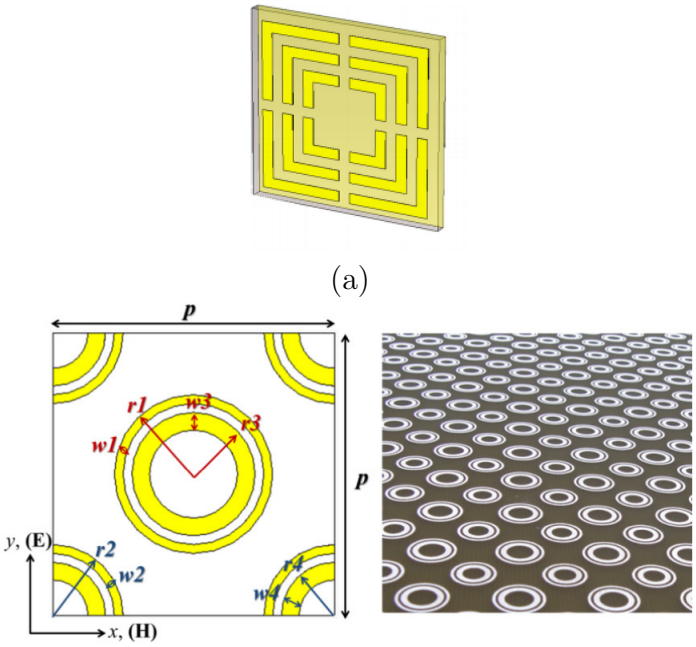

Figure 6.9: Multi-band SRRs. (a) Proposed structure in [133]. (b) Proposed structure in [134].

The other approach of having a multi-band MPA is to use vertical metal-dielectric layers as a multi-layer design. In this approach, each layer has resonances at specific frequencies. For instance, in [135], a four-layer structure that consists of defected squares with different sizes, as illustrated in Fig. 6.10(a), is proposed. In this structure, the close resonances of the system result in a broad absorption band. In another case, G. Dayal *et al.* proposed a different type of multi-layer structure MPA [136], which is shown in Fig. 6.10(b). In this technique, the substrate dielectric is shaped as micro-disk as illustrated in the circles in Fig. 6.10(b). Using this method, very high absorption over multiple frequency bands can be achieved.

As discussed above, MPAs have been designed to trap and dissipate incident signals. The calculation of the absorption ratio that has been presented in 6.3.1 shows its relation to the transmitted and reflected signals. The main effort in the designs is to design resonators

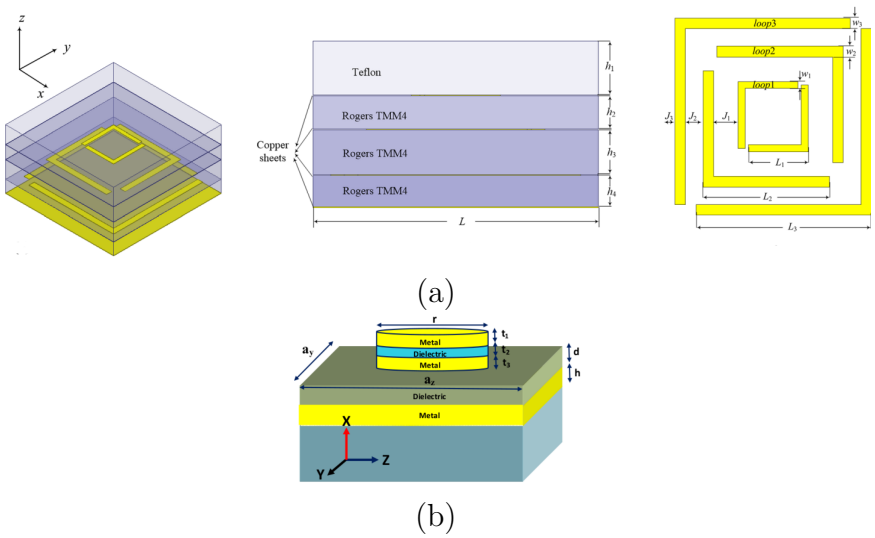

(a)

(b)

Figure 6.10: Multi-band MPA using a multi-layer technique. (a) [135] (b) [136].

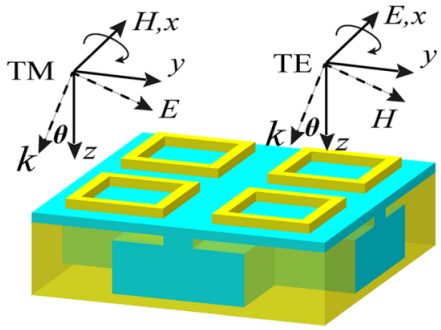

Figure 6.11: The cavity in the substrate using a folded ground plane [137].

that provide matching impedance and thus open the door for the incident wave. The signal is trapped and dissipated in the lossy substrate. Considering this concept, Zhang *et al.* introduced an approach to create a cavity inside the substrate [137]. In this approach, they used a combination of localized surface plasmon resonators and Helmholtz resonators, which are referred to as the surface square rings, and a folded metal plate is used, which is part of the ground plane, to form a cavity to trap the signal inside. Using this technique, the authors have achieved a dual-band wide-angle MPA with a nearly 100% absorption rate. Fig. 6.11 illustrates their proposed structure.

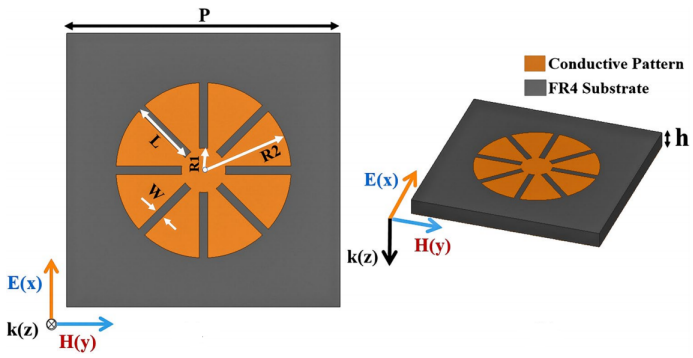

(a)

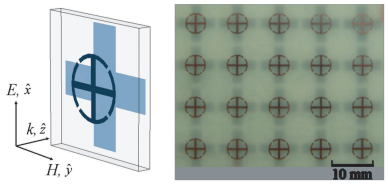

(b)

Figure 6.12: (a) Proposed structure in [138]. (b) Proposed structure in [139].

6.4.3 Insensitivity to polarization and oblique waves

Metamaterial absorbers are mostly designed to catch all the possible waves around. To this end, an absorber should be insensitive to the receiving wave angle and polarization. This feature is highly tied to the shape of the unit cell. To have a polarization-insensitive absorber, the proposed structure should be symmetric with respect to the cell's perpendicular vector. In [138], the authors presented a polarization-insensitive unit cell in the shape of eight-circular-sector conductive pattern, which is shown in Fig. 6.12(a). The symmetric structure also helps to improve the unit cell's response regarding a wide range of oblique wave angles. In some other works, such as [139], a combination of perpendicular and circular shapes has been used to catch signals with vertical, horizontal and circular polarization. As shown in Fig. 6.12(b), a four-sector cross is implemented in addition to the abovementioned combination, and thus, the whole structure stays symmetric. The proposed final structure is insensitive to the polarization and incidence angle.

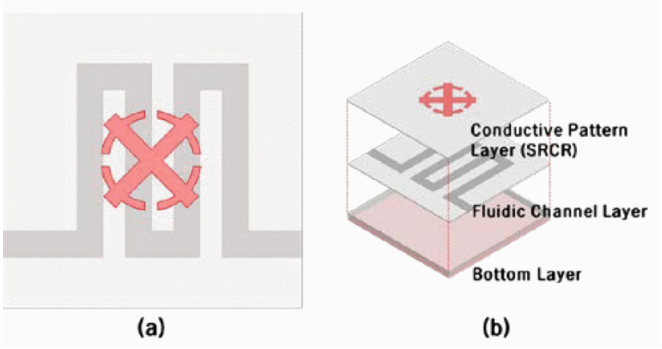

Figure 6.13: Metamaterial absorbers with sensing applications [143].

6.5 Metamaterials as sensors

With the advent of metamaterials and metamaterial absorbers, a new approach was introduced to enhance the sensing capabilities of various systems. For instance, in [123], Ishikawa used a plasmonic metamaterial absorber as a novel approach in infrared spectroscopic sensitivity measurements. A terahertz power meter using a thin-film metamaterial absorber was proposed by Park *et al.* [140]. To enhance Co2 gas sensing, a hybrid polymer-metamaterial absorber in the mid IR spectral was investigated in [141]. In [142], Ni *et al.* introduced a humidity sensor based on a metamaterial absorber on silicon. Kim *et al.* introduced an ethanol chemical sensor by combining micro-fluidic techniques with metamaterial absorbers, which uses variations in the resonance frequency (from 10.42 to 11.46 GHz) to determine the concentration of ethanol [143].

In chapter 5, we have introduced a new method of people detection and crowd estimation. According to the issues that have been discussed in the previous chapter, a metamaterial absorber can be introduced as a solution to enhance the accuracy of detection measurements. The following chapters of this thesis provide two different designs of metamaterial absorbers for the EM energy-level measurements. The first design is based on the space-filing curves (Sierpinski curve) as an approach for reducing the size of the unit cell to target very low frequencies. The next design provides a multi-layer metamaterial absorber design, target-

ing both 2.4 GHz and 5 GHz of WiFi bands, to enable accurate measurements for indoor environments.

6.6 A Polarization-Independent low-frequency metamaterial absorber using space-filling curves

The extensive use of metamaterials and metamaterial absorbers increases the demand for compact structures in various frequencies. Designing electrically small absorbers for lower frequencies, especially sub-gigahertz applications, is one of the open issues in this field.

Leveraging the characteristics of fractal structures, [144] utilized a Minkowski fractal to mitigate the multi-path phenomena in the UHF band. Combining this approach with other techniques, Liu *et al.* proposed a multi-layer structure loaded with lumped resistors to cover a wide range of frequencies from 5 GHz to 12 GHz [145]. Combining all these techniques, [128] used incurved square loops in combination with lumped elements and an air gap to target the UHF band. It is noteworthy that using fractal-based structures in MPA designs in addition to the miniaturization of the structure increases the number of absorption bands due to its repetitive pattern.

In this section, a new approach using space-filling curves is introduced to design an absorber operating on low frequencies. The logic behind the use of surface-filling curves is discussed while considering the equivalent circuit model of a unit cell in different steps. The unit cell design is based on the Sierpinski curve with the size of $25 \times 25 \times 1.6\, mm^3$ and air gap of $10\, mm$. The structure shows 99.9% absorption at 900 MHz on the third step. The system also exhibits multiple resonances due to its structure. The proposed structure is tested using a fabricated array of the third order of the curve, and the results are compared with the simulation outcomes.

6.6.1 Design of the unit cell

A space-filling curve is a curve that can cover the entire 2D unit square. The specific structures of these curves introduce loops with various sizes in different orders. Leveraging these features, a metamaterial structure can be manipulated to stimulate various resonances in the system. However, it should be noted that only a limited number of steps can be followed in the design due to the various restrictions, such as fabrication limitations. It is also noteworthy that in higher orders, the unit cell is almost fully covered and turns into a plane copper plate. In this chapter, the Sierpinski curve, as one of the well-known space-filling curves, is analysed to provide resonances in lower frequency bands with a fixed size of the unit cell for various sensing purposes.

Fig. 6.14(a) represents the base design of the first order of Sierpinski curve-based MPA. The width for the unit cell is fixed for all steps to W. The line width for the first step is $W_1 = 1mm$, and the length of the line is $L_1 = 3mm$. The first step of the curve, Fig. 6.14(a), can be modelled as shown in Fig. 6.15(a), providing two resonances at 14.4 GHz and 16.7 GHz, as shown in Fig. 6.16. In this circuit, C_{11} represents the capacitance between the lines, and L_{11} is the inductance created in the smaller loops of the curve. L_{12} stands for the inductance value of the whole cell. C_{sa} is the equivalent capacitor for the capacitance values for the substrate and air gap.

In the next step of the curve, Fig. 6.14(b), the width of the line is $W_2 = \frac{W_1}{2} = 0.5mm$, and its length is $L_2 = \frac{L_1}{2} = 1.5mm$. Although the width of the line is decreased, the added length and capacitances increase its value. Furthermore, new routes of the induced surface current increase the inductance values, denoted as L_{22} in Fig. 6.15(b), and result in stimulating the lower resonance frequencies of 1.2 GHz and 5.4 GHz. However, the impedance of the structure at 1.2 GHz is not fully matched with the air impedance. Using higher orders of the Sierpinski curve, impedance matching occurs in lower frequencies due to the added effective electrical length. In the third order of the curve, the line width and

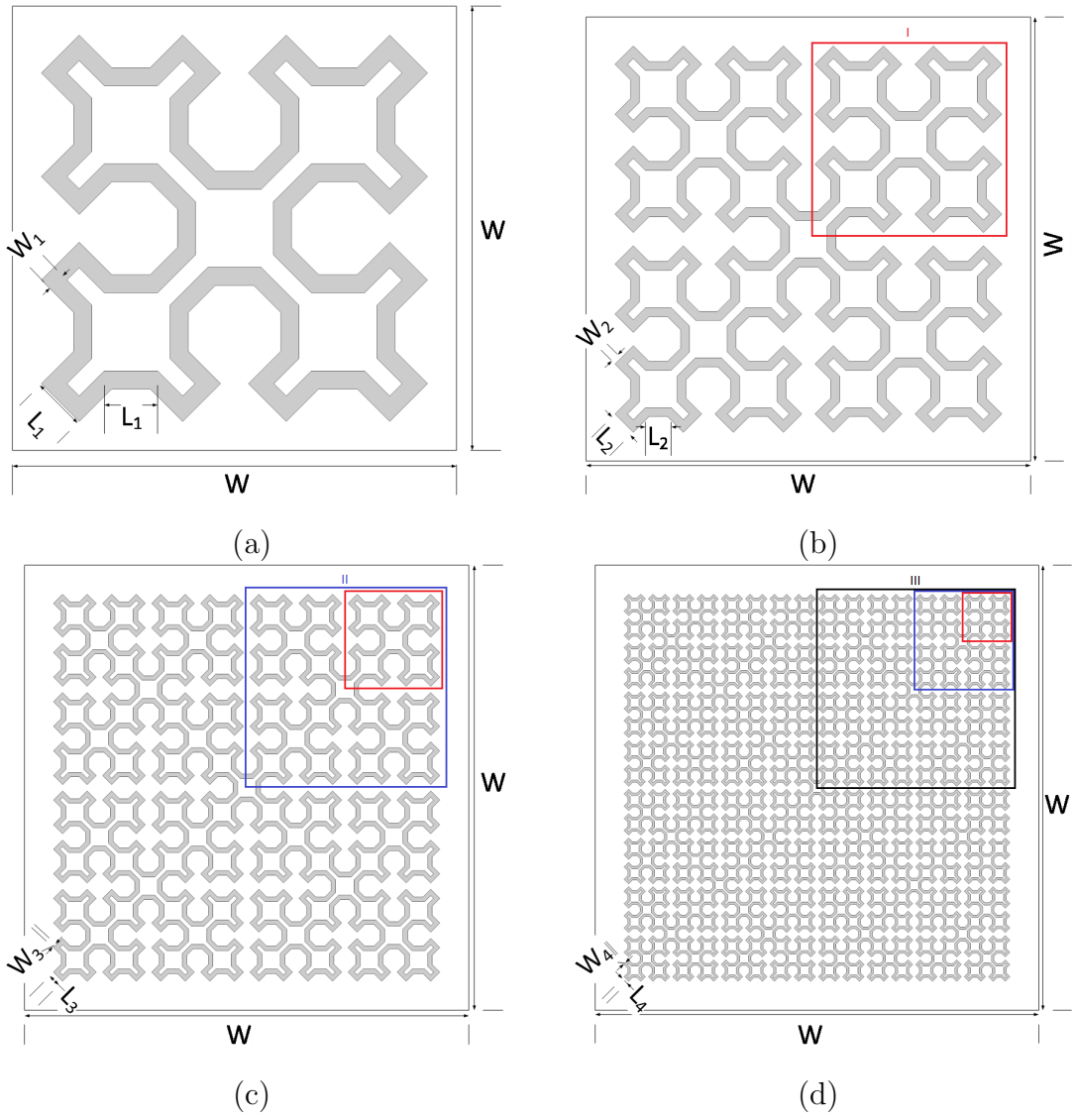

Figure 6.14: Proposed unit cell structure with different steps of the Sierpinski curve. (a) Step one. (b) Step two. (c) Step three. (d) Step four.

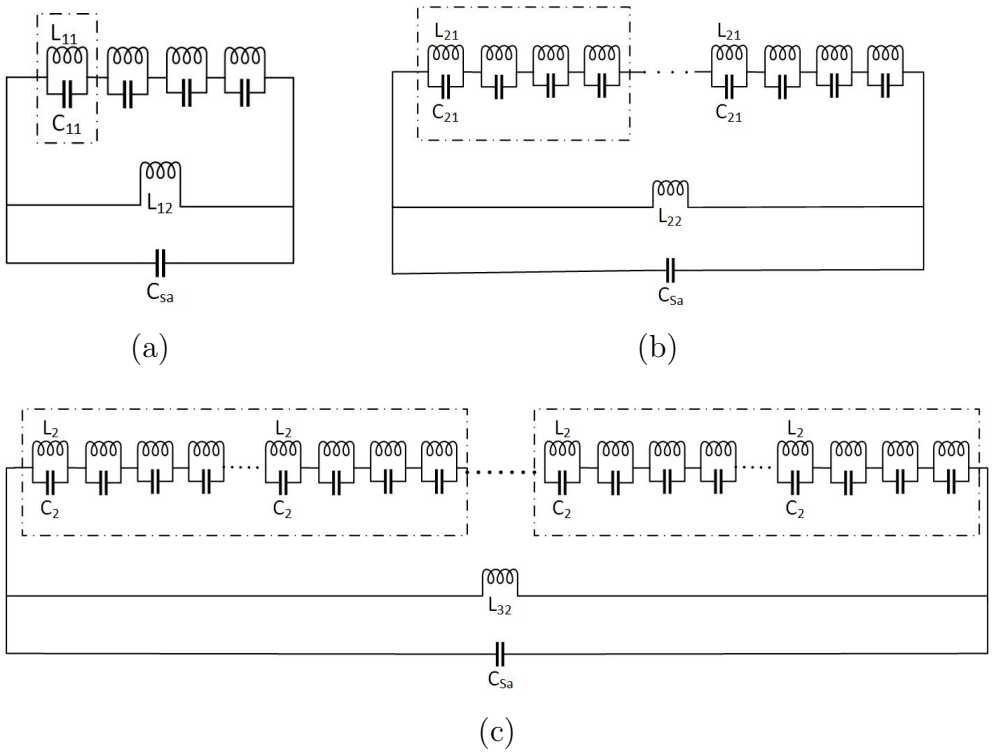

Figure 6.15: Equivalent circuit for each step of the Sierpinski curve. (a) Step one. (b) Step two. (c) Step three.

length decrease to $W_3 = \frac{W_1}{4} = 0.25mm$ and $L_3 = \frac{L_1}{4} = 0.725mm$, respectively. Considering the parameters that affect resonance frequencies, we have calculated the length and area of the curve [**?**]. The areas of the top-layer metal for steps one to four are 151.43 mm^2, 142.14 mm^2, 137.33 mm^2, and 135.08 mm^2, respectively. It can be noted that as the orders increase, the area of the metallic part decreases. The outer length of the curve from step one to step four can be calculated as 158.86 mm, 303.44 mm, 594.4 mm, and 1177.92 mm, which dramatically increases the length of curve. Furthermore, the number of small loops increases as the order of the curve increases. Thus, a very large inductance is stimulated, whereas the capacitance value is not changing that much. This phenomenon enables the structure to exhibit strong resonances in frequencies as low as 900 MHz in the third step of the curve. This phenomenon also can be illustrated with its equivalent circuit, as shown in Fig. 6.15(c). The large inductance stimulated by the curve denoted as L_{32} and the main capacitance, C_{sa}, are almost the same as the previous step. These values are enabling a 99% absorption ratio at 900 MHz. Moreover, the combination of these resonators stimulates more resonance frequencies in the structure. Thus, a multi-band absorber can be achieved utilizing this technique. Following this approach, the fourth order of the Sierpinski curve is also simulated to verify the logic of the behaviour of the absorber relative to the curve order. As illustrated in Fig. 6.14(c), the number of loops increases sharply. However, the cross-section area of each loop decreases compared to the third step. Since the value of inductance is related to the area of the loops and the square of the number of loops, the equivalent inductance of the structure increases. Furthermore, the capacitance of the structure remains unchanged due to the increase in the mutual effect between metal paths, indicated as C_{11} in the circuit of Fig. 6.14(a), and decrease in the surface area. Consequently, the first resonance of the system is moved to 500 MHz. However, according to the uniform distribution of the metal layer on the surface of the substrate and its space-filling properties, at higher orders, the ratio of the return loss increases, and thus, the absorption ratio decreases.

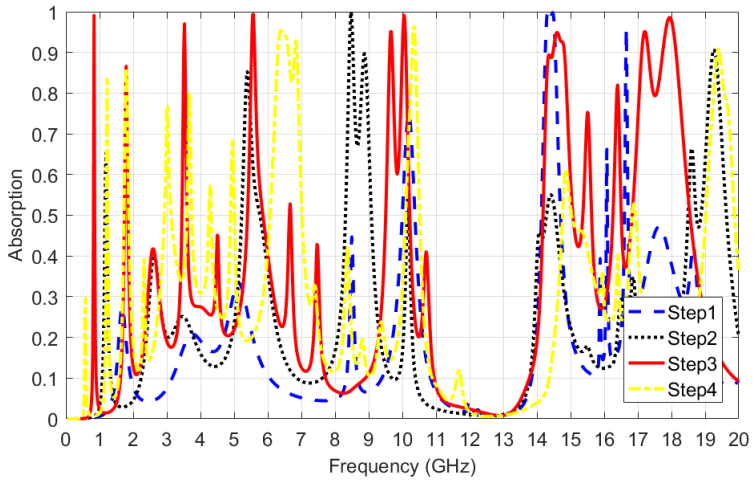

Figure 6.16: Absorption ratio for four steps of the proposed structure.

6.6.2 Simulation results

Perfect absorption depends on the resonance frequencies of the MPA structure, where the structure presents an impedance equal to the free space impedance. To illustrate the resonances of the system, Fig. 6.17 represents the E-field density for step three of the design. As discussed above, the whole structure is engaged with the resonances at lower frequencies. Fig. 6.17(a) shows the E-field density at 900 MHz and demonstrates the whole curve engagement with the resonance. At 10 GHz, Fig. 6.17(b), half of the structure is stimulated to provide the matching impedance and perfect absorption. Fig. 6.17(c) visualizes the E-field density at 18 GHz and provides a clear understanding of the roles of the smaller capacitors and inductors in higher frequencies. It can also be seen that at higher frequencies, the air gap plays a critical role.

The use of an absorber in a real-world scenario requires an insensitivity to the polarization and angle of the incident wave. To demonstrate the performance of the proposed approach, Fig. 6.18 represents the absorption ratio for various angles of oblique wave and polarizations. Fig. 6.18(a) compares the absorption ratio for different angles of the incident wave. The structure performs well for lower frequencies (less than 12 GHz) for the incident wave angle

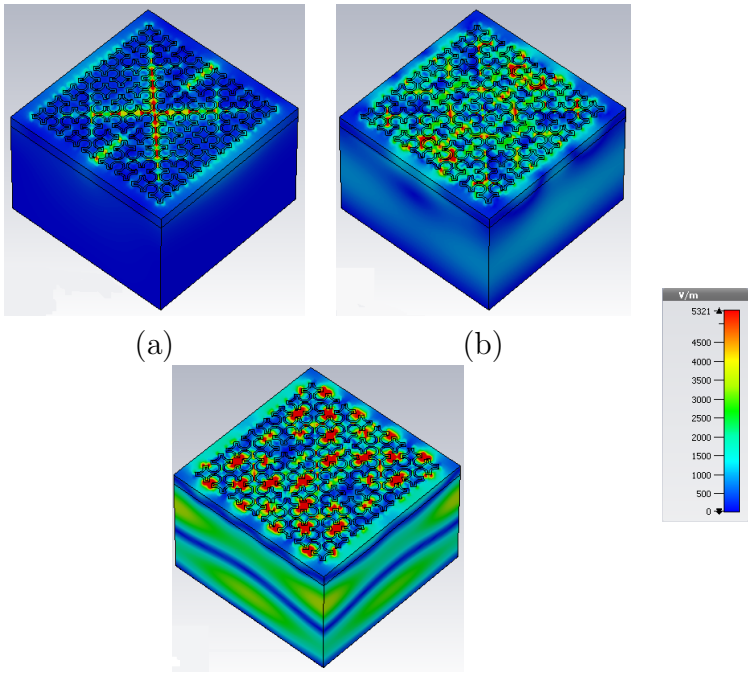

(a) (b)

(c)

Figure 6.17: E-field density for the system at three different resonance frequencies: (a) 900 MHz, (b) 10 GHz, (c) 18 GHz.

(θ) of 0 to 80. For instance, the absorption ratio at 900 MHz is greater than 60% for $\theta = 70$. As mentioned, polarization insensitivity is usually one of the requirements in absorber designs. Fig. 6.18(b) represents the performance of the structure for various polarization angles (ϕ). The proposed approach exhibits a good performance for all the values of ϕ due to its symmetric and unique structure.

6.6.3 Measurement results

To evaluate the proposed structure, an array of its third step with total dimension of $100 \times 100 \times 11.6\ mm^3$ is fabricated on a substrate of $FR4$ with relative permittivity of 4.4 and dielectric loss of 0.02, as shown in Fig. 6.19. To verify the absorption ratio, the fabricated absorber was tested using the horn antenna technique, as described in [146]. A Keysight PNA Network Analyzer N5225A was used in S-parameter measurements. First, using a

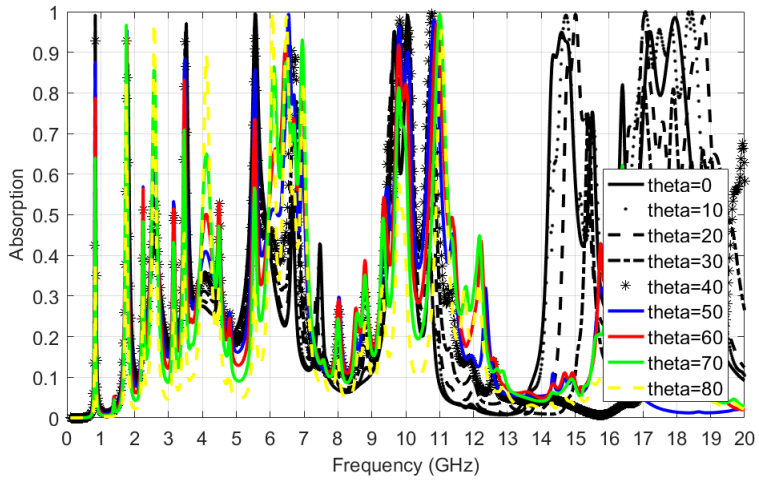

(a)

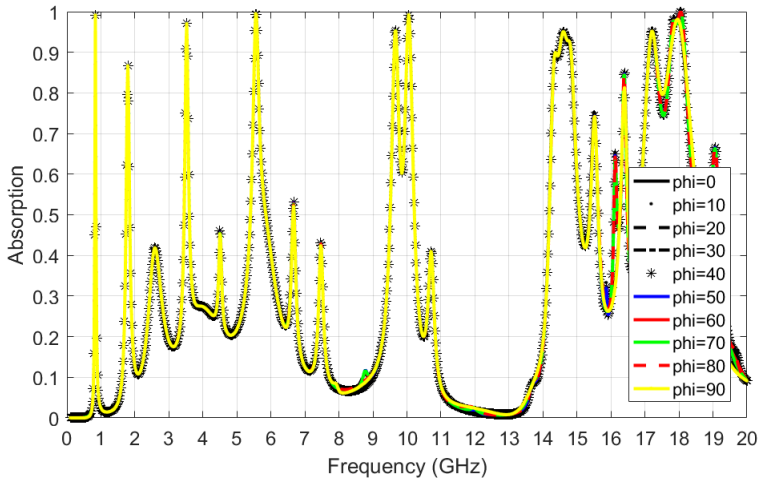

(b)

Figure 6.18: Absorption ratio for different angles of incident wave and polarization. (a) Absorption ratio for various θ. (b) Absorption ratio for various ϕ.

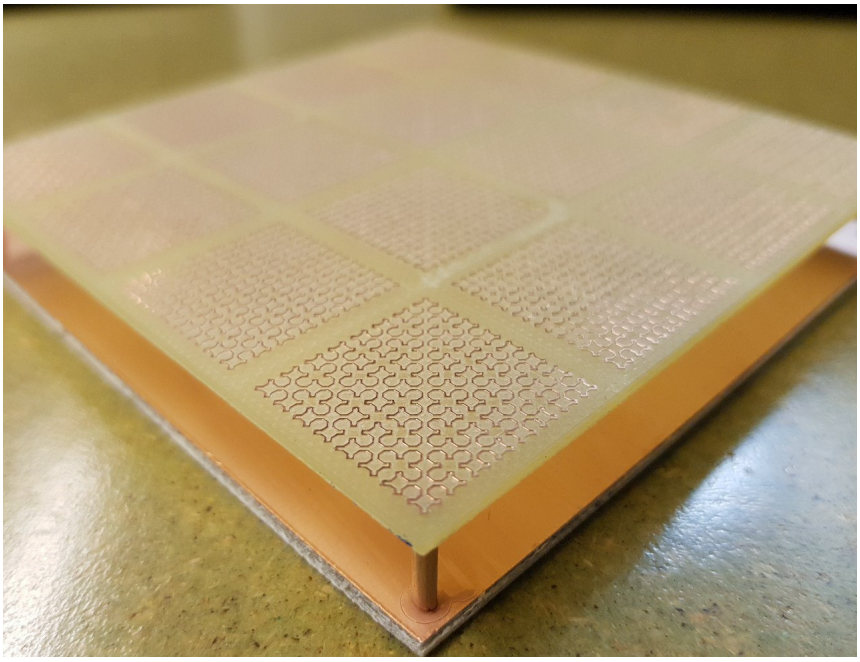

Figure 6.19: Fabricated array of the proposed structure.

plane copper plate, the S_{21} was measured to calibrate the network analyser. Having zero as the result of S_{21} measurement, the absorption ratio can be calculated as $1 - |S_{11}|^2$. This process eases the measurement process of the absorption ratio for the proposed structure. Fig. 6.20 compares the measurement and simulation results. It is clear that there is a good agreement between the simulation and measurement results.

6.7 Conclusion

In this chapter, a brief overview of the history and physics behind metamaterials and metamaterial absorbers was provided. The parameters that affect the designs illustrated and various applications for metamaterials and absorbers were discussed. It is noteworthy to mention that use of metamaterials offer a low cost solution to measure the level of available electromagnetic energy. Moreover, absorbers can be designed to have nearly 100% absorption in specific frequencies, enabling detection of slight changes in the environment.

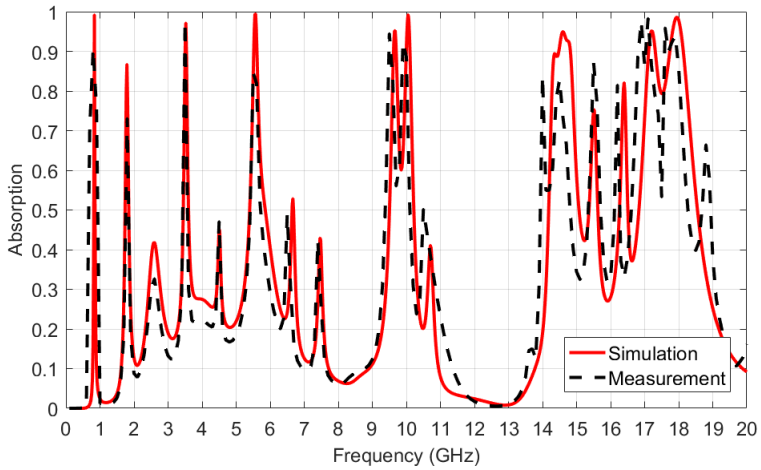

Figure 6.20: Comparison between measurement and simulation results.

Ref.	Fractal type	Size	Lowest band	Absorption ratio	Number of bands
[132]	Square loop	0.06λ	910 MHz	%99.9	1
[147]	Minkowski	0.25λ	870 MHz	%99.8	1
[148]	Minkowski	0.2λ	5 GHz	%95	1 Wide
[138]	Circular Minkowski	0.32λ	8.7 GHz	%98.47	3
[149]	Tree Shape	0.18λ	6 GHz	%90	3
[146]	Circular shape	0.4λ	10 GHz	%99.8	1
This work	Sierpinski	0.075λ	900 MHz	%99.9	8

Table 6.1: Size and performance comparison.

A new approach for designing compact low-frequency metamaterial absorber based on space-filling curves was presented. The proposed structure uses the Sierpinski curve, one of the well-known space-filling curves. The first four orders of the curve were simulated to understand its behaviour, and the resonance frequencies and absorption ratios were calculated. It was shown that using higher orders of the curve can stimulate resonances in low frequencies, while the unit cell size is fixed. The proposed unit cell has a size of $25 \times 25 \times 11.6\, mm^3$ ($0.0751\lambda \times 0.0751\lambda$ at 900 MHz). However, considering fabrication restrictions, there is a limit to higher-order implementation. Table 6.1 provides a comparison between the proposed structure and recent works in the literature. The first-order structure has two absorption bands at 14.4 GHz and 16.7 GHz. In the second step, a resonance at 19.3 GHz is stimulated, whereas the other two resonances have moved to 8.5 GHz and 5.3 GHz. In the third step, eight resonances with absorption rates of greater than 90% are introduced into the system. It is noteworthy that the first absorption band is at 900 MHz, with an absorption ratio greater than 99.9%.

Chapter 7

Polarization-Insensitive Metamaterial Perfect Absorber for Crowd Estimation Based on Energy-Level Measurements of Ambient Electromagnetic Waves

Non-invasive crowd estimation has remained a challenging issue among researchers. Methods such as image analysis and WiFi/Bluetooth probing can always be used to identify and track people. Lately, we have introduced a non-invasive method for crowd estimation based on ambient RF energy measurements. In this chapter, a polarization-insensitive multi-layer metamaterial absorber is introduced to measure the variation in the available RF energy levels for crowd estimation purposes. The proposed dual-band absorber is designed to absorb and transfer the maximum of the available WiFi energy to a lumped element to enable proper and accurate measurements. To evaluate the design, the proposed structure is fabricated as

an array, and its performance is tested, proving perfect absorption at the desired frequencies, 2.4 GHz and 5 GHz.

7.1 Introduction

Metamaterial absorbers, due to their specific characteristics, are one of the candidates to be used in this process as the energy measurement sensor. Metamaterials and absorbers are both used by researchers to enhance sensing capabilities in various systems. For instance, in [123], Ishikawa introduced a novel approach in infrared spectroscopic sensitivity using a plasmonic metamaterial absorber. In [140], Park *et al.* proposed a terahertz power meter using a thin-film metamaterial absorber. To enhance Co2 gas sensing, a hybrid polymer-metamaterial absorber in the mid IR spectral was investigated in [141]. In [142], Ni *et al.* introduced a humidity sensor based on a metamaterial absorber on silicon. Combining microfluidic techniques with metamaterial absorbers, Kim *et al.* introduced an ethanol chemical sensor that uses variations in the resonance frequency (from 10.42 to 11.46 GHz) to determine the concentration of ethanol [143]. Given these examples, it can be noted that most of the research has focused on high frequencies, especially in the terahertz regime, and the design of a metamaterial absorber for lower frequencies for sensing purposes is still a challenge to overcome. In this work, we present a novel approach for the design of a metamaterial absorber targeting two available WiFi bands: 2.4 GHz and 5.1 GHz. At present, indoor environments are densely equipped with WiFi access points, making WiFi a good source of EM energy in crowd estimation. The designed structure is a combination of a miniature periodic structure with the size of $18 \times 18 \times 1.75\, mm^3$, offering an absorption ratio of 99.9% in both frequency bands. A new technique of using single vias accompanied with lumped resistors is introduced to help to reduce the size while enabling the proper measurement of the amount of absorbed energy without interfering with the absorber structure. Compared to

previous work, which considered changing RF signal strength for crowd estimation by using a grid of active sensors, this approach introduced a passive method to implement lifetime battery-less devices.

7.2 Structure design and simulation results

Metamaterials are synthetic compositions of periodic metallic structures that are printed on a substrate that controls the electric permittivity $\varepsilon(\omega)$ and magnetic permeability $\mu(\omega)$ of the structure with respect to the operating frequency. This phenomenon occurs due to the stimulation of capacitors and inductors in the structure, which are triggered with the induced surface current. Then, at the resonance frequency, the effective impedance equals the free space impedance ($Z(\omega) = \sqrt{\frac{\mu(\omega)}{\varepsilon(\omega)}} = 1$).

The effective impedance can be calculated based on the reflection and transmission parameters

$$Z(\omega) = \sqrt{\frac{(1 + S_{11}(\omega))^2 - S_{21}^2(\omega)}{(1 - S_{11}(\omega))^2 - S_{21}^2(\omega)}},\ \omega = 2f \tag{7.1}$$

The absorption, $A(\omega)$, will be perfect according to the definition:

$$A(\omega) = 1 - \Gamma(\omega) - T(\omega) \tag{7.2}$$

where $\Gamma(\omega) = |S_{11}|^2$ and $T(\omega) = |S_{21}|^2$.

Fig. 7.1 represents the 2D models of the proposed structure for the MPA unit cell with the size of $18 \times 18 \times 1.75\, mm^3$. The proposed unit cell consists of three layers that target two absorption frequencies. The top metal surface consists of a set of rings, where the inner radius of $R_{1in} = 3.4\, mm$ and outer radius or $R_{1out} = 2.7\, mm$, are connected through symmetric lines with the line width of $W_1 = 0.7\, mm$. The mid-layer also consists of four

rings with inner radius of $R_{2in} = 1.25\,mm$ and outer radius or $R_{2out} = 0.55\,mm$, and the connection lines have a line width of $W_2 = 0.7\,mm$. Each layer is connected to the ground plane using four vias with the size of $R_{via} = 0.6\,mm$, while a lumped resistor is between the vias and the ground plane. The substrate thicknesses are indicated with $h_1 = h_2 = 0.75\,mm$.

7.2.1 Design procedure

The body absorption and its effects are different at various frequencies, which have been vastly studied in the literature [150, 151]. Accordingly, having a multi-resonator absorber that can independently set frequencies helps to increase the accuracy of the measurements and estimations. The human body shows two main resonance frequencies at 60 MHz and 2 GHz [97]. However, the lack of ambient RF energy at 60 MHz and the size of the unit cell in this frequency (60 MHz) make the system move to more available frequencies, especially indoors. Thus, the focus of the design is WiFi bands (2.4 GHz and 5 GHz). Nonetheless, the resonance bands can be manipulated by following the same procedure and only changing the size of the entire unit cell. Furthermore, it is worth noting that the structure should be capable of absorbing all possible polarisations. Therefore, the proposed structure is symmetric with respect to the origin of the unit cell.

A multi-layer symmetric structure is proposed with the purpose of providing a multi-resonance absorber [152–156]. The multi-layer structure is used to enable frequencies to be set independently. In the proposed approach, the top layer is set to absorb the lower frequency band (2.4 GHz), while the mid-layer is stimulated at higher frequencies (5.1 GHz). This combination is created due to the higher energy levels of high-frequency waves and ease of penetrating into the substrate. Therefore, the top layer of the structure is designed to resonate at 2.4 GHz, while the mid-layer resonates at 5.1 GHz. Fig. 7.2 shows real and imaginary values of the effective impedance. It can be seen that at 2.4 GHz and 5.1 GHz, the structure shows perfect matching impedance.

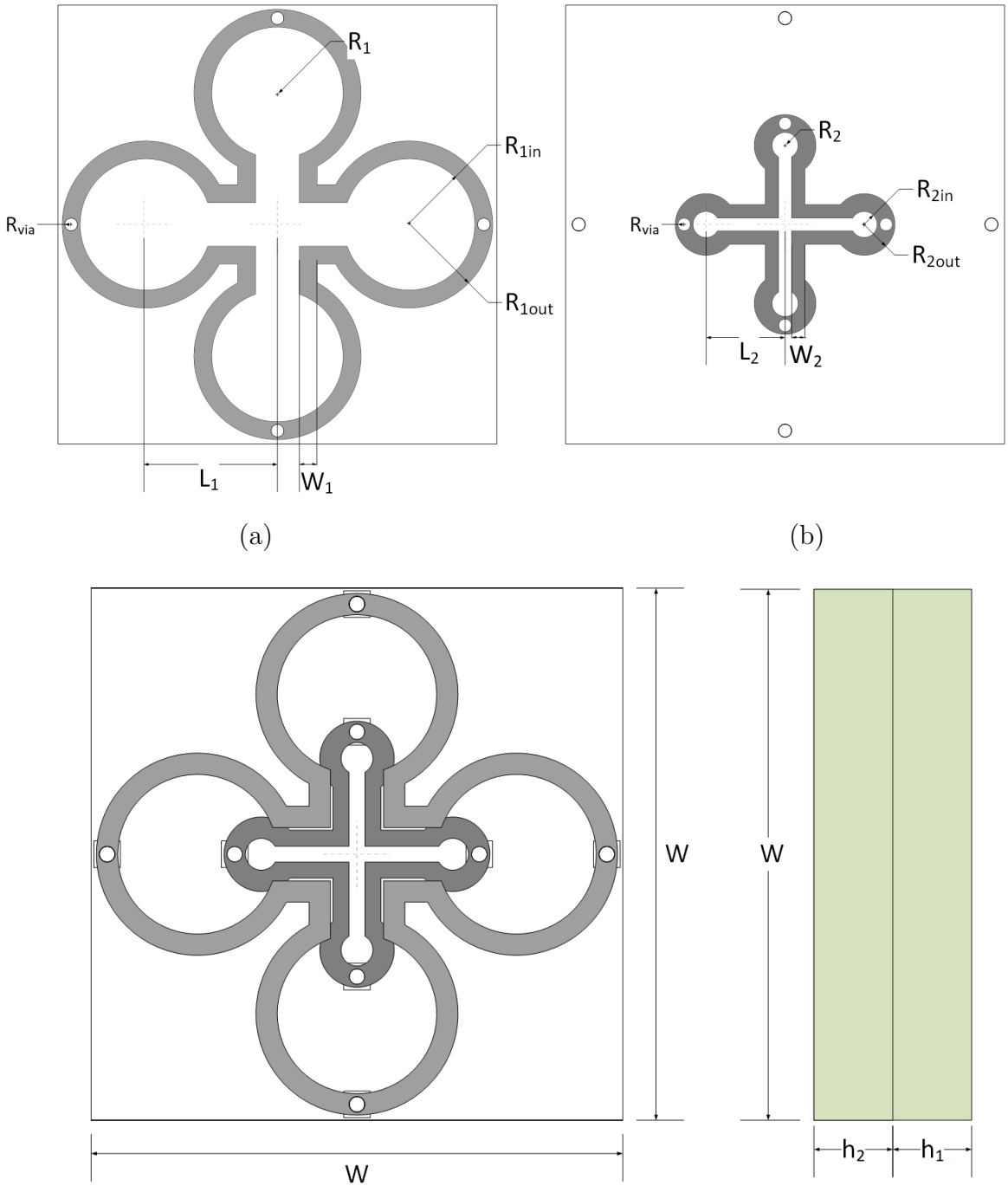

Figure 7.1: Proposed structure of the metamaterial absorber. (a) Top layer. (b) Mid layer. (c) Full unit cell.

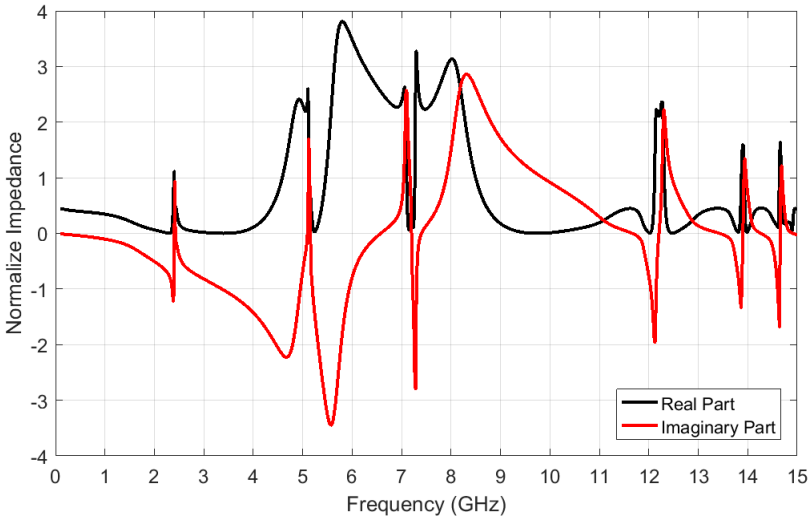

Figure 7.2: Real and imaginary values of $Z(\omega)$.

Fig. 7.3 illustrates the E-field, H-field and induced surface current distribution for both frequency bands in the top and mid layers. Noting the E-field distributions in Fig. 7.3(1:a) and (1:b), the concentration of the E-fields proves the functionality of the top layer and mid layer at 2.4 GHz and 5.1 GHz, respectively. With a horizontal linear polarised wave at 2.4 GHz hitting the absorber, two horizontal rings at the top layer of structure are involved (Fig. 7.3(1:a)). By changing the polarisation angle from 0 to 90, we transfer the E-field and induced surface current focus area to the vertical set of rings instead of horizontal ones. Thus, the polarisation insensitivity is guaranteed in the structure. Furthermore, the measured E- and H-fields (Fig. 7.3(1:a) and (2:a)) at 2.4 GHz are negligible in the mid layer compared to those in the upper layer. At 5.1 GHz (Fig. 7.3(1:b) and (d)), the mid layer plays the main role and provides the impedance matching, which shows that the top and mid layers of the structure act separately. Thus, the absorption bands can be easily adjusted by manipulating the size of the rings in each layer.

Fig. 7.4 illustrates the role of the radius of the rings in each layer to set the resonance frequencies. We set the fixed dimensions for the unit cell as $18 \times 18\, mm^2$, and R_{1in} and L_1

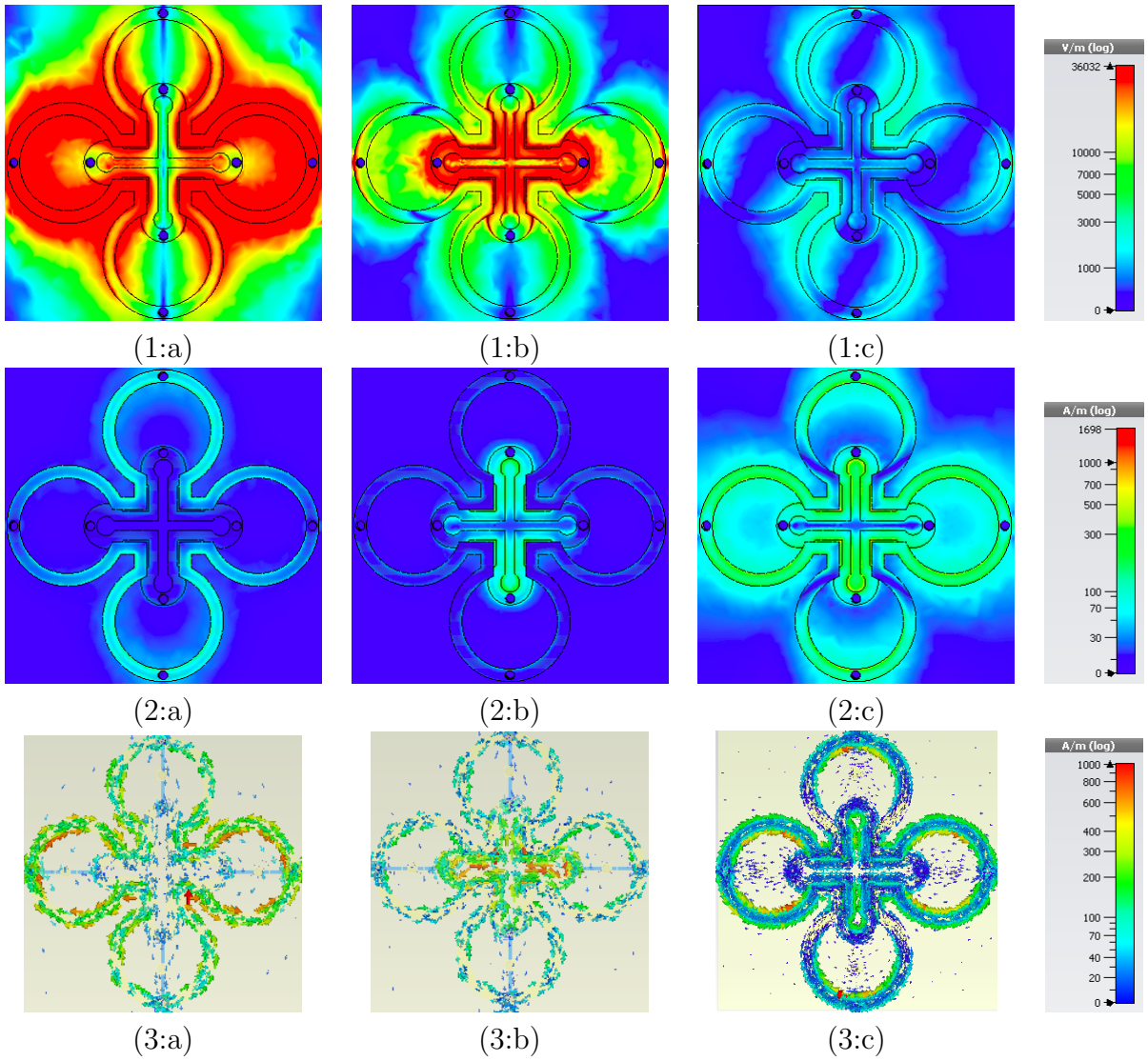

(1:a) (1:b) (1:c)

(2:a) (2:b) (2:c)

(3:a) (3:b) (3:c)

Figure 7.3: (1:*) E-field distribution at (a) 2.4 GHz; (b) 5.1 GHz; (c) 7.2 GHz. (2:*) H-field distribution at (a) 2.4 GHz; (b) 5.1 GHz; (c) 7.2 GHz. (3:*) Induced surface current at (a) 2.4 GHz; (d) 5.1 GHz; (c) 7.2 GHz.

are inversely related to each other. As represented in Fig. 7.4(a), by reducing the radius R_{1in} of the circles on the top layer and consequently increasing the length L_1 of the lines, the equivalent electrical length of the resonator decreases, and the resonance frequency increases. The phenomenon of independent adjustment of the resonance frequency repeats in the mid-layer at 5.1 GHz, as illustrated in Fig. 7.4(b). Moreover, as shown in Fig. 7.4, a third resonance appears at 7.2 GHz. In Fig. 7.3(1:c) and (2:c), which shows the E- and H-fields at 7.2 GHz, this resonance is a result of the mutual effect of the rings in the upper and middle layers. In Fig. 7.3(2:c), the anti-parallel currents between two layers are strong and result in a strong magnetic field.

With fixed radii for the rings as $R_1 = 3\,mm$ and $R_2 = 0.85\,mm$, the effect of the line width is investigated. Fig. 7.5 shows the changes in absorption ratio and resonance frequencies with a small change in line width. With $W_1 = W_2 = 0.6\,mm$, the resonance frequency of the structure slightly moves to lower bands as 2.38 GHz and 5.05 GHz. With $W_1 = W_2 = 0.8\,mm$, the resonance frequency slightly shifts to higher bands at 2.43 GHz and 5.33 GHz. Thus, the line width of $W_1 = W_2 = 0.7\,mm$ is fixed for both resonators.

Absorbers were traditionally designed to trap electromagnetic waves and dissipate them. However, a higher efficiency of the absorbers in catching signals enables new applications in the field of sensing. Similar to most sensing applications, the proposed sensing application in this chapter requires the detection of the changes of the available RF energy levels. To provide this function, the loss of the system should be minimal, and the absorbed power should be transmitted and translated to a measurable parameter. Thus, a substrate of *Rogers RO*3003 with the thickness of $h_1 = 0.75\,mm$ and $h_2 = 0.75\,mm$ and loss tangent of 0.001 is selected.

Fig. 7.6 represents the simulation analysis of the power loss in the structure. For simulations, the structure is placed in front of a transmitter with an outgoing power of 0.5 watt. At resonance frequencies of 2.4 GHz, 5.1 GHz and 7.2 GHz, the accepted power in the structure

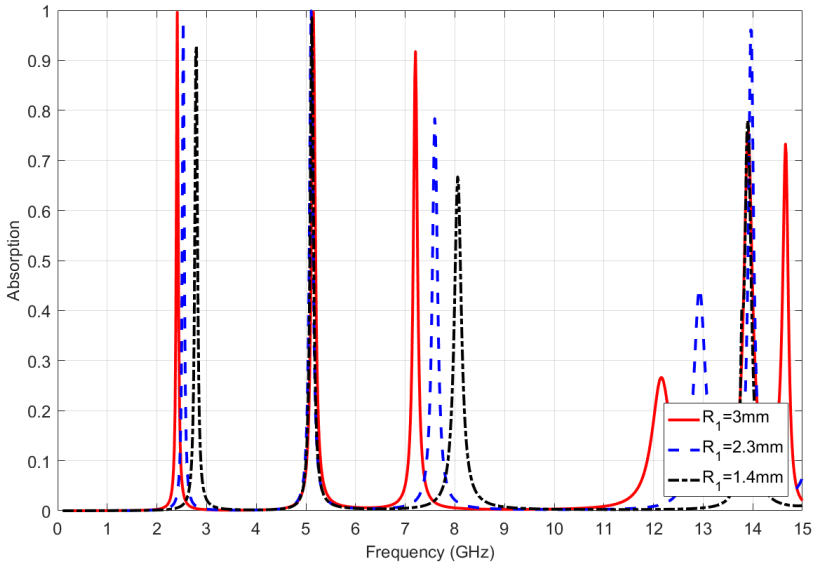

(a)

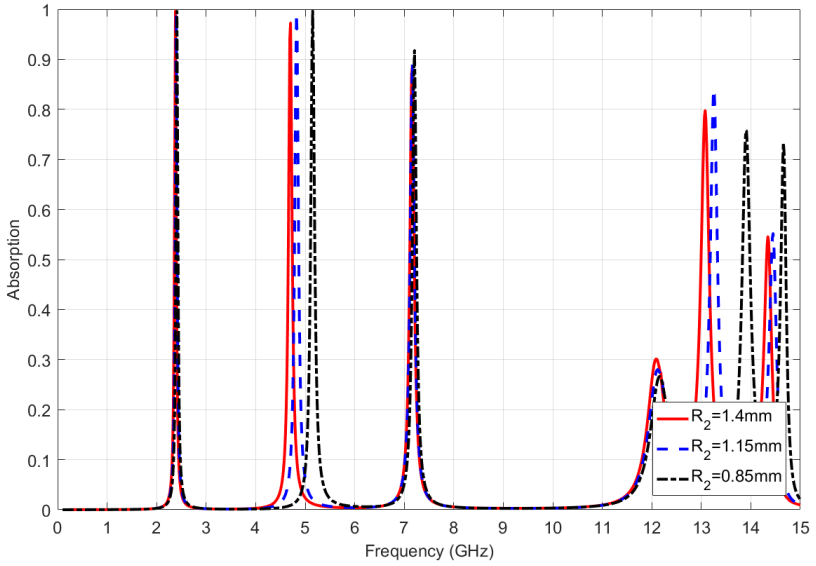

(b)

Figure 7.4: Effect of the radius of the rings. (a) Various values of R_{1in} with $R_{2in} = 0.85mm$. (b) Various values of R_{2in} with $R_{1in} = 3mm$.

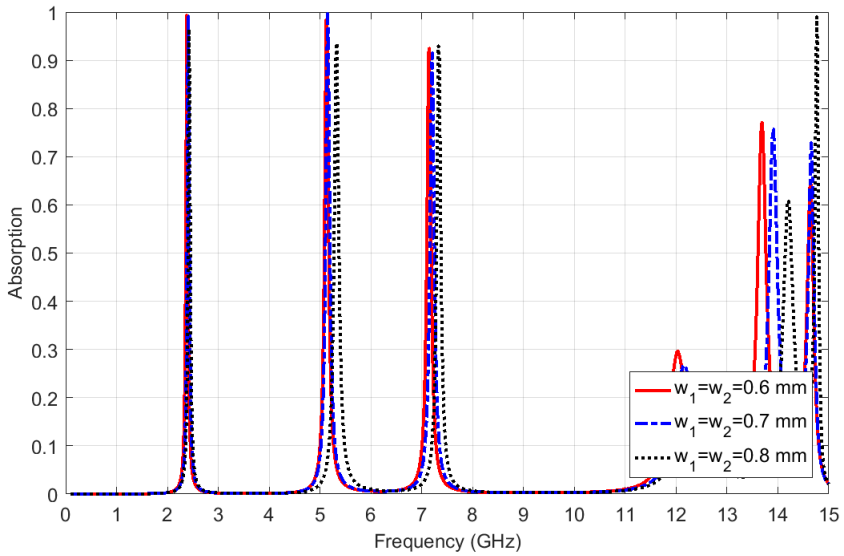

Figure 7.5: Effect of the line width on the resonator.

are approximately 100%, 45% and 85%, respectively. At 2.4 GHz, 0.5 watt RF energy is absorbed with the structure, while 0.19 watt is wasted in the metal and substrate (0.145 watt in the metal parts of the structure and 0.045 watt in the dielectric substrate). Thus, 0.31 watt is transferred to the lumped element. At 5.1 GHz, the accepted power on the mid-layer resonator is 0.23 watt due to the loss in the upper layer. However, the loss in the metal and substrate is relatively low, and 0.14 watt can be transferred to the lumped elements. As mentioned, at 7.2 GHz, both resonators are engaged, so 85% of the power is accepted with the structure. Furthermore, the proposed metamaterial absorber is introduced to operate as a sensor in the crowd estimation analysis based on the RF energy measurements. To this end, the absorbed energy should be translated to measurable parameters. The power analysis in Fig. 7.6 shows that 62% and 28% of available RF energy can be transferred to the lumped elements. Measuring the voltage and current on these elements would be used to determine the changes in amount of available EM energy.

As mentioned, one of the challenges in using an absorber as a sensor is to transfer the absorbed power and translate it to a measurable parameter. One of the common techniques

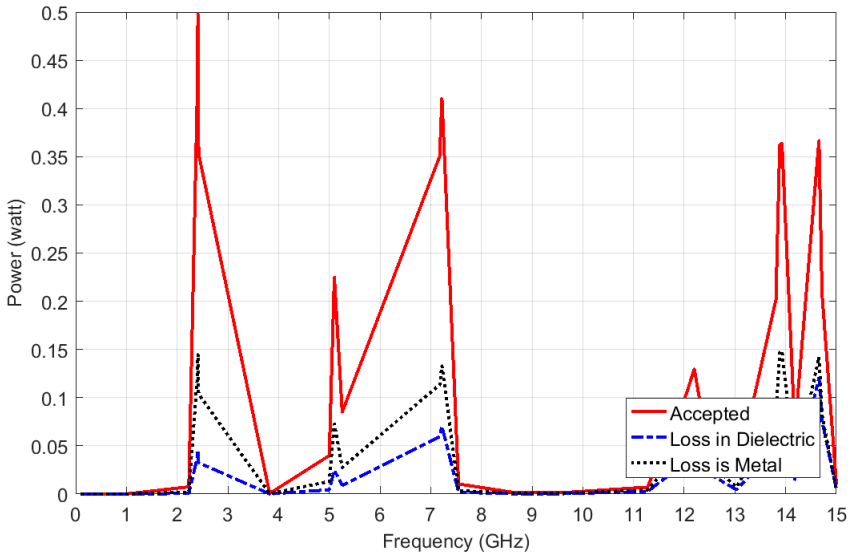

Figure 7.6: Power loss analysis in the structure.

to translate the power to a measurable parameter is to use lumped resistors. Thus, the voltage can easily be measured. However, placing lumped resistors on the top layer of the absorber makes the measurement process almost impossible due to the parasitic effects of the added or connected equipment. Therefore, the technique of using vias and defecting the ground plane is introduced in this work. In this technique, our vias are added in each resonator, which is connected to the ground plane through resistors. These vias are used to control the induced surface current directions and redirect the current into the resistors, which are placed at the bottom layer of the absorber. Thus, when the current passes the resistor, the voltage on the resistor can be measured. Considering the direct relation of the induced surface current with the amount of absorbed energy, the proposed structure is used to measure the amount of available RF energy and monitor its changes. It is worth noting that the use of vias and the connection to the ground plane through lumped resistors introduce new routes for the induced surface current transferring maximum power to the resistor. This feature also helps to yield more accurate measurements of the changes. The effect of the lumped resistors and its values are shown in Fig. 7.7. As shown, a wide range of

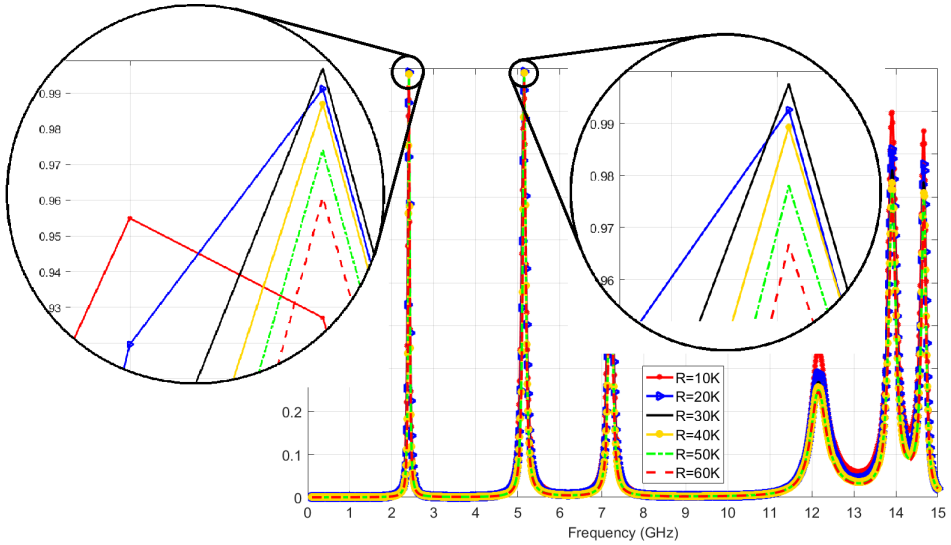

Figure 7.7: Effects of the resistor values on the absorption levels at 2.4 GHz and 5 GHz.

resistors (10 $K\Omega$ to 60 $K\Omega$) are considered, and $R = 30\ K\Omega$ is selected for both resonators. It should be mentioned that the values of the resistors are critical to the absorption ratio. Considering the RLC resonator circuit model for a unit cell, the resistor should be selected with respect to the inductance and capacitance of the resonator to provide perfect resonance. The symmetry of the design is guaranteed by having four resistors for both layers.

As mentioned, according to the application, the structure should be insensitive to the polarisation and incident angle. Fig. 7.8 shows the performance of the proposed structure with various oblique angles and polarisations. Despite a small shift at 2.4 GHz, the proposed absorber shows good absorption (over 75%) from $\theta = 0$ to $\theta = 70$ at both frequencies as shown in Fig. 7.8(a). The absorption ratio remains over 99% for all polarisation angles, ϕ, as shown in Fig. 7.8(b).

7.2.2 Proposed absorber as a sensor

Metamaterial absorbers can provide an efficiency of 100% on its resonance frequencies. This feature enables us to detect small changes in the level of available electromagnetic energy.

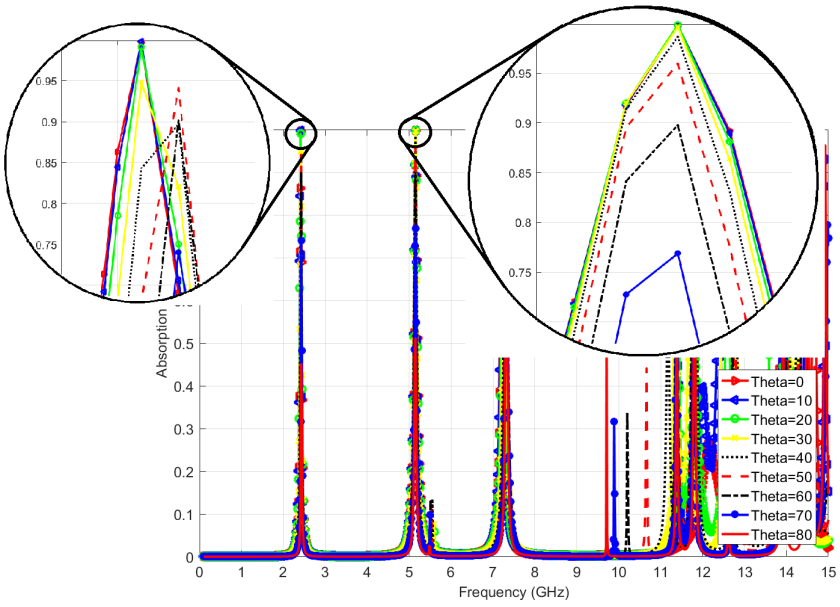

(a)

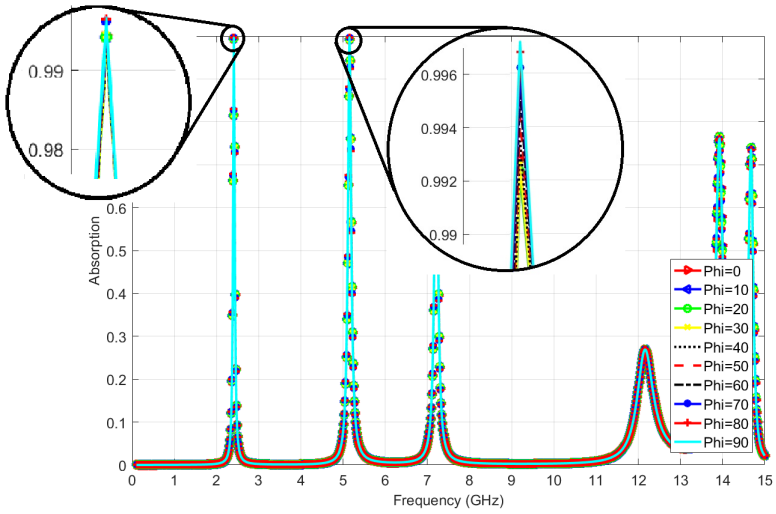

(b)

Figure 7.8: Absorption ratio for different angles of the incident wave and polarization. (a) Absorption ratio for θ; (b) Absorption ratio for ϕ.

Furthermore, these structures are low cost and easy to deploy in a large scale. So, metamaterial absorbers are good candidates to replace antennas in measuring electromagnetic energy levels.

The proposed metamaterial absorber is designed to act as a sensor by proving the changes in RF energy levels. The amount of output voltage and current are two parameters of sensitivity of metamaterial absorber as a crowd estimation sensor. As mentioned both resonators (top layer resonator and mid layer resonator) are stimulated independently in different frequencies and each resonator is connected to the ground through four lumped resistors. Therefore, effects of the body in different frequencies can be measured independently at 2.4 GHz and 5.1 GHz. This feature is illustrated in Fig. 7.9 by representing the simulation results for the measures of voltage and current on the lumped resistors regarding different input powers. Fig. 7.9(a1) and (a2) shows the measurable voltage values on the associated resistors at 2.4 GHz and 5.1 GHz, respectively. Comparing two graphs prove its independent functionality at 2.4 GHz and 5.1 GHz. Similarly, Fig. 7.9(b1) and (b2) represents the current values as a complementary measurable parameter for available RF energy.

Table 7.2 shows the simulation results for measurable values for the voltage and current with respect to various levels of transmitted power. Setting transmitting power as $-23\,dBm$, the measured voltage and current are 4.84 (V) and 161 (μA) at 2.4 GHz. These values are slightly higher at 5.1 GHz with measures of 5.39 (v) and 180 (μA) for voltage and current, respectively. Recalling the introduced application, sensitivity of the absorber plays critical role in the accuracy of measurements. Sensitivity of the absorber and respected measurements are also investigated in Table 7.2 by considering $3\,dBm$ changes in the level of transmitting power at both resonance frequencies. For $-3\,dBm$, the measured voltage is 48.48 (V), and the current is 1.61 (mA) at 2.4 GHz. At $0\,dBm$ for the transmitted power, the voltage is 68.64 (V), and the current increases to 2.28 (mA) at 2.4 GHz. Likewise, measurable parameters values are 54.16 (V) and 77.2 (V) for voltage and 1.79 (mA) and 2.56 (mA) for

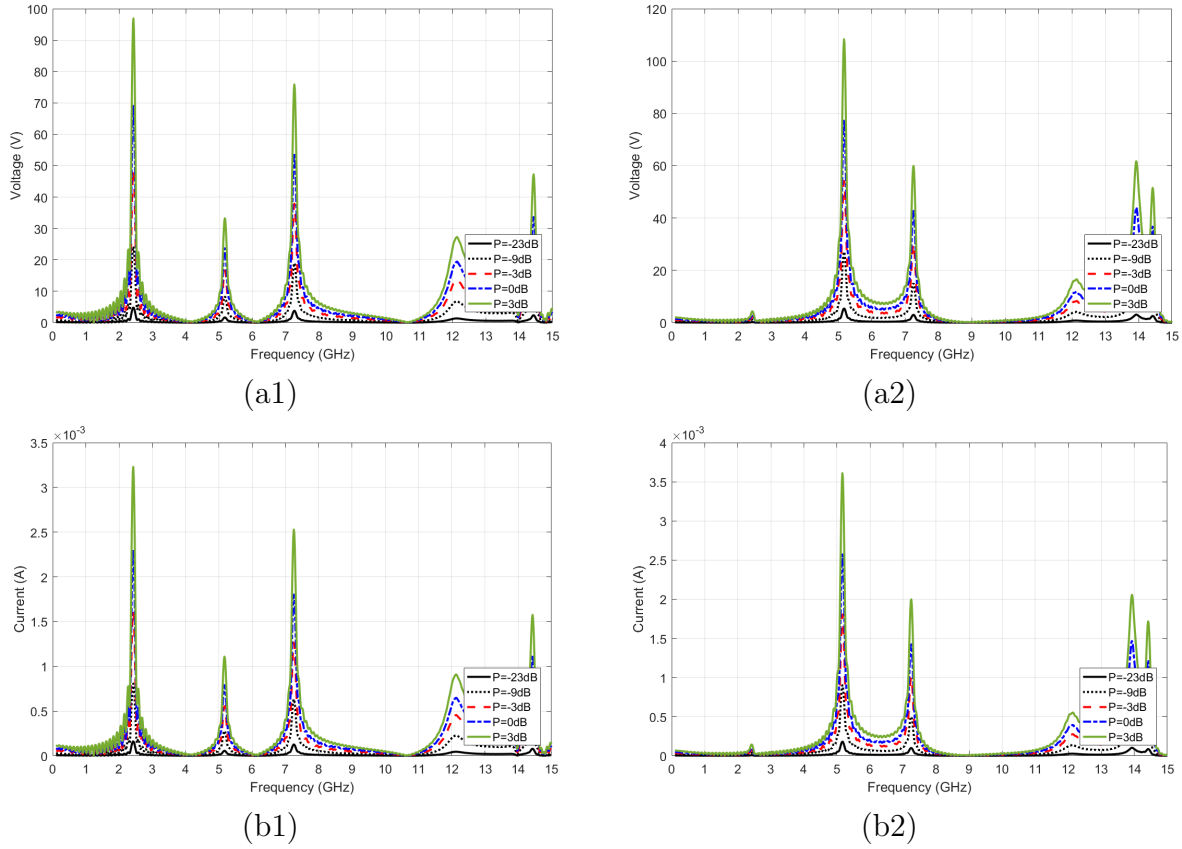

Figure 7.9: Simulation results for the voltage and current on the lumped elements. (a) Voltage on the lumped resistor (a1) 2.4 GHz (a2) 5.1 GHz; (b) current passing through the lumped resistor (b1) 2.4 GHz (b2) 5.1 GHz.

current with the transmitting power of $-3\,dBm$ and $0\,dBm$ at 5.1 GHz. These measurements prove that the proposed absorber reacts logically to the transmitted power and can be noted as a sensor. Therefore, any changes in the level of available RF energy can be tracked and an accurate estimation can be provided.

7.3 Measurement Results

The proposed approach is fabricated as an array to evaluate its performance in a real-world environment. Figs. 7.10(a) and (b) show the top and bottom layers of the fabricated 8×8

Frequency	2.4 GHz		5.1 GH	
Transmitted power (dBm)	Voltage (V)	Current (mA)	Voltage (V)	Current (mA)
-23 dBm	4.84 v	161 μ A	5.39 v	180 μ A
-9 dBm	24.24 v	806 μ A	27.1 v	900 μ A
-3 dBm	48.48 v	1.61 mA	54.16 v	1.79 mA
0 dBm	68.64 v	2.28 mA	77.2 v	2.56 mA
3 dBm	96.88 v	3.23 mA	107.63 v	3.6 mA

Table 7.1: Voltage and Current for various levels of transmitted power.

array of the proposed structure on a substrate of *Rogers* 3003. It is noteworthy to mention that resin epoxy is used to press different layers of substrate which pose a small shift on the resonance frequencies. The structure is used to test its performance in comparison with the simulation results. Then, the absorber is used to measure the changes of the available RF energy levels to prove its proposed application.

7.3.1 Measurements of the proposed absorber characteristics

To test the fabricated absorber, a setup as described in Fig. 7.11 is used [146]. The structure is fixed in front of the EMC pyramid absorbers to avoid the reflection when the power is radiating. Two horn antennas are connected to a network analyser (Agilent Technologies E5071B) to measure parameters S_{11}. Fig. 7.12 compares the measurement results of S_{11} of the system with its simulated results. It should be noted that epoxy resin is added into the structure during final simulations. Despite a small shift in resonance frequencies, the measurements are consistent with the simulation results and show perfect absorption at the desired resonance frequencies (2.05 GHz and 4.13 GHz). Moreover, the proposed structure is tested for performance evaluation in various oblique angles and polarisations. Fig. 7.13 shows the measurement results of its absorption ratio for various oblique angles and polarisations. The proposed absorber shows good absorption from $\theta = 0$ to $\theta = 70$ as shown in Fig. 7.13(a). As shown in Fig. 7.13(b), the absorption ratio remains over 90% for

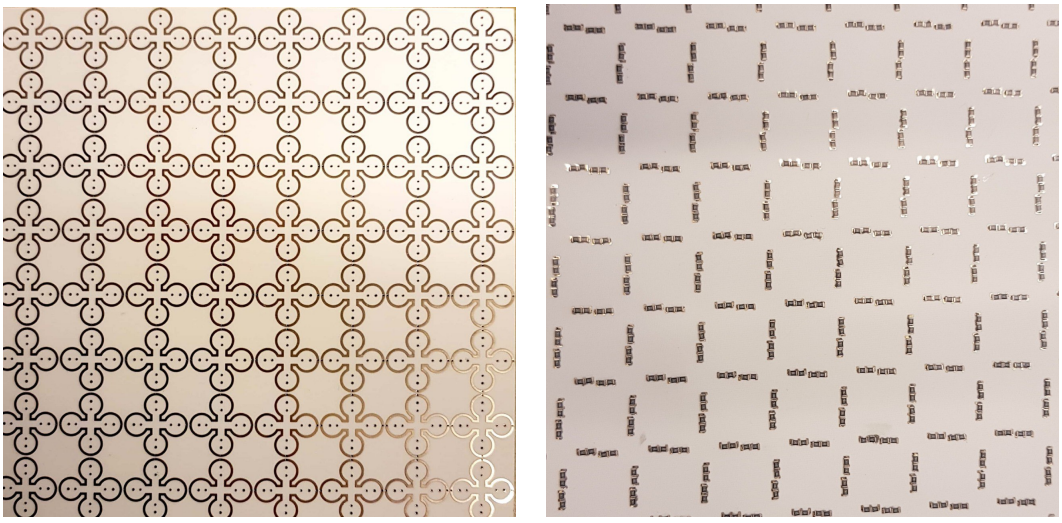

(a) (b)

Figure 7.10: Fabricated 8×8 array of the proposed absorber. (a) Top layer; (b) bottom layer

all polarisation angles ϕ.

7.3.2 Measurements of proposed absorber as a sensor

The proposed metamaterial absorber is designed to act as a sensor by proving the changes in RF energy levels. To test its functionality, the absorber is fixed in front of a transmitter antenna, and the voltage and current on the resistors are measured. Table 7.2 shows the measured values for the voltage and current with respect to various levels of transmitted power. Starting from $-30\,dBm$, the measured voltage and current are 1.5 (V) and 1 (mA), respectively. For $0\,dBm$, the measured voltage is 18.3 (V), and the current is 3.2 (mA). At $10\,dBm$ for the transmitted power, the voltage is 23 (V), and the current increases to 4 (mA). These measurements prove that the proposed absorber reacts logically to the transmitted power and can be noted as a sensor.

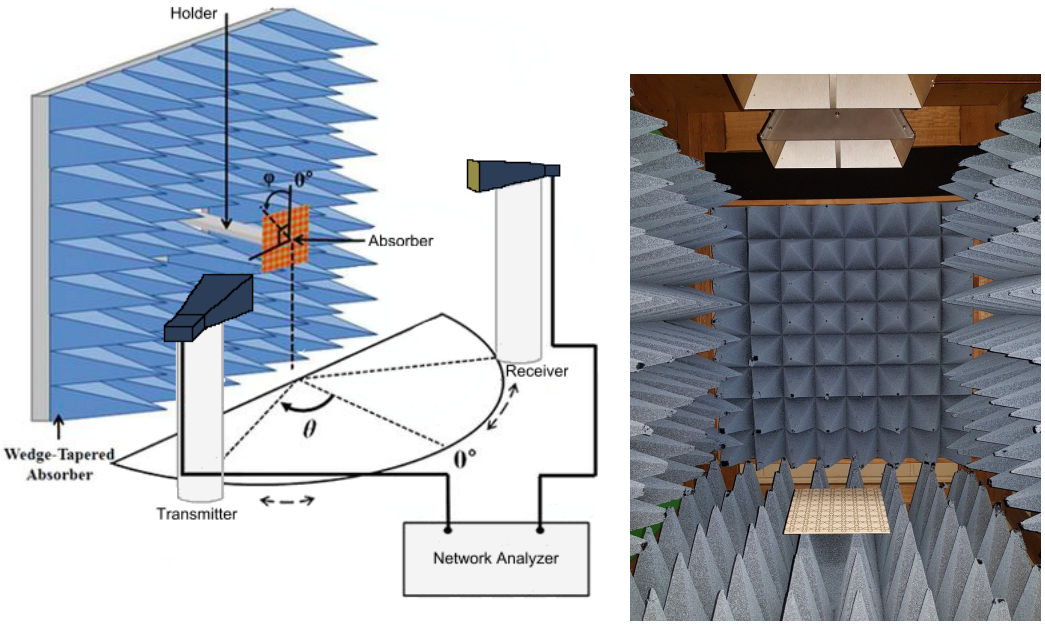

(a) (b)

Figure 7.11: (a) Setup for the absorber tests [146]. (b) Setup for experiments.

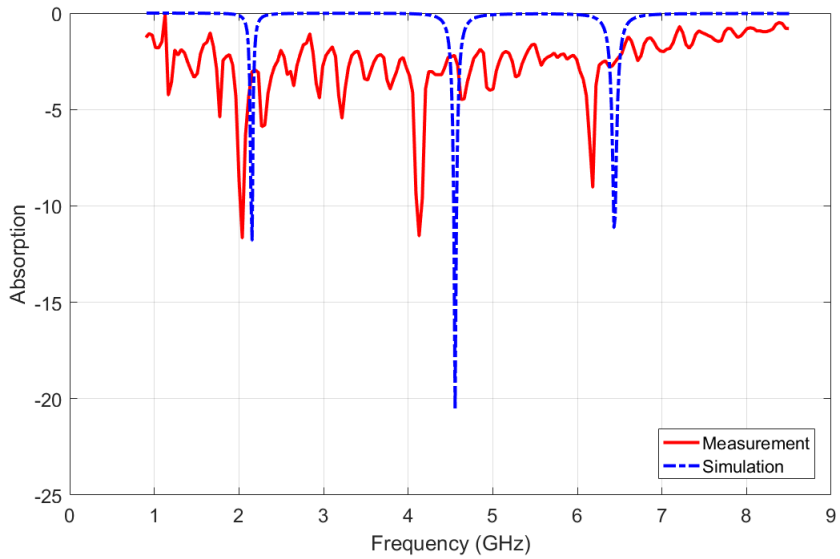

Figure 7.12: S_{11} measurement in comparison with simulations.

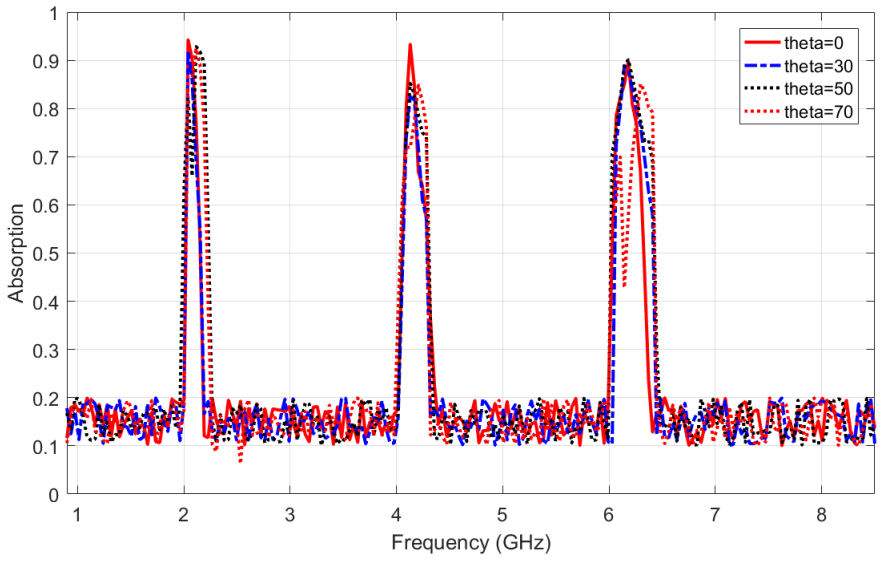

(a)

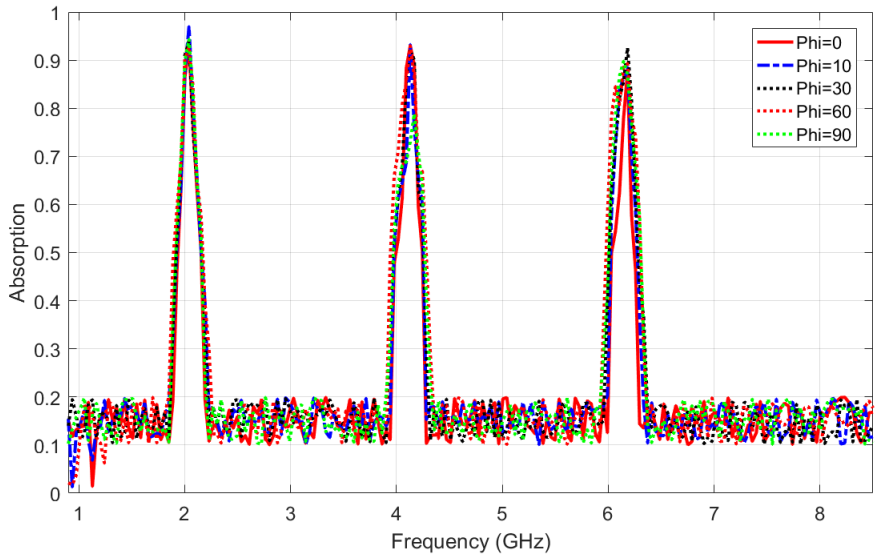

(b)

Figure 7.13: Measurement results for absorption ratio for different angles of the incident wave and polarization. (a) Absorption ratio for θ; (b) Absorption ratio for ϕ.

Transmitted power (dBm)	Voltage (V)	Current (mA)
-30 dBm	1.5	1
-20 dBm	3.7	1.5
-10 dBm	9.9	1.9
0 dBm	18.3	3.2
10 dBm	23	4

Table 7.2: Voltage and Current measurements for various levels of transmitted power.

7.4 Conclusion

A multi-layer polarisation-insensitive metamaterial perfect absorber has been introduced in this chapter to provide a solution for accurate measurements of the available RF energies to estimate the crowd. The proposed approach address the issue of the need for multiple antenna measurements for crowd estimations. The proposed unit cell with a size of $18 \times 18 \times 1.75\,mm^2$ operates at WiFi frequencies (2.4 GHz and 5.1 GHz). The unique structure of the proposed absorber enables perfect power absorption and its accurate translation to the voltage. Using single vias, the resistors move to the bottom layer of the structure to avoid any parasitic effects during measurements. The proposed structure has been fabricated, and its functionality regarding various levels of available RF energies have been tested.

Chapter 8

Conclusion

This chapter summarises the contributions of this dissertation. The final part of the chapter illustrates the remaining challenges in each section and future directions for studies.

8.1 Contributions

In chapter 3, participatory Bluetooth scanning was investigated as a crowd estimation method. The discovery probability of the Bluetooth protocol and detection probability were calculated. A wide range of experiments was designed and performed to collect data for the parameter estimation and model evaluation. The maximum likelihood estimation (MLE) is used to estimate the parameters of the probabilities using experimental results. The penetration rate is defined as the ratio of available Bluetooth devices to the total number of people. It has been proven that the probability of having k number of Poisson-distributed Bluetooth devices is a inhomogeneous Poisson distribution with density λ. Then, the crowd density is estimated with using the MLE as the value of λ, which maximises the probability of detecting k Bluetooth devices. The estimated values are backed up by indoor and outdoor experiments. Finally, a testbed was designed to provide information citywide. To this end,

an Android app has been designed, which collects Bluetooth scanning and location data. The collected data are uploaded to the cloud for processing, and the results are represented on a web page.

Chapter 4 investigated the WiFi-based crowd detection and its distribution estimation. In a real-world scenario, six WiFi probes were installed on a train platform to collect data. The collected data were used to determine the crowd density and its distribution. To determine the WiFi fingerprint map over the platform, three participants using six mobile phones were present on the platform and followed a predefined pattern. However, the collected data were sparse, which makes the location estimations very challenging. To overcome this issue, prior knowledge was applied on top of the fingerprint map to produce a probability map. The probability map is used to estimate the location of each node, and the expected value for the number of people in each cell is calculated. Then, using k-nearest neighbours, density heat maps are generated. Finally, the generated heat maps are compared to the results of CCTV images.

Both Bluetooth and WiFi probing methods show good accuracy. However, there are inherent privacy issues with these methods due to their unique fingerprint and MAC addresses. In chapter 5, a fully non-intrusive method to estimate crowds using available RF energy measurements is introduced. Any object in the environment directly affects the amount of measured electromagnetic energy. The human body consists 60% water on average and has a significant effect on the amount of available EM energy. These effects can be measured and modelled to understand the number of people and their behaviour. Numerical simulations using Comsol were performed to illustrate the effects of the human body in a room. The three-dimensional distribution of the E-field is extracted in two body resonance frequencies: 60 MHz and 2 GHz. The energy measurements are quite challenging at higher frequencies using antennas due to many holes and peaks. Multiple measurements at various points can be used to overcome this issue. Finally, a series of experiments was designed to test the

theory in reality. To have a controlled environment, the measurements were performed in a lift cabin. During the experiments, 20 different measurement positions for the antennas have been selected and average of all measurements calculated to obtain the amount of absorbed energy. It is proven that a 0.8 dB decrease in the energy levels can be measured for an average body.

Metamaterial absorbers were introduced as an alternative solution for multiple antenna measurements in chapters 6 and 7. Use of metamaterial absorbers also offers accurate measurements of the average of available EM energy. Chapter 6 provides a solution to design compact metamaterial absorbers using space-filling curves. Sierpinski curves are introduced as an example of space-filling curves to reach lower resonance frequencies at 900 MHz with the fixed size of the unit cell. In chapter 7, a multilayer absorber is introduced to accurately measure the EM energy levels. To minimise the loss, a substrate of Rogers 3003 with loss of 0.001 is chosen. The proposed structure introduces single vias to transfer the induced surface current to the bottom layer. The vias are connected to the ground plane through a resistor. Using this technique, measurements can be done without affecting the interference with the resonator structure. Both proposed structures were fabricated and tested. The final multi-layer structure was examined to determine the changes in the receiving RF power by monitoring voltage and currents on the components.

8.2 Future works

8.2.1 Increasing the accuracy of Bluetooth-based estimation

As shown, participatory Bluetooth scanning can be used to determine the number of people around each scanning node. Moving people around each node can be modelled with a dynamic probability model, which can be applied to increase the accuracy of the measurements and estimations. Furthermore, the estimated crowd density can be monitored to extract the

hourly, daily, and weekly patterns of the crowd changes in an area.

8.2.2 Increasing the accuracy of WiFi-based estimation

WiFi probes can be used to estimate the crowd density and its distribution. WiFi probes can be manipulated to decrease the scanning intervals. Then, methods such as Kalman or particle filters can be used to increase the accuracy of estimating the paths and associated locations of the detected nodes. Furthermore, WiFi probes can be integrated with CCTV images to cover blind spots of the images, while the images can provide a dynamic penetration rate to increase the accuracy of the measurements in the integrated system.

8.2.3 Crowd estimation based on EM energy level measurements

The proposed method of using electromagnetic measurements for crowd estimation purposes is introduced and tested in a controlled environment. The absorption effects of the human body should be tested in various indoor settings. Machine learning algorithms can be trained to monitor the small changes in the environment to increase the accuracy of the estimations in large and dynamic environments.

Metamaterials are introduced as a solution to replace multiple antennas and increase the accuracy of energy level measurements. New techniques in the design of metamaterial absorbers can be investigated to increase the sensitivity of absorbers in different bands and minimise the loss in the system. Thus, the accuracy of the measurements can be increased.

Bibliography

[1] Australia's population projected to double by 2075. *Austrlian Bureau of Statistics*, 2013.

[2] Travel forecast 2006-2036. *Austrlian Bureau of Transport Statistics*, 2012.

[3] Julio Cezar Silveira Jacques Junior, Soraia Raupp Musse, and Claudio Rosito Jung. Crowd analysis using computer vision techniques. *IEEE Signal Processing Magazine*, 27(5):66–77, 2010.

[4] Naeim Abedi, Ashish Bhaskar, and Edward Chung. Bluetooth and wi-fi mac address based crowd data collection and monitoring: benefits, challenges and enhancement. 2013.

[5] Jens Weppner, Benjamin Bischke, and Paul Lukowicz. Monitoring crowd condition in public spaces by tracking mobile consumer devices with wifi interface, 2016.

[6] Yaoxuan Yuan, Jizhong Zhao, Chen Qiu, and Wei Xi. Estimating crowd density in an rf-based dynamic environment. *IEEE Sensors Journal*, 13(10):3837–3845, 2013.

[7] Saandeep Depatla and Yasamin Mostofi. Crowd counting through walls using wifi. pages 1–10. IEEE, 2018.

[8] Wei Xi, Jizhong Zhao, Xiang-Yang Li, Kun Zhao, Shaojie Tang, Xue Liu, and Zhiping Jiang. Electronic frog eye: Counting crowd using wifi. pages 361–369. IEEE, 2014.

[9] Giuseppe Bonaccorso. *Machine Learning Algorithms*. Packt Publishing Ltd, 2017.

[10] A. Stopczynski, J. E. Larsen, S. Lehmann, L. Dynowski, and M. Fuentes. Participatory bluetooth sensing: A method for acquiring spatio-temporal data about participant mobility and interactions at large scale events. *Pervasive Computing and Communications Workshops (PERCOM Workshops), 2013 IEEE International Conference on*, pages 242–247, 2013.

[11] J. Weppner, P. Lukowicz, U. Blanke, and G. Troster. Participatory bluetooth scans serving as urban crowd probes. *IEEE Sensors Journal*, 14(12):4196–4206, 2014.

[12] Lorenz Schauer, Martin Werner, and Philipp Marcus. Estimating crowd densities and pedestrian flows using wi-fi and bluetooth. pages 171–177. ICST (Institute for Computer Sciences, Social-Informatics and Telecommunications Engineering), 2014.

[13] Cristian Chilipirea, Andreea-Cristina Petre, Ciprian Dobre, and Maarten van Steen. Presumably simple: monitoring crowds using wifi. volume 1, pages 220–225. IEEE, 2016.

[14] H. Jacobs. To count a crowd. *Columbia Journalism Review*, 6:36–40, 1967.

[15] Jason M. Grant and Patrick J. Flynn. Crowd scene understanding from video: A survey. *ACM Trans. Multimedia Comput. Commun. Appl.*, 13(2):19:1–19:23, March 2017.

[16] W. Xi, J. Zhao, X. Y. Li, K. Zhao, S. Tang, X. Liu, and Z. Jiang. Electronic frog eye: Counting crowd using wifi. In *IEEE INFOCOM 2014 - IEEE Conference on Computer Communications*, pages 361–369, April 2014.

[17] M. Yamin and Y. Ades. Crowd management with rfid and wireless technologies. *Networks and Communications, 2009. NETCOM '09. First International Conference on*, pages 439–442, 2009.

[18] J. Weppner and P. Lukowicz. Bluetooth based collaborative crowd density estimation with mobile phones. *Pervasive Computing and Communications (PerCom), 2013 IEEE International Conference on*, pages 193–200, 2013.

[19] G. Pan, G. Qi, W. Zhang, S. Li, Z. Wu, and L. T. Yang. Trace analysis and mining for smart cities: issues, methods, and applications. *IEEE Communications Magazine*, 51(6):120–126, June 2013.

[20] M. Wirz, T. Franke, D. Roggen, E. Mitleton-Kelly, P. Lukowicz, and G. Troster. Inferring crowd conditions from pedestrians' location traces for real-time crowd monitoring during city-scale mass gatherings. In *Enabling Technologies: Infrastructure for Collaborative Enterprises (WETICE), 2012 IEEE 21st International Workshop on*, pages 367–372, June 2012.

[21] J. C. Silveira Jacques Junior, S. R. Musse, and C. R. Jung. Crowd analysis using computer vision techniques. *IEEE Signal Processing Magazine*, 27(5):66–77, Sept 2010.

[22] Piotr Dollar, Christian Wojek, Bernt Schiele, and Pietro Perona. Pedestrian detection: An evaluation of the state of the art. *IEEE transactions on pattern analysis and machine intelligence*, 34(4):743–761, 2012.

[23] Min Li, Zhaoxiang Zhang, Kaiqi Huang, and Tieniu Tan. Estimating the number of people in crowded scenes by mid based foreground segmentation and head-shoulder detection. pages 1–4. IEEE, 2008.

[24] Xinyu Wu, Guoyuan Liang, Ka Keung Lee, and Yangsheng Xu. Crowd density estimation using texture analysis and learning. In *Robotics and Biomimetics, 2006. ROBIO'06. IEEE International Conference on*, pages 214–219. IEEE, 2006.

[25] Juergen Gall, Angela Yao, Nima Razavi, Luc Van Gool, and Victor Lempitsky. Hough forests for object detection, tracking, and action recognition. *IEEE transactions on pattern analysis and machine intelligence*, 33(11):2188–2202, 2011.

[26] Navneet Dalal and Bill Triggs. Histograms of oriented gradients for human detection. volume 1, pages 886–893. IEEE, 2005.

[27] Payam Sabzmeydani and Greg Mori. Detecting pedestrians by learning shapelet features. pages 1–8. IEEE, 2007.

[28] Paul Viola and Michael J Jones. Robust real-time face detection. *International journal of computer vision*, 57(2):137–154, 2004.

[29] Bo Wu and Ram Nevatia. Detection of multiple, partially occluded humans in a single image by bayesian combination of edgelet part detectors. pages 90–97. IEEE, 2005.

[30] Antoni B Chan and Nuno Vasconcelos. Bayesian poisson regression for crowd counting. pages 545–551. IEEE, 2009.

[31] Ke Chen, Chen Change Loy, Shaogang Gong, and Tony Xiang. Feature mining for localised crowd counting. volume 1, page 3, 2012.

[32] David Ryan, Simon Denman, Clinton Fookes, and Sridha Sridharan. Crowd counting using multiple local features. pages 81–88. IEEE, 2009.

[33] Victor Lempitsky and Andrew Zisserman. Learning to count objects in images. pages 1324–1332, 2010.

[34] Yifei Yuan, Zhenrui Wang, Mingyang Li, Young-Jun Son, and Jian Liu. Dddas-based information-aggregation for crowd dynamics modeling with uavs and ugvs. *Frontiers in Robotics and AI*, 2:8, 2015.

[35] F. Calabrese, M. Colonna, P. Lovisolo, D. Parata, and C. Ratti. Real-time urban monitoring using cell phones: A case study in rome. *IEEE Transactions on Intelligent Transportation Systems*, 12(1):141–151, March 2011.

[36] R. A. Becker, R. Caceres, K. Hanson, J. M. Loh, S. Urbanek, A. Varshavsky, and C. Volinsky. A tale of one city: Using cellular network data for urban planning. *IEEE Pervasive Computing*, 10(4):18–26, April 2011.

[37] Nabeel Koshak and Abdullah Fouda. Analyzing pedestrian movement in mataf using gps and gis to support space redesign. In *The 9th international conference on design and decision support systems in architecture and urban planning*, 2008.

[38] Federico Botta, Helen Susannah Moat, and Tobias Preis. Quantifying crowd size with mobile phone and twitter data. *Open Science*, 2(5), 2015.

[39] R. O. Sinnott and W. Chen. Estimating crowd sizes through social media. In *2016 IEEE International Conference on Pervasive Computing and Communication Workshops (PerCom Workshops)*, pages 1–6, 2016.

[40] Mohammad Yamin, Masoud Mohammadian, Xu Huang, and Dharmendra Sharma. Rfid technology and crowded event management. pages 1293–1297. IEEE, 2008.

[41] A. Basalamah. Sensing the crowds using bluetooth low energy tags. *IEEE Access*, 4:4225–4233, 2016.

[42] Eamonn O'Neill, Vassilis Kostakos, Tim Kindberg, Ava Fatah gen. Schiek, Alan Penn, Danae Stanton Fraser, and Tim Jones. *Instrumenting the City: Developing Methods*

for Observing and Understanding the Digital Cityscape, pages 315–332. Springer Berlin Heidelberg, Berlin, Heidelberg, 2006.

[43] Darcy Bullock, Ross Haseman, Jason Wasson, and Robert Spitler. Automated measurement of wait times at airport security: deployment at indianapolis international airport, indiana. *Transportation Research Record: Journal of the Transportation Research Board*, (2177):60–68, 2010.

[44] C Mottram. Collective choreography of space: modelling digital co-presence in a public arena. International Institute for Advanced Studies/L'Institut International pour les Etudes Avancees, 2007.

[45] Simon Hay and Robert Harle. Bluetooth tracking without discoverability. pages 120–137. Springer, 2009.

[46] Mathias Versichele, Matthias Delafontaine, Tijs Neutens, and Nico Van de Weghe. Potential and implications of bluetooth proximity-based tracking in moving object research. 2010.

[47] TNAT ALREADY CONTAIN. Real-time travel time estimates using media access control address matching. *ITE JOURNAL*, 2008.

[48] Alexandra Millonig and Georg Gartner. Shadowing-tracking-interviewing: How to explore human spatio-temporal behaviour patterns. pages 1–14. Citeseer, 2008.

[49] Ali Haghani, Masoud Hamedi, Kaveh Sadabadi, Stanley Young, and Philip Tarnoff. Data collection of freeway travel time ground truth with bluetooth sensors. *Transportation Research Record: Journal of the Transportation Research Board*, (2160):60–68, 2010.

[50] Mathias Versichele, Tijs Neutens, Matthias Delafontaine, and Nico Van de Weghe. The use of bluetooth for analysing spatiotemporal dynamics of human movement at mass events: A case study of the ghent festivities. *Applied Geography*, 32(2):208–220, 2012.

[51] Matthias Delafontaine, Mathias Versichele, Tijs Neutens, and Nico Van de Weghe. Analysing spatiotemporal sequences in bluetooth tracking data. *Applied Geography*, 34:659–668, 2012.

[52] Naeim Abedi, Ashish Bhaskar, and Edward Chung. Tracking spatio-temporal movement of human in terms of space utilization using media-access-control address data. *Applied Geography*, 51:72–81, 2014.

[53] Marcus Handte, Muhammad Umer Iqbal, Stephan Wagner, Wolfgang Apolinarski, Pedro José Marrón, Eva Maria Muñoz Navarro, Santiago Martinez, Sara Izquierdo Barthelemy, and Mario González Fernández. Crowd density estimation for public transport vehicles. pages 315–322, 2014.

[54] Pravein Govindan Kannan, Seshadri Padmanabha Venkatagiri, Mun Choon Chan, Akhihebbal L Ananda, and Li-Shiuan Peh. Low cost crowd counting using audio tones. In *Proceedings of the 10th ACM Conference on Embedded Network Sensor Systems*, pages 155–168. ACM, 2012.

[55] Carlos Pérez-Penichet and Adriano Moreira. Analyzing the quality of crowd sensed wifi data. pages 272–277. IEEE, 2014.

[56] Yan Wang, Jie Yang, Hongbo Liu, Yingying Chen, Marco Gruteser, and Richard P Martin. Measuring human queues using wifi signals. pages 235–238. ACM, 2013.

[57] Saandeep Depatla, Arjun Muralidharan, and Yasamin Mostofi. Occupancy estimation using only wifi power measurements. *IEEE Journal on Selected Areas in Communications*, 33(7):1381–1393, 2015.

[58] Yan Wang, Jian Liu, Yingying Chen, Marco Gruteser, Jie Yang, and Hongbo Liu. E-eyes: device-free location-oriented activity identification using fine-grained wifi signatures. pages 617–628. ACM, 2014.

[59] Yanni Yang, Jiannong Cao, Xuefeng Liu, and Xiulong Liu. *Wi-Count Passing People Counting with COTS WiFi Devices*. 08 2018.

[60] Han Zou, Yuxun Zhou, Jianfei Yang, and Costas J. Spanos. Device-free occupancy detection and crowd counting in smart buildings with wifi-enabled iot. *Energy and Buildings*, 174:309–322, 2018.

[61] Simone Di Domenico, Mauro De Sanctis, Ernestina Cianca, and Giuseppe Bianchi. A trained-once crowd counting method using differential wifi channel state information. In *Proceedings of the 3rd International on Workshop on Physical Analytics*, WPA '16, pages 37–42, New York, NY, USA, 2016. ACM.

[62] J. C. Silveira Jacques Junior, S. R. Musse, and C. R. Jung. Crowd analysis using computer vision techniques. *IEEE Signal Processing Magazine*, 27(5):66–77, 2010.

[63] Mathias Versichele, Tijs Neutens, Matthias Delafontaine, and Nico Van de Weghe. The use of bluetooth for analysing spatiotemporal dynamics of human movement at mass events: A case study of the ghent festivities. *Applied Geography*, 32(2):208 – 220, 2012.

[64] G. V. Zaruba and V. Gupta. Simplified bluetooth device discovery - analysis and simulation. *System Sciences, 2004. Proceedings of the 37th Annual Hawaii International Conference on*, pages 9 pp.–, 2004.

[65] Marie Duflot, Marta Kwiatkowska, Gethin Norman, and David Parker. A formal analysis of bluetooth device discovery. *International journal on software tools for technology transfer*, 8(6):621–632, 2006.

[66] Tom Nicolai and Holger Kenn. About the relationship between people and discoverable bluetooth devices in urban environments. In *Proceedings of the 4th International Conference on Mobile Technology, Applications, and Systems and the 1st International Symposium on Computer Human Interaction in Mobile Technology*, Mobility '07, pages 72–78, New York, NY, USA, 2007. ACM.

[67] Andrea Goldsmith. *Wireless communications*. Cambridge university press, 2005.

[68] Donna J Peuquet. A conceptual framework and comparison of spatial data models. *Classics in Cartography: Reflections on Influential Articles from Cartographica*, pages 147–195, 2011.

[69] Manuela Vasilescu and Demetri Terzopoulos. Adaptive meshes and shells: Irregular triangulation, discontinuities, and hierarchical subdivision. In *Computer Vision and Pattern Recognition, 1992. Proceedings CVPR'92., 1992 IEEE Computer Society Conference on*, pages 829–832. IEEE, 1992.

[70] Geoffrey Dutton. Part 4: Mathematical, algorithmic and data structure issues: Geodesic modelling of planetary relief. *Cartographica: The International Journal for Geographic Information and Geovisualization*, 21(2-3):188–207, 1984.

[71] Weizhe Liu, Krzysztof Lis, Mathieu Salzmann, and Pascal Fua. Geometric and physical constraints for head plane crowd density estimation in videos. *arXiv preprint arXiv:1803.08805*, 2018.

[72] Jason M Grant and Patrick J Flynn. Crowd scene understanding from video: a survey. *ACM Transactions on Multimedia Computing, Communications, and Applications (TOMM)*, 13(2):19, 2017.

[73] Yungeun Kim, Hyojeong Shin, and Hojung Cha. Smartphone-based wi-fi pedestrian-tracking system tolerating the rss variance problem. pages 11–19. IEEE, 2012.

[74] Di Wu, Qiang Liu, Yuan Zhang, Julie McCann, Amelia Regan, and Nalini Venkatasubramanian. Crowdwifi: efficient crowdsensing of roadside wifi networks. pages 229–240. ACM, 2014.

[75] Xiaoyong Tang, Bin Xiao, and Kenli Li. Indoor crowd density estimation through mobile smartphone wi-fi probes. *IEEE Transactions on Systems, Man, and Cybernetics: Systems*, 2018.

[76] Xiaonan Guo, Bo Liu, Cong Shi, Hongbo Liu, Yingying Chen, and Mooi Choo Chuah. Wifi-enabled smart human dynamics monitoring. page 16. ACM, 2017.

[77] Rui Zhou, Meng Hao, Xiang Lu, Mingjie Tang, and Yang Fu. Device-free localization based on csi fingerprints and deep neural networks. pages 1–9. IEEE, 2018.

[78] Piotr Sapiezynski, Arkadiusz Stopczynski, Radu Gatej, and Sune Lehmann. Tracking human mobility using wifi signals. *PloS one*, 10(7):e0130824, 2015.

[79] Ahmed Shokry, Moustafa Elhamshary, and Moustafa Youssef. The tale of two localization technologies: Enabling accurate low-overhead wifi-based localization for low-end phones. page 42. ACM, 2017.

[80] Yang Gu, Caifa Zhou, Andreas Wieser, and Zhimin Zhou. Pedestrian positioning using wifi fingerprints and a foot-mounted inertial sensor. pages 91–99. IEEE, 2017.

[81] Eladio Martin, Oriol Vinyals, Gerald Friedland, and Ruzena Bajcsy. Precise indoor localization using smart phones. pages 787–790. ACM, 2010.

[82] Ville Honkavirta, Tommi Perala, Simo Ali-Loytty, and Robert Piché. A comparative survey of wlan location fingerprinting methods. pages 243–251. IEEE, 2009.

[83] Zahid Farid, Rosdiadee Nordin, and Mahamod Ismail. Recent advances in wireless indoor localization techniques and system. *Journal of Computer Networks and Communications*, 2013, 2013.

[84] Esmond Mok and Günther Retscher. Location determination using wifi fingerprinting versus wifi trilateration. *Journal of Location Based Services*, 1(2):145–159, 2007.

[85] Vishal Singh, Gorish Aggarwal, and BVS Ujwal. Ensemble based real-time indoor localization using stray wifi signal. pages 1–5. IEEE, 2018.

[86] Steven B. Heymsfield, ZiMian Wang, Richard N Baumgartner, and Robert Ross. Human body composition: advances in models and methods. *Annual review of nutrition*, 17(1):527–558, 1997.

[87] Gregory CR Melia, Martin P Robinson, Ian D Flintoft, Andrew C Marvin, and John F Dawson. Broadband measurement of absorption cross section of the human body in a reverberation chamber. *IEEE Transactions on Electromagnetic Compatibility*, 55(6):1043–1050, 2013.

[88] Yuri Feldman, Alexander Puzenko, and Yaroslav Ryabov. Dielectic relaxation phenomena in complex materials. *Advances in chemical physics*, 133(A):1, 2006.

[89] David Keun Cheng et al. *Field and wave electromagnetics*. Pearson Education India, 1989.

[90] Sami Gabriel, RW Lau, and Camelia Gabriel. The dielectric properties of biological tissues: Iii. parametric models for the dielectric spectrum of tissues. *Physics in Medicine & Biology*, 41(11):2271, 1996.

[91] Om P Gandhi. Millimeter-resolution mri-based models of the human body for electromagnetic dosimetry from elf to microwave frequencies. In *Proc. Int. Workshop on Voxel Phantom Development, 1995*, pages 24–31, 1995.

[92] XG Xu, TC Chao, and A Bozkurt. Vip-man: an image-based whole-body adult male model constructed from color photographs of the visible human project for multi-particle monte carlo calculations. *Health Physics*, 78(5):476–486, 2000.

[93] P Ferrari and G Gualdrini. An improved mcnp version of the norman voxel phantom for dosimetry studies. *Physics in Medicine & Biology*, 50(18):4299, 2005.

[94] Peter Dimbylow. Development of the female voxel phantom, naomi, and its application to calculations of induced current densities and electric fields from applied low frequency magnetic and electric fields. *Physics in Medicine & Biology*, 50(6):1047, 2005.

[95] Peter J Dimbylow, Tomoaki Nagaoka, and X George Xu. A comparison of foetal sar in three sets of pregnant female models. *Physics in medicine & biology*, 54(9):2755, 2009.

[96] Andreas Christ, Wolfgang Kainz, Eckhart G Hahn, Katharina Honegger, Marcel Zefferer, Esra Neufeld, Wolfgang Rascher, Rolf Janka, Werner Bautz, Ji Chen, et al. The virtual familydevelopment of surface-based anatomical models of two adults and two children for dosimetric simulations. *Physics in Medicine & Biology*, 55(2):N23, 2009.

[97] Akimasa Hirata, Ilkka Laakso, Takuya Oizumi, Ryuto Hanatani, Kwok Hung Chan, and Joe Wiart. The relationship between specific absorption rate and temperature elevation in anatomically based human body models for plane wave exposure from 30 mhz to 6 ghz. *Physics in Medicine & Biology*, 58(4):903, 2013.

[98] R. Liu, C. Ji, J. J. Mock, J. Y. Chin, T. J. Cui, and D. R. Smith. Broadband ground-plane cloak. *Science*, 323(5912):366–369, 2009.

[99] Nathan Kundtz, Daniel Gaultney, and David R. Smith. Scattering cross-section of a transformation optics-based metamaterial cloak. *New Journal of Physics*, 12(4):043039, 2010.

[100] John B. Pendry, David Schurig, and David R. Smith. Controlling electromagnetic fields. *science*, 312(5781):1780–1782, 2006.

[101] Hui Feng Ma and Tie Jun Cui. Three-dimensional broadband ground-plane cloak made of metamaterials. *Nature communications*, 1:21, 2010.

[102] Guy Lipworth, Joshua Ensworth, Kushal Seetharam, Da Huang, Jae Seung Lee, Paul Schmalenberg, Tsuyoshi Nomura, Matthew S. Reynolds, David R. Smith, and Yaroslav Urzhumov. Magnetic metamaterial superlens for increased range wireless power transfer. *Scientific reports*, 4:3642, 2014.

[103] Nicholas Fang, Hyesog Lee, Cheng Sun, and Xiang Zhang. Sub-diffraction-limited optical imaging with a silver superlens. *Science*, 308(5721):534–537, 2005.

[104] Yongzhi Cheng, Xue Song Mao, Chenjun Wu, Lin Wu, and RongZhou Gong. Infrared non-planar plasmonic perfect absorber for enhanced sensitive refractive index sensing. *Optical Materials*, 53:195–200, 2016.

[105] Longqing Cong, Siyu Tan, Riad Yahiaoui, Fengping Yan, Weili Zhang, and Ranjan Singh. Experimental demonstration of ultrasensitive sensing with terahertz metamaterial absorbers: A comparison with the metasurfaces. *Applied Physics Letters*, 106(3):031107, 2015.

[106] Khagendra Bhattarai, Zahyun Ku, Sinhara Silva, Jiyeon Jeon, Jun Oh Kim, Sang Jun Lee, Augustine Urbas, and Jiangfeng Zhou. A largearea, mushroomcapped plasmonic perfect absorber: Refractive index sensing and fabry-perot cavity mechanism. *Advanced Optical Materials*, 3(12):1779–1786, 2015.

[107] Yang Hao and Raj Mittra. *FDTD modeling of metamaterials: Theory and applications*. Artech house, 2008.

[108] Tie Jun Cui, David R. Smith, and R. P. Liu. *Metamaterials*. Springer, 2010.

[109] R. A. Shelby, D. R. Smith, S. C. Nemat-Nasser, and Sheldon Schultz. Microwave transmission through a two-dimensional, isotropic, left-handed metamaterial. *Applied Physics Letters*, 78(4):489–491, 2001.

[110] David Schurig, J. J. Mock, B. J. Justice, Steven A. Cummer, John B. Pendry, A. F. Starr, and D. R. Smith. Metamaterial electromagnetic cloak at microwave frequencies. *Science*, 314(5801):977–980, 2006.

[111] T. Koschny, M. Kafesaki, E. N. Economou, and C. M. Soukoulis. Effective medium theory of left-handed materials. *Physical Review Letters*, 93(10):107402–, 09 2004.

[112] Zhangqi Liao, Rongzhou Gong, Yan Nie, Tao Wang, and Xian Wang. Absorption enhancement of fractal frequency selective surface absorbers by using microwave absorbing material based substrates. *Photonics and Nanostructures-Fundamentals and Applications*, 9(3):287–294, 2011.

[113] Jiaming Hao, Lei Zhou, and Min Qiu. Nearly total absorption of light and heat generation by plasmonic metamaterials. *Physical review B*, 83(16):165107, 2011.

[114] Marcus Diem, Thomas Koschny, and Costas M. Soukoulis. Wide-angle perfect absorber/thermal emitter in the terahertz regime. *Physical Review B*, 79(3):033101, 2009.

[115] Hou-Tong Chen, Willie J. Padilla, Joshua M. O. Zide, Seth R. Bank, Arthur C. Gossard, Antoinette J. Taylor, and Richard D. Averitt. Ultrafast optical switching of

terahertz metamaterials fabricated on eras/gaas nanoisland superlattices. *Optics letters*, 32(12):1620–1622, 2007.

[116] Mehdi Hajizadegan, Vahid Ahmadi, and Maryam Sakhdari. Design and analysis of ultrafast and tunable all optical metamaterial switch enhanced by metal nanocomposite. *Journal of Lightwave Technology*, 31(12):1877–1883, 2013.

[117] Viktor G Veselago. The electrodynamics of substances with simultaneously negative values of and μ. *Soviet physics uspekhi*, 10(4):509, 1968.

[118] David R. Smith, D. C. Vier, N. Kroll, and S. Schultz. Direct calculation of permeability and permittivity for a left-handed metamaterial. *Applied Physics Letters*, 77(14):2246–2248, 2000.

[119] H. Nornikman, Badrul Ahmad, Mohamad Zoinol Abd Aziz, Zahriladha Zakaria, Mohd Azlishah Othman, A. R. Othman, Mariana Yusoff, and Kamaruzaman Jusoff. *Rice Husk Truncated Pyramidal Microwave Absorber using Quadruple P-Spiral Split Ring Resonator (QPS-SRR)*, volume 7. February 2013.

[120] N. I. Landy, S. Sajuyigbe, J. J. Mock, D. R. Smith, and W. J. Padilla. Perfect metamaterial absorber. *Physical review letters*, 100(20):207402, 2008.

[121] Bui Xuan Khuyen, Bui Son Tung, Young Joon Yoo, Young Ju Kim, Ki Won Kim, Liang-Yao Chen, Vu Dinh Lam, and YoungPak Lee. Miniaturization for ultrathin metamaterial perfect absorber in the vhf band. *Scientific Reports*, 7:45151, 2017.

[122] Wei Shi, Shaobin Liu, Busheng Zheng, Xiangkun Kong, Haifeng Zhang, and Siyuan Liu. Broadband perfect metamaterial absorption, based on flexible material. pages 1–3. IEEE, 2016.

[123] A. Ishikawa. Infrared metamaterials for high-sensitive surface-enhanced molecular detection. In *2016 URSI Asia-Pacific Radio Science Conference (URSI AP-RASC)*, pages 1–3, 2016.

[124] Li-Fang Yao, Min-Hua Li, Xiao-Min Zhai, Hui-Bo Wang, and Jian-Feng Dong. On the miniaturization of polarization insensitive wide angle metamaterial absorber. *Applied Physics A*, 122(2):61, 2016.

[125] Fan Yue-Nong, Cheng Yong-Zhi, Nie Yan, Wang Xian, and Gong Rong-Zhou. An ultrathin wide-band planar metamaterial absorber based on a fractal frequency selective surface and resistive film. *Chinese Physics B*, 22(6):067801, 2013.

[126] Yanbing Ma, Huaiwu Zhang, Yuanxun Li, and Yicheng Wang. Miniaturized and dual-band metamaterial absorber with fractal sierpinski structure. *JOSA B*, 31(2):325–331, 2014.

[127] Bui Xuan Khuyen, Bui Son Tung, Young Joon Yoo, Young Ju Kim, Ki Won Kim, Liang-Yao Chen, Vu Dinh Lam, and YoungPak Lee. Miniaturization for ultrathin metamaterial perfect absorber in the vhf band. *Scientific Reports*, 7:45151, 2017.

[128] Weiqing Zuo, Yang Yang, Xiaoxiang He, Dawei Zhan, and Qifan Zhang. A miniaturized metamaterial absorber for ultrahigh-frequency rfid system. *IEEE Antennas and Wireless Propagation Letters*, 16:329–332, 2017.

[129] Yong Zhi Cheng, Ying Wang, Yan Nie, Rong Zhou Gong, Xuan Xiong, and Xian Wang. Design, fabrication and measurement of a broadband polarization-insensitive metamaterial absorber based on lumped elements. *Journal of applied physics*, 111(4):044902, 2012.

[130] Mehmet Bakir, Muharrem Karaaslan, Furkan Dincer, Kemal Delihacioglu, and Cumali Sabah. Perfect metamaterial absorber-based energy harvesting and sensor applications in the industrial, scientific, and medical band. *Optical Engineering*, 54(9):097102, 2015.

[131] Hasan Kocer, Serkan Butun, Zhongyang Li, and Koray Aydin. Reduced near-infrared absorption using ultra-thin lossy metals in fabry-perot cavities. *Scientific reports*, 5:8157, 2015.

[132] Weiqing Zuo, Yang Yang, Xiaoxiang He, Dawei Zhan, and Qifan Zhang. A miniaturized metamaterial absorber for ultrahigh-frequency rfid system. *IEEE Antennas and Wireless Propagation Letters*, 16:329–332, 2017.

[133] O. T. Gunduz and C. Sabah. Polarization angle independent perfect multiband metamaterial absorber and energy harvesting application. *Journal of Computational Electronics*, 15(1):228–238, 2016.

[134] Jin Woo Park, Pham Van Tuong, Joo Yull Rhee, Ki Won Kim, Won Ho Jang, Eun Ha Choi, Liang Yao Chen, and YoungPak Lee. Multi-band metamaterial absorber based on the arrangement of donut-type resonators. *Optics express*, 21(8):9691–9702, 2013.

[135] Han Xiong, Jin-Song Hong, Chao-Ming Luo, and Lin-Lin Zhong. An ultrathin and broadband metamaterial absorber using multi-layer structures. *Journal of Applied Physics*, 114(6):064109, 2013.

[136] Govind Dayal and S. Anantha Ramakrishna. Design of multi-band metamaterial perfect absorbers with stacked metaldielectric disks. *Journal of Optics*, 15(5):055106, 2013.

[137] Changlei Zhang, Cheng Huang, Mingbo Pu, Jiakun Song, Zeyu Zhao, Xiaoyu Wu, and Xiangang Luo. Dual-band wide-angle metamaterial perfect absorber based on the

combination of localized surface plasmon resonance and helmholtz resonance. *Scientific Reports*, 7(1):5652, 2017.

[138] Toan Trung Nguyen and Sungjoon Lim. Wide incidence angle-insensitive metamaterial absorber for both te and tm polarization using eight-circular-sector. *Scientific reports*, 7(1):3204, 2017.

[139] Bo Zhu, Zhengbin Wang, Ci Huang, Yijun Feng, Junming Zhao, and Tian Jiang. Polarization insensitive metamaterial absorber with wide incident angle. *Progress In Electromagnetics Research*, 101:231–239, 2010.

[140] K. Y. Park, N. Wiwatcharagoses, A. Baczewski, and P. Chahal. A novel terahertz power meter using metamaterial-inspired thin-film absorber. In *2011 International Conference on Infrared, Millimeter, and Terahertz Waves*, pages 1–2, 2011.

[141] D. Hasan and C. Lee. Hybrid metamatarial absorber enhanced sensing of co2 gas in the 5–8 m mid ir spectral window. In *2017 19th International Conference on Solid-State Sensors, Actuators and Microsystems (TRANSDUCERS)*, pages 664–667, 2017.

[142] B. Ni, Z. Y. Wang, R. S. Zhao, X. Y. Ma, Z. Q. Xing, L. S. Yang, L. J. Huang, Y. Y. Lin, and D. B. Zhang. Humidity sensor based on perfect metamaterial absorber. In *2016 International Conference on Numerical Simulation of Optoelectronic Devices (NUSOD)*, pages 37–38, 2016.

[143] H. K. Kim, M. Yoo, and S. Lim. Novel ethanol chemical sensor using microfluidic metamaterial. In *2015 IEEE International Symposium on Antennas and Propagation & USNC/URSI National Radio Science Meeting*, pages 1358–1359, 2015.

[144] Francesca Venneri, Sandra Costanzo, and Giuseppe Di Massa. Fractal-shaped metamaterial absorbers for multireflections mitigation in the uhf band. *IEEE Antennas and Wireless Propagation Letters*, 17(2):255–258, 2018.

[145] Lu-Lu Liu, Hai-Feng Zhang, and Ling-Ling Wang. A novel broadband metamaterial absorber based on the fractal structure. pages 1928–1931. IEEE, 2016.

[146] Daecheon Lim, Dongju Lee, and Sungjoon Lim. Angle-and polarization-insensitive metamaterial absorber using via array. *Scientific reports*, 6:39686, 2016.

[147] Francesca Venneri, Sandra Costanzo, and Giuseppe Di Massa. Fractal-shaped metamaterial absorbers for multireflections mitigation in the uhf band. *IEEE Antennas and Wireless Propagation Letters*, 17(2):255–258, 2018.

[148] Lu-Lu Liu, Hai-Feng Zhang, and Ling-Ling Wang. A novel broadband metamaterial absorber based on the fractal structure. pages 1928–1931. IEEE, 2016.

[149] MRI Faruque, MM Hasan, and MT Islam. Tree-shaped fractal meta-surface with left-handed characteristics for absorption application. *Applied Physics A*, 124(2):127, 2018.

[150] ID Flintoft, MP Robinson, GCR Melia, AC Marvin, and JF Dawson. Average absorption cross-section of the human body measured at 1–12 ghz in a reverberant chamber: results of a human volunteer study. *Physics in Medicine & Biology*, 59(13):3297, 2014.

[151] Katsushige Harima. Estimation of power absorbed by human body using reverberation chamber. pages 39–43. IEEE, 2012.

[152] Bui Son Tung, Bui Xuan Khuyen, Young Ju Kim, Vu Dinh Lam, Ki Won Kim, and YoungPak Lee. Polarization-independent, wide-incident-angle and dual-band perfect absorption, based on near-field coupling in a symmetric metamaterial. *Scientific reports*, 7(1):11507, 2017.

[153] Toan Trung Nguyen and Sungjoon Lim. Wide incidence angle-insensitive metamaterial absorber for both te and tm polarization using eight-circular-sector. *Scientific reports*, 7(1):3204, 2017.

[154] Daecheon Lim, Dongju Lee, and Sungjoon Lim. Angle-and polarization-insensitive metamaterial absorber using via array. *Scientific reports*, 6:39686, 2016.

[155] Dongju Lee, Jung Gyu Hwang, Daecheon Lim, Tadayoshi Hara, and Sungjoon Lim. Incident angle-and polarization-insensitive metamaterial absorber using circular sectors. *Scientific reports*, 6:27155, 2016.

[156] Li Li Cong, Xiang Yu Cao, Tao Song, Jun Gao, and Jun Xiang Lan. Angular-and polarization-insensitive ultrathin double-layered metamaterial absorber for ultra-wideband application. *Scientific reports*, 8(1):9627, 2018.